NOVA SCHOOL OF SCIENCE & TECHNOLOGY

DEPARTMENT OF PHYSICS

JOANA CUNHA CAETANO

Bachelor of Science in Biomedical Engineering

DEVELOPMENT OF A LOW-COST, NON-ENZYMATIC GLUCOSE SENSOR BASED ON COPPER NANOPARTICLES AND LASER-INDUCED GRAPHENE TOWARDS WEARABLE SENSING

MASTER IN BIOMEDICAL ENGINEERING

NOVA University Lisbon
November, 2021

NOVA SCHOOL OF
SCIENCE & TECHNOLOGY

DEPARTMENT
OF PHYSICS

DEVELOPMENT OF A LOW-COST, NON-ENZYMATIC GLUCOSE SENSOR BASED ON COPPER NANOPARTICLES AND LASER-INDUCED GRAPHENE TOWARDS WEARABLE SENSING

JOANA CUNHA CAETANO

Bachelor of Science in Biomedical Engineering

Adviser: Prof. Elvira Fortunato
Full Professor, NOVA University Lisbon

MASTER IN BIOMEDICAL ENGINEERING

NOVA University Lisbon
November, 2021

Development of a low-cost, non-enzymatic glucose sensor based on copper nanoparticles and laser-induced graphene towards wearable sensing

Acknowledgements

Agradeço à minha orientadora, a Professora Elvira Fortunato, pela oportunidade de desenvolver este projeto no CENIMAT e ao Tomás, por todo o tempo despendido e apoio durantes estes meses.

Um especial obrigada ao André pela paciência, amizade, partilha de conhecimento, dicas de inglês e etc etc etc.

À Mariana e ao Francisco, companheiros de cenimatas, por todas as vezes que me distraíram e impediram de trabalhar.

Aos monkeys pelos fantásticos 5 anos de curso, todos os momentos que passámos juntos em festas, viagens e jantares e por todos os minutos dedicados a gozarem com a minha pessoa.

À Joana e ao Ricardo por todas as conversas parvas ou menos parvas que tivemos.

À minha família por me apoiar em todas as escolhas e pelo questionário semanal do estado da tese.

À Mara, Filipa, Telma, Henrique, Kika, Zagalo, Rita, às minhas afilhadas lindas e padrinhos jeitosos, a todos um grande obrigada.

"There's no such thing as a free lunch."

Abstract

According to the International Diabetes Federation (IDF), in 2021 approximately 537 million adults (20 to 79 years) suffered from diabetes, which corresponds to a total of 10.5 % of the world's adult population, and its prevalence is predicted to rise dramatically in the following years. Since glucose sensors constitute an effective approach for diabetes management, by providing precise information about glucose levels, the glucose sensor market has experienced enormous growth in the last few years. However, due to the high cost of the commercially available glucose detection solutions and since the rise in the number of diabetic patients has been more pronounced in low and middle-income countries, there is a high demand for low-cost glucose monitoring systems.

In order to address the lack of inexpensive glucose sensors issue, this thesis aims to meet the presented necessity in three strands: the development of a glucose sensor based on copper nanoparticles (CuNPs) and Laser-Induced Graphene (LIG), fabricated on paper substrate. Firstly, the LIG technique offers a rapid and simple method for the production of graphitized material, which is an extremely conductive composite and valuable for the sensing field, without the need for expensive and complex fabrication techniques. Moreover, it allows the LIG production on paper, which is a more sustainable, flexible, economic and easily accessible alternative than other commonly used substrates. For the non-enzymatic glucose detection, a cheap copper precursor was selected for the laser-induced CuNPs formation, presenting highly catalytic activity towards the glucose oxidation. Thus, CuNPs and LIG composites were simultaneously synthesized in one fabrication step, allowing for a large-scale sensor production.

LIG was fabricated with a sheet resistance value as low as 14.8 Ω sq^{-1}. The sensor showed good glucose sensing performance (267 μA mM^{-1} cm^{-2} sensitivity, 11 μM detection limit, and high selectivity and reproducibility) with a linear range within the glucose concentration range detected in sweat (20 μM - 1.79 mM), opening the possibility of integrating this method into a wearable and non-invasive glucose monitoring system.

Keywords: Glucose, paper biosensor, laser-induced graphene, copper nanoparticles, one-step synthesis, non-enzymatic, flexible electronics, sustainability.

Resumo

De acordo com a *International Diabetes Federation*, em 2021, cerca de 537 milhões de adultos (20 a 79 anos) viviam com diabetes, o que corresponde a um total de 10,5 % da população adulta a nível mundial, e prevê-se que a sua prevalência continue a aumentar. Uma vez que os sensores de glucose constituem uma abordagem eficaz para o controlo da diabetes, fornecendo informação precisa sobre os níveis de glucose, o seu mercado tem vindo a registar um enorme crescimento. Contudo, devido ao elevado custo das soluções propostas e, uma vez que o aumento do número de pacientes diabéticos é mais pronunciado nos países de baixo e médio rendimento, continua a haver uma grande procura por sistemas de baixo custo para a monitorização da glucose.

Com o objetivo de apresentar uma solução viável e barata para a deteção da glucose, esta tese visa satisfazer a necessidade apresentada em três vertentes, com o desenvolvimento de um sensor de glucose baseado em nanopartículas de cobre (Cu NPs) e grafeno induzido por laser (GIL), fabricado em substrato de papel. Em primeiro lugar, a técnica de GIL oferece uma forma rápida e simples para a produção de material grafítico, de elevada condutividade, sem a necessidade da aplicação de técnicas de fabricação dispendiosas e complexas. Além disso, permite a produção de GIL em papel, constituindo uma alternativa mais sustentável, flexível e económica do que outros substratos geralmente utilizados. A deteção não enzimática da glucose é feita através das Cu NPs, sintetizadas a partir de um precursor de cobre barato, que possuem propriedades catalíticas. Assim, as Cu NPs e o GIL são simultaneamente sintetizados numa única etapa de fabrico, permitindo uma produção destes sensores em grande escala. Na síntese do GIL obteve-se um valor de resistência da folha de 14,8 Ω sq^{-1}. O sensor demonstrou um bom desempenho na deteção da glucose (sensibilidade de 267 μA mM^{-1} cm^{-2}, limite de deteção de 11 μM e alta seletividade e reprodutibilidade) com alcance linear dentro da janela de concentrações de glucose detetadas no suor (20 μM - 1,79 mM), abrindo a possibilidade de integração deste método num sistema de monitorização de glucose "wearable"e não-invasivo.

Palavras-chave: Glucose, biosensor em papel, grafeno induzido por laser, nanopartículas de cobre, síntese numa etapa, não enzimático, eletrónica flexível, sustentabilidade.

Contents

List of Figures

List of Tables

List of Constants

D_O	diffusion coefficient for ferricyanide in KCl (0.1 M)	6.67×10^{-6} cm^2 s^{-1}
$\mathbf{D}_R$	diffusion coefficient for ferrocyanide in KCl (0.1 M)	7.26×10^{-6} cm^2 s^{-1}
F	Faraday constant	96485 C mol^{-1}
R	Universal Gas constant	8.314 J K^{-1} mol^{-1}

Abbreviations

$\mathbf{A}_e$	electrochemical active surface area
ATP	Adenosine Triphosphate
CE	Counter Electrode
CuNPs	copper nanoparticles
CV	Cyclic Voltammetry
EDS	Energy Dispersive X-Ray Spectroscopy
EIS	Electrochemical Impedance Spectroscopy
EsB	Energy selective Backscattered
$\mathbf{glu}^-$	negatively charged glucose
GOx	glucose oxidase
IDF	International Diabetes Federation
$\mathbf{k}^0$	heterogeneous electron transfer rate
LDW	Laser Direct Writing
LIG	Laser-Induced Graphene
$\mathbf{R}_{CT}$	electron transfer resistance
$\mathbf{R}_S$	solution resistance
RE	Reference Electrode
SE	Secondary Electron
SEM	Scanning Electronic Microscope

VA ratio volume to surface area ratio

WE Working Electrode
WHO World Health Organization
WS Wearable Sensors

XPS X-Ray Photoelectron Spectroscopy
XRD X-Ray Diffraction

1

Introduction

1.1 Motivation and Context

With the world's ageing population increasing and the growing percentage of patients who need to be monitored, it has been a challenge to maintain good healthcare services that assure quality medical management for the worldwide population. The applicability of Internet of Things is revolutionising healthcare and medicine in a way that, with the introduction of Wearable Sensors (WS), self and continuous monitoring has become a reality on an everyday basis. These mobile electronics worn on the human body provide specific clinical information at the molecular level, crucial for health monitoring and prevention [1].

According to the World Health Organization (WHO), diabetic worldwide prevalence is now 537 million people and, each year, 1.6 million deaths have diabetes as its first cause [2], placing diabetes as one of the leading worldwide causes of death. With that said, diagnosis and control methods for diabetes are now among the most critical health challenges to the medical and scientific community. People who develop this pathology have the constant need to control their glucose concentration levels to adjust their diet, exercise practice, and dose their medication to avoid related complications [3].

Therefore there's a rise in the necessity of creating comfortable and straightforward devices capable of detecting blood sugar levels, allied with a keen interest in the development of glucose WS. This scientific field has gained enormous potential in the last few years, and according to Nery et al. [4], in 2016, glucose sensors constitute 85 % of the biosensor market. Also, it is estimated a volume of 25 billion euros for the glucose sensor market by 2022 [5].

Although the glucose-sensing market is widely explored, most of the published research focus only on the development of non-invasive or non-enzymatic alternative glucose detection mechanisms, not taking into account their high production cost. Adding the non commercial viability, to the fact that more than 80 % of diabetic patients belong to low and middle-income countries [6], the need for economical glucose sensors arises.

Researchers have been interested in selecting paper as the substrate that supports

sensors in an attempt to develop inexpensive devices. In the past few years, paper has become an alternative platform for several applications because of its affordable price when compared to other materials, such as glass, plastic or silicone. Its use is promising in the area of flexible and sustainable electronics, suitable for sensing devices [7, 8].

1.2 Goals

This thesis aims to develop an inexpensive, sustainable and enzyme-free glucose sensor, with the possibility of being further integrated into a wearable system able to perform a non-invasive glucose detection from sweat. For this purpose, the sensor will be made of Laser-Induced Graphene (LIG), which is a highly conductive material, and copper nanoparticles (CuNPs) for the non-enzymatic detection of glucose, both synthesized on paper substrate. With that said, for the development of this dissertation, three main goals were defined:

1. LIG formation, followed by one-step synthesis of CuNPs-LIG composites by laser irradiation, on paper substrate;
2. Optimization of different LIG and CuNPs-LIG synthesis conditions such as the laser operational parameters and the copper precursor concentrations;
3. Fabrication of a CuNPs-LIG based sensor for glucose detection in the sweat concentration range.

2

Theoretical Concepts

This chapter presents the theoretical concepts required for a better understanding of this project. Combined with the theory that supports this thesis, it is vital to understand the need for glucose sensors in the diabetic population, especially low-cost sensors for developing countries. Moreover, it is crucial to clarify the importance of LIG and also metallic nanoparticles for the development of non-enzymatic glucose sensors.

2.1 Diabetes

Diabetes mellitus is one of the most common chronic conditions that affect millions of people worldwide, being one of the most prevalent and economically important diseases globally.

This disease develops two different possible variations: type 1 associated with deficient production of insulin by the pancreas and type 2 related to insulin resistance, which means that the organism is unable to use it effectively [9]. Diabetes pathogenesis is complex, yet its causes can be genetic, environmental, demographic, or can be related to behavioural risk factors, such as cigarette smoking, alcohol, and obesity. All of these factors provoke an impact on insulin that causes deregulation of blood glucose levels and harmful related micro and macrovascular consequences: cardiovascular damage, nerve degeneration, and vision damage are some of these related complications [10]. Also, it is expected that the patients affected by this condition suffer a significantly reduced life expectancy.

According to released data by the International Diabetes Federation (IDF), diabetes in 2017 was estimated to have caused four million worldwide deaths, and in the same year, a total of 617 billion euros was expended on global health for diabetes [11]. Besides, with the continuous population growth and the increased diabetes prevalence per year, it is foreseeable that these numbers will continue to rise (Figure 2.1). Thus, monitoring glucose concentration is a fundamental practice for effective diabetes management.

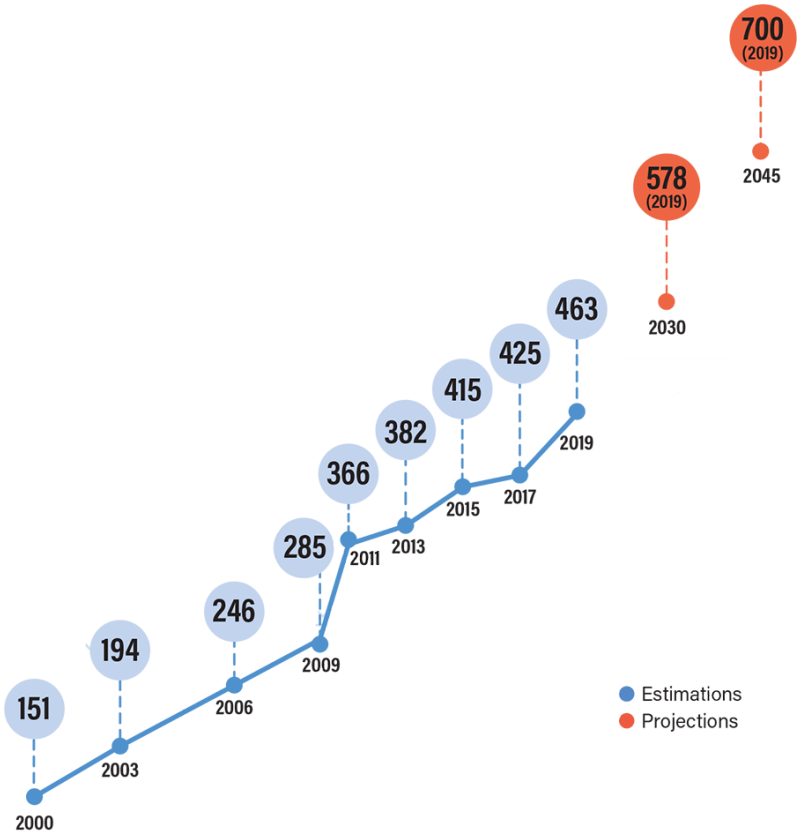

Figure 2.1: Evolution of the estimated number of adults (in millions) with diabetes all over the years (retrieved from the IDF [12]).

2.1.1 Glucose

Glucose is one of the most abundant and essential monosaccharides, with the molecular formula $C_6H_{12}O_6$. Glucose is also the primary energy source for living cells and participates in metabolic processes of the organisms to generate energy, such as cellular respiration and fermentation. These processes aim to obtain Adenosine Triphosphate (ATP), a highly energetic molecule, from metabolic reactions while a transformation chain of glucose molecules occurs. Glucose is stored in animals, fungi, and bacteria in the form of glycogen.

Blood glucose concentration is mainly regulated by insulin, which is produced by the pancreas. Its presence increases glucose permeability to cells, vital for the initiation of cellular metabolism. Abnormal sugar levels may indicate two different possible states, hypoglycemia and hyperglycemia. Hypoglycemia incidence is considered when blood glucose level drops below 3.9 mM [13], and it can lead to a state of anxiety, nausea, and fast heartbeat [14]. On the other hand, the rise of glucose levels beyond 7.8 mM can lead to hyperglycemia [15], which can increase the risk of heart and kidney diseases. As these values move further and further away from ideal blood glucose values, the symptoms associated with these two states become more severe. With that said, it is important to have a simple mechanism that maintains glucose levels at optimum values and prevents

a human being from reaching one of these two conditions.

2.2 Biosensors

Human's living quality underwent a huge change with the introduction of biosensors on a daily basis. Biosensors arise from the need of creating safe and cheaper solutions for a wide range of problems. Its research lead to the development of several applications in different sectors such as medical [16], environmental [17], food safety [18], and pharmaceutical [19] (Figure 2.2). These sensing platforms allow for the detection of a target analyte based on the affinity with a particular biochemical species [20]. Because these are user-friendly, rapid, cost-effective, highly sensitive and selective, the improvement in the biosensor field has been contributing to future medicine [21].

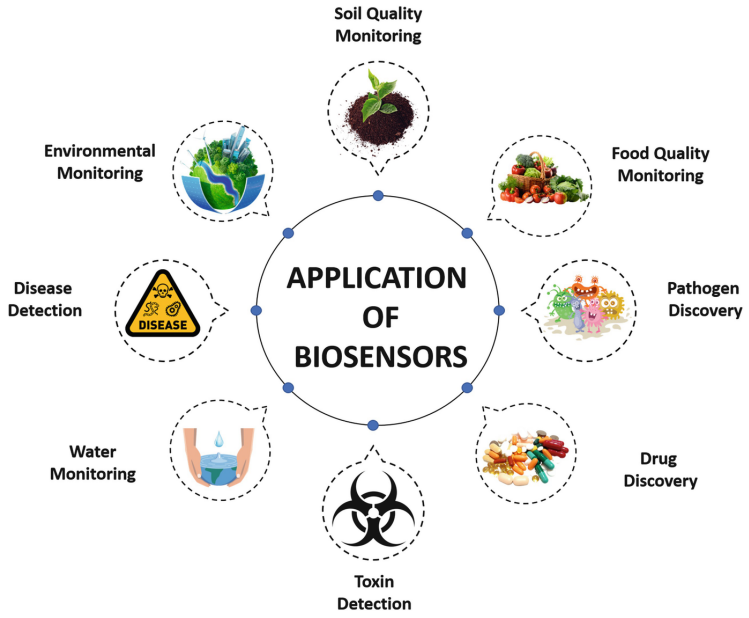

Figure 2.2: Examples of fields of work that use biosensor technology (retrieved from [22]).

There are certain properties specific to the sensor that can be reflected in its performance. The optimization of a sensor is based on the optimization of each of these parameters. The most important characteristics are [23, 24]:

- Linear Range - the analyte concentrations range in which the sensor responds as a linear function. The linear calibration curve can be calculated by plotting the measured signal as a function of the analyte concentrations.

- Selectivity - the sensor's capacity to detect a specific analyte in a sample containing interfering substances. It can be investigated by adding these contaminant species at their expected concentration into the measuring cell in the presence of the analyte that is actually intended to be measured.

- Sensitivity - the ratio between the magnitude of the sensor's output and the magnitude of the input quantity to be measured. By plotting the measured signal as a function of the real analyte concentrations, the sensitivity can be calculated as the slope of this calibration curve. The sensitivity is higher, as higher the slope.
- Limit of Detection - the minimum amount of analyte that can be reliably detected by the sensor, distinguishable from zero. This limit of detection depends on the sensor's sensitivity (S) and on the standard deviation of the response (σ).
- Response Time - the time interval that the sensor needs to achieve 95 % of the steady-state value after the addition of the analyte.
- Stability - the ability of the sensor to maintain a constant response over time; it is the most crucial feature in a continuous monitoring context. Stability can be investigated by measuring the output signal over a long time after adding a specific analyte concentration and calculating the mean deviation.
- Reproducibility - the sensor's ability to produce similar sensor's electrochemical responses for different sensors fabricated using the same procedure. It can be calculated by the mean deviation of several response measures towards the analyte from the mean value of them all. This parameter provides reliability to the sensor, showing that outputs do not result from one unique experiment and can be replicated with the same experimental conditions.

Biosensors can be categorised by their bioreceptor or transducer. The bioreceptor is a key biological agent that provides high selectivity, explicitly recognising the analyte to be measured, while the transducer is used to convert the biorecognition information event into a measurable analytical output [25] (Figure 2.3). The most used biorecognition elements are enzymes, organelles, cell receptors, proteins, antibodies, and microorganisms [16]. Various transduction methods can be separated into three different main classes: electrochemical, mass-based, and optical sensors [26].

To what concerns glucose biosensing, sensors usually are either optical or electrochemical in their core. In the following section, electrochemical sensors will be further explored, since the goal of this thesis relies on the development of such sensor.

2.2.1 Electrochemical Sensors

Electrochemical biosensors experienced tremendous progress over the last decade and are, at present, the most used and explored strategy for wearable glucose sensing. Several advantages, such as device miniaturisation, rapid response, high sensitivity and selectivity, make electrochemical sensing a promising method for glucose detection [27]. Therefore, electrochemical biosensors have become the leaders in the glucose sensor market currently. These sensors integrate electrodes capable of measuring electrical properties resulting from reduction and oxidation reactions.

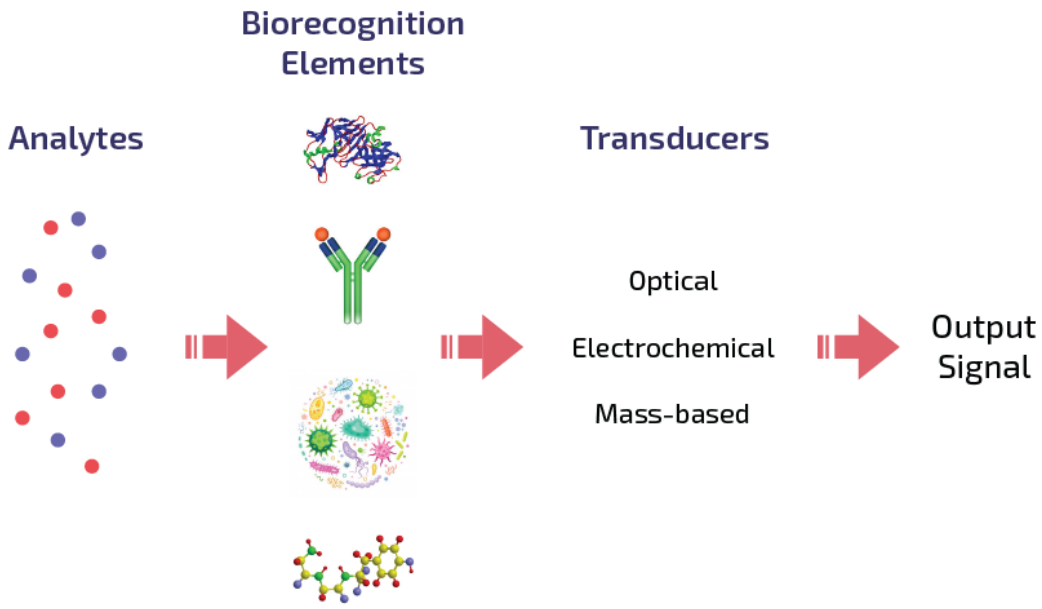

Figure 2.3: Schematic diagram of the components of a biosensor system.

2.2.1.1 Electrochemical cell

Electrochemical sensors' architecture is usually composed of three different electrodes that form the electrochemical cell (Figure 2.4):

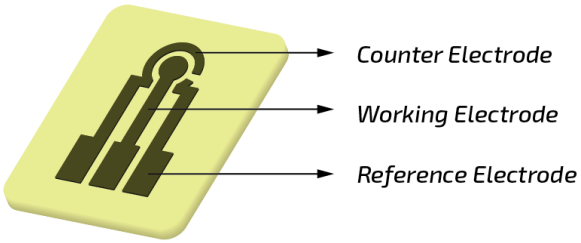

Figure 2.4: Schematic of a three-electrode electrochemical sensor.

- The Working Electrode (WE) is the most important component of the sensor because it is where the reaction, oxidation, or reduction of the target analyte is occurring. The measurement of the intended electrical property is highly influenced by the WE since this is the area where the sensing material is assembled [24]. The selection of the WE material is critical to attain realistic measurements since we want a material that assures good electron transfer properties between the chemical species involved in the reaction [28].

- The Reference Electrode (RE) has a constant and well-known electrochemical potential. This electrode allows for a fixed potential, meaning that a change in the cell refers to the WE [29]. The Ag/AgCl reference electrode is the most used in electrochemical sensing for aqueous solutions once it offers stable potentials that do not change over time or with temperature variations [24].

- The Counter Electrode (CE) is considered an auxiliary electrode and is used to complete the current circuit. This electrode is not involved in the chemical reaction; it only operates to flow the current between the WE and the CE [30]. To avoid limitations in the kinetics of the reaction, the surface area of this electrode must be much larger compared with the WE [31].

2.2.1.2 Detection method

Electrochemical sensors can be divided into different approaches to measuring analyte concentrations. Voltammetry, amperometry, potenciometry and impedance spectroscopy are the four main types of electrochemical methods of detection. This thesis aims to develop an amperometric sensor for glucose detection and will use voltammetry techniques to characterize and optimize the sensor performance.

The principle of voltammetry is based on the measurement of a current response as a function of the applied potential between the WE and RE [32]. The voltammogram, which is the resulting plot of current vs potential, provides quantitative and qualitative information about the species involved in the redox reaction [33]. This category groups several voltammetric methods that, using a potentiostat, apply specific voltage profiles to the WE. As the resulting current is measured, different types of voltammograms are generated as outputs. Cyclic Voltammetry (CV), Square Wave Voltammetry, Differential Pulse Voltammetry, Stripping Voltammetry, Polarography, Linear Sweep Voltammetry are some examples of these techniques [24].

An amperometric measure differs from the voltammetric one since the applied potential is fixed. It works by measuring the generated current from the targeted analyte catalysis in a chemical reaction, as a function of time. Through the application of a constant potential between the WE and the RE, the produced electrons migrate from the WE to the CE and electrical current can be measured. The resulting electrical current directly derives from the electron transfer rate, and it is proportional to the analyte concentration [1]. Next , a general insight of the working principles of CV is presented, since this technique will be extensively used in this work.

Fundamentals of cyclic voltammetry

CV is a powerful electrochemical technique used to investigate the reduction and oxidation processes of redox couples. Its basic operating principle is based on cycling the potential of the sensor's WE and measuring the current (between RE and CE) resulting

from electron transfers associated with the redox interactions. To complete one scan, the applied potential is varied linearly between two fixed switching potentials (E_1 and E_2), and when the E_2 potential is reached, the scan direction is reversed, as shown in Figure 2.5 A). This triangular excitation signal produces a cyclic voltammogram (Figure 2.5 B) when plotting current (vertical axis) versus potential (horizontal axis), which can provide important kinetic information such as electrochemical active surface area (A_e) and heterogeneous electron transfer rate (k^0) parameters.

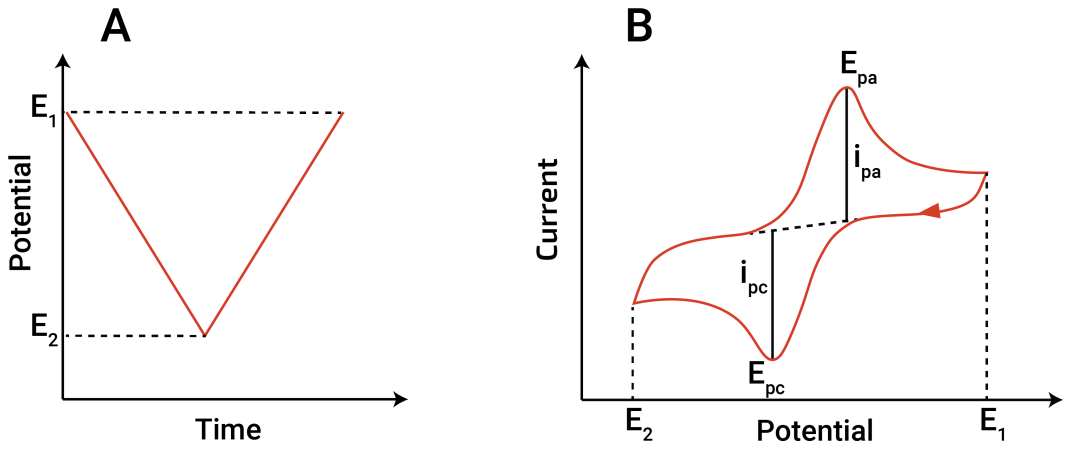

Figure 2.5: Cyclic voltammetry input and output. A) Applied potential waveform as a function of time for a generic cyclic voltammetry measurement. B) The resultant cyclic voltammogram showing anodic and cathodic current peaks.

Figure 2.5 B) shows a sample cyclic voltammogram obtained when performing CV trials on a sensor immersed in a solution containing the electroactive species and the supporting electrolyte. Considering $K_3[Fe(CN)_6]$ as the electroactive species, the following analysis of the voltammogram curve can be made. The potential starts at E_1 and is scanned negatively (cathodic current) in the direction indicated by the arrow. Then, when the potential attains a specific negative value, the electrode becomes a sufficiently strong reductant, and the following reaction starts to occur at the electrode surface:

$$Fe(CN)_6^{3-} + e \rightarrow Fe(CN)_6^{4-} \tag{2.1}$$

which provokes a current increase. At the same time, due to the gradient of chemical potential, the oxidized species starts to move from the bulk solution to the electrode surface, to be reduced. The cathodic peak appears when the $Fe(CN)_6^{3-}$ concentration is considerably low. After this, the current starts to decay until the switching potential (E_2) is reached. At this moment, the scan direction is reversed, and the potential is scanned in the positive direction (anodic current). Here, the opposite process arises, and the $Fe(CN)_6^{4-}$ species is oxidized back to $Fe(CN)_6^{3-}$ as the applied potential becomes more positive.

$$Fe(CN)_6^{4-} \rightarrow Fe(CN)_6^{3-} + e \tag{2.2}$$

Through the graph, the current increases until the anodic peak is reached, followed by a current decrease due to the depletion $Fe(CN)_6^{4-}$.

The reaction is considered electrochemically reversible when the electron transfer between the redox species and the WE is rapidly enough to maintain those species always in the Nernstian equilibrium. If this situation occurs, then the difference between the anodic and cathodic peak potentials, the peak separation *(ΔE_p)*, obeys the following equation [34]:

$$\Delta E_p = \frac{0.059}{n} \tag{2.3}$$

where n is the number of electrons participating in the charge transfer process.

Thus, considering one-electron processes, such as CV experiments that use $Fe(CN)_6{}^{3-/4-}$ couple as the supporting electrolyte, their reaction must exhibit a ΔE_p of 59 mV to be considered reversible. When the electron transfer of the redox species is slow, the peak separation in the voltammogram increases when the scan rate also increases. In this case, the system is described as quasi-reversible. In the last possible scenario, if the cathodic and anodic peaks in the CV curve are so far apart that there is no overlap between them on the potential axis, then the reaction is called irreversible [35, 36].

Next, some equations that allow the extraction of parameters to evaluate and compare the kinetic behavior of different reversible systems are presented. The calculated parameters are less accurate the farther the peak separation moves away from the perfect conditions, the reversible case.

The A_e can be estimated according to the Randles-Sevcik equation, which describes the peak current toward the scan rate [24]

$$i_p = 2.69 \times 10^5 n^{\frac{3}{2}} A D^{\frac{1}{2}} C v^{\frac{1}{2}} \tag{2.4}$$

where A_e is the electrochemical active surface area of the WE, D is the diffusion coefficient of the redox probe, n is the number of electrons participating in the charge transfer process, v is the scan rate, and C is the concentration of the redox probe molecule.

An electrode reaction is a heterogeneous redox reaction since it occurs only at the interface between the electrode surface and the electrolyte solution [29]. The k^0 is an important indicator for the application of the electrode in the electrochemical sensing context.

The method proposed by Nicholson relates the dimensionless kinetic parameter Ψ with the rate constant k^0 and is applicable to diffusion-controlled and quasi-reversible reactions [37]

$$\Psi = k_0 \left(\frac{D_O}{D_R} \right)^{\frac{\alpha}{2}} \sqrt{\frac{RT}{\pi n F D_O v}} \tag{2.5}$$

where D_O and D_R are the diffusion coefficients for oxidized and reduced species, R is the universal gas constant, T is the absolute temperature (295.15 K), and F is the Faraday

constant. For clarification, a diffusion-controlled system refers to reactions where the redox couple moves from the bulk solution to the electrode interface through diffusion processes, and the mass transport rate determines the reaction rate. α is the transfer coefficient and can be calculated from the slopes of the curves for anodic and cathodic peak currents vs. log of scan rate, respectively [38]:

$$\alpha = \frac{\delta_{pa}}{\delta_{pa} + \delta_{pc}} \tag{2.6}$$

The value of Ψ also depends on the peak separation through the following equation, developed by Klingler and Kochi [39]

$$\Psi = 2.18\left(\frac{\alpha}{\pi}\right)^{\frac{1}{2}} e^{\left[-\left(\alpha^2 F/RT\right)n\Delta E_p\right]} \tag{2.7}$$

This last equation is only valid for high values of the peak separations. For electrochemical systems characterized by $\Delta E_p < 220mV$, Lavagnini proposed an empirical relationship between the dimensionless parameter Ψ and the peak separation, expressed by Equation 2.8 [39]

$$\Psi = \frac{-0.6288 + 0.0021\Delta E_p}{1 - 0.017\Delta E_p} \tag{2.8}$$

In electrochemical measurements, when current is flowing through an electrochemical cell, a potential loss is always experienced between the RE and the WE. This phenomenon is called ohmic potential drop and is inherent to any voltammetric experiment [40].

Its effects can be reflected on the voltammogram by a decrease in the current magnitude and a shift in the cathodic and anodic peaks potential, consequently provoking an increase in the peak separation [36]. Moreover, with an increase in the scan rate, these undesirable consequences tend to be more intensified.

To mitigate these ohmic drop contributions, several factors can be manipulated [41]:

- The smaller the conductivity of the electrolyte, the higher the ohmic drop will be.
- The three-electrode system geometry will influence the shape and distribution of the equipotential lines (Figure 2.6); therefore, the ohmic drop can be controlled by changing the shape and size of the WE as well as the distance that separates the WE from the RE.

These approaches can minimize the ohmic drop but never completely eradicate its presence.

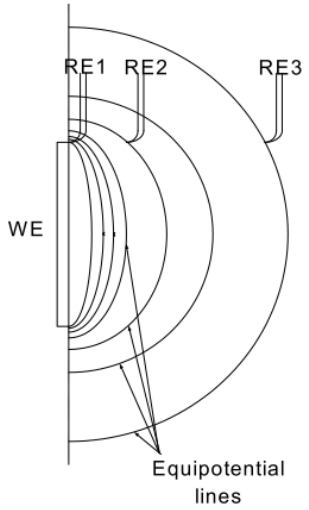

Figure 2.6: Equipotential lines for different positions of the RE with respect to the WE. As the distance separating the WE and the RE increases (RE2 and RE3), the ohmic drop also increases. (retrieved from [41])

2.3 Nanotechnology

With the recent development in the nanotechnology field, many novel nanomaterials with improved properties, compared with bulk materials (materials without nanoscale features), are being discovered. By definition, nanomaterials are engineered particles used at a nanometric scale, 1–100 nm in at least one dimension [42]. The chemical, electrical and mechanical properties were found to be affected by the substance size, so nanomaterials exhibit remarkable advances when faced with materials with larger-scale particles [43]. With that said, this emergent field of nanotechnology has become the foundation for innovative applications in varied areas such as agriculture, nutrition, engineering, and medicine [18].

Regarding the biosensing field, the inclusion of nanomaterials in its devices has been actively investigated, and there has been a notable merge between biological sensing and material science areas over time [44]. Nanomaterial-based sensors are essentially developed by incorporating nanomaterials into compatible substrates with the desired characteristics. Nanomaterials can be divided into different classes based on specific criteria, such as dimensionality, morphology, state, and chemical composition [42]. Biosensors could easily integrate carbon-based and metallic nanostructures in their chemical composition since they present good catalytic properties, making them the ideal electrode substrate for non-enzymatic biosensing. Here, the significance of carbon-based materials and metallic nanostructures will be highlighted, specifying graphene and copper nanoparticles (CuNPs).

2.3.1 Graphene

Carbon nanostructures continue to attract significant interest across several fields, including sensors, high-speed electronics, and storage applications [45]. Carbon materials appear in different dimensions, such as amorphous carbon, graphite, diamond, carbon nanotubes, and the more recent discovery, graphene [46]. Among these various carbon forms, the increased graphene-based sensors' quality raised interest in these nanostructures.

The isolation of graphene was first discovered in 2004 by two researchers at The University of Manchester, Professor Andre Geim and Professor Kostya Novoselov, who were later awarded the Nobel Prize for their pioneering work. This carbon sheet is defined as a monolayer of carbon atoms packed into a benzene-ring structure, with a space of 0.142 nm between them [47], and it has emerged as the most promising candidate to be used in stretchable and flexible devices. Graphene has gained much attention due to its excellent physical properties, such as extraordinary strength, lightweight, flexibility, and superior electrical conductivity. Its enormous potential has had a massive impact in such different fields: food waste reduction, coatings, bendable devices, storing energy are some examples of graphene applications [48].

Several approaches to synthesise graphene have been reported. These can be divided into two different types of methods (Figure 2.7):

- Bottom-up: that uses carbon precursors submitted to high temperatures to create graphene (chemical vapour deposition, epitaxial growth, laser-induced graphene, *etc.*);

- Top-down: that involves breaking stacked graphite layers to form graphene monolayers (exfoliation, arc discharge, unzipping graphene nanotubes, *etc.*) [49, 50].

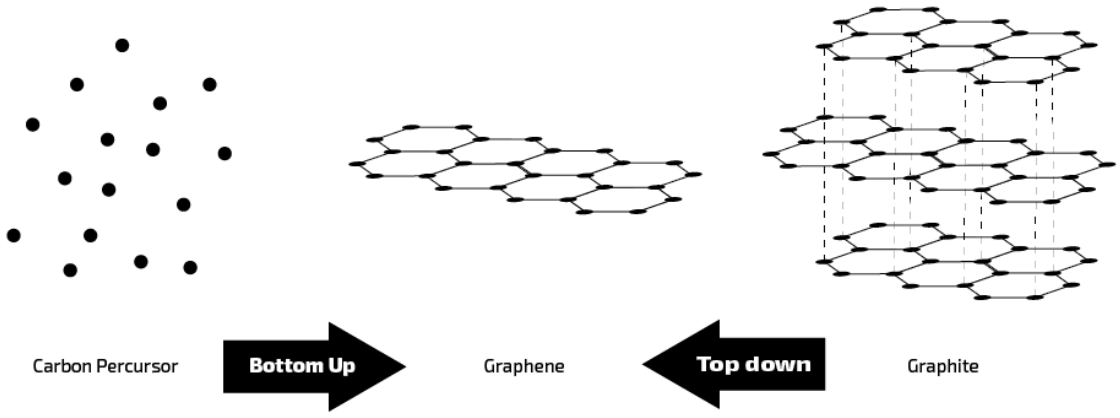

Figure 2.7: Schematic of different graphene synthesis methods.

Both categories present their advantages and challenges. In general, top-down techniques do not require expensive equipment, but they lack consistent conformation of graphene. Despite bottom-up methods needing sophisticated infrastructure, they allow the production of more high-quality graphene and direct growth on specific substrates, convenient for several applications [49, 51]. Depending on the final application of graphene, the most suitable synthesis technique can be selected, maximising its strengths.

2.3.1.1 Laser Induced Graphene

Regarding flexible and stretchable materials, printing processes such as screen printing [52], inkjet printing [53], and laser induction [54] have received tremendous attention in recent years due to their excellent compatibility with flexible systems. These printed electronics are highly sensitive functional inks containing soluble or dispersed materials and can be attainable at a low manufacturing cost.

For biosensor application, the most attractive synthesis technique and also the elected one for the development of several graphene electrodes has been Laser-Induced Graphene (LIG). The simple, rapid and non-chemical synthesis based on LIG have led to the development of several laser engraved graphene electrodes such as strain sensors [55], gas sensors [56], pressure sensors [57], and glucose sensors [37, 58, 59].

LIG is a technique that creates highly conducting graphitic carbon patterns, based on a three-dimensional printing technology, Laser Direct Writing (LDW), that allows for localised cut, ablation, or conversion of materials [60] (Figure 2.8).

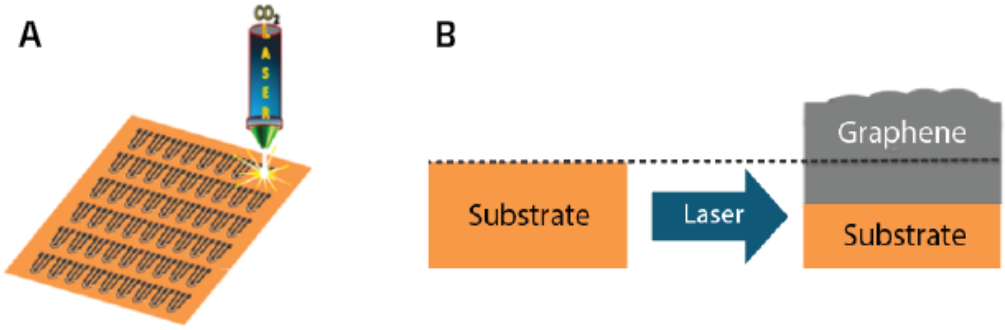

Figure 2.8: LIG formation. A) Fabrication of a 3-electrode LIG pattern array (adapted from [37]). B) Schematic of graphene formation using the LIG process.

With this method, it is possible to construct structures with high resolution and accurate control of the patterning by irradiating a polymer surface with a CO_2 laser source. A photothermal and photochemical transition will convert the irradiated substrate to graphene when the laser reaches the material's surface. Its discovery, published in 2014, uses a CO_2 infrared laser to convert sp3-carbon atoms into sp2-carbon atoms of a polyimide substrate in ambient atmospheric conditions. The energy resulting from the pulsed laser irradiation provokes a photothermal reaction, breaking C-O, C=O, and N-C bonds

of the polymer and forming stacked graphitic structures with high electrical conductivity. By moving the laser according to a previous computer-designed vectorised model, it is possible to produce graphene in customisable shapes and sizes. LIG has revolutionised printable electronics, once it can be patterned into detailed designs with delicate features and produce high-quality graphene with high surface area and electrical conductivity. Moreover, this technique allows for massive one-step production of electrodes at meagre cost and under ambient conditions [61], which could not be achieved with previous approaches.

LIG composition and morphology can be influenced by operational laser parameters, environment, and substrates [54]. In 2018, Chyan et al. [62] discovered that a wide range of materials can be converted into LIG. Heat-resistant plastics, such as poly(ether imide), were already known as possible substrates to be readily converted into LIG. Howerever, it was proved that other carbon precursor materials that can be first converted into amorphous carbon, such as paper, can be further converted into LIG with following laser scans. The same study described two different methods of attaining multiple lasing: by irradiating the substrate multiple times with the moving platform positioned on the focal plane or by defocusing the laser in order to increase its spot size and create overlapped laser spots. Figure 2.9 illustrates this second method.

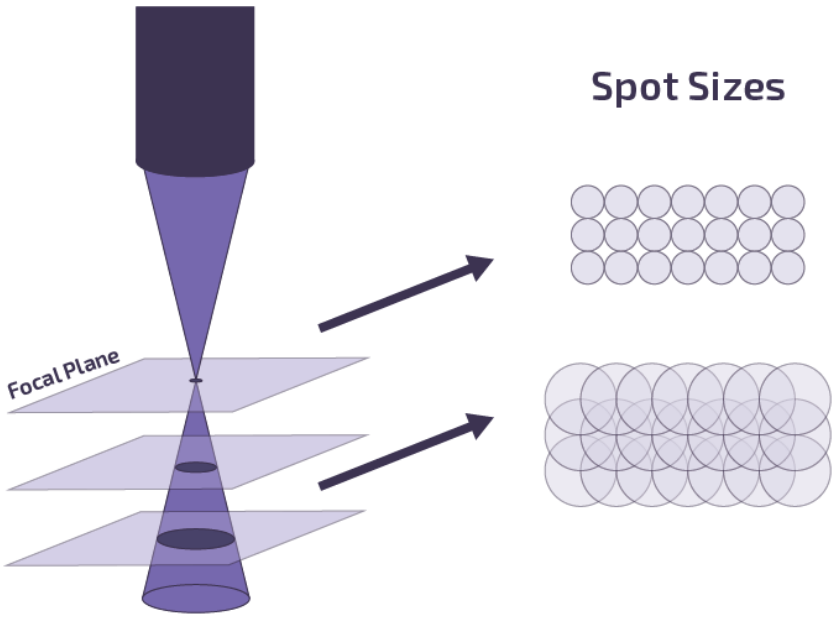

Figure 2.9: Schematic of the influence of laser height variation in its spot size.

Since the laser irradiation area is conical, the substrate area exposed to the laser beam increases as the z platform moves away from the focus plane. This way, spot sizes that with the laser at focal point were smaller, now are larger, which creates overlaps between them, resulting in multiple scans. This defocus can be attained by either lowering or

ascending the platform.

2.3.2 Copper Nanoparticles

Metallic nanoparticles have now been a focus of interest due to their unique properties, such as biocompatibility with several materials, easy production, and excellent catalytic activity. Some of the most well-explored metals used to develop these nanostructures are gold [63], silver [64], copper [59], iron [65], platinum [66] nickel [67].

The focus of investigating glucose detection methods based on enzymes is being switched to non-enzymatic alternatives. Metallic nanoparticles and their oxides arise as active substances capable of directly oxidizing glucose on the electrode surface. Among metallic nanoparticles, copper, a transition metal, is more attractive than expensive noble metals, such as gold and silver. Physical characteristics, such as size and shape, are highly dependent on their synthesis method and precursors used [68] and can influence the catalytic activity of CuNPs.

Recently, copper-based nanomaterials (Cu, CuO, Cu_2O, etc.) have been included in several electrodes for glucose sensing, and many researchers have investigated their ability to effectively improve sensors' performance. Cu-based nanomaterials take advantage of their capability of rapid glucose detection due to their excellent benefits such as increased surface area, which increases the rate of the glucose oxidation reaction, low toxicity, high sensitivity, and good stability [69].

To fully understand the glucose electro-oxidation mechanism, Figure 2.10 A) shows the commonly accepted principle behind the excellent catalytic reaction of CuNPs-based electrodes towards glucose. During CV scanning in alkaline solution, a chain of reactions can occur on the electrode surface, changing the initial form of copper to different copper oxidation states, and further oxidation of those species to Cu(III) may occur. For clarification, all species containing Cu^{+3} are labelled as Cu(III) and the same is valid for the other copper oxidation states. Since Cu(III) complex is extremely reactive, this species is rapidly reduced back to Cu(II). In the absence of glucose, reactions 2.9 and 2.10 describe this mentioned process [70].

$$Cu(II) \rightarrow Cu(III) + e^- \tag{2.9}$$

$$Cu(III) + 4OH^- \rightarrow Cu(II) + 2H_2O + O_2 \tag{2.10}$$

W. Zheng et al. [71] proposed that the oxidation of Cu(II) may take a different path when both Cu(II) and glucose are present. Instead of reacting with the diatomic anion OH^-, the Cu(III) species takes another path, which is energetically favorable, by oxidizing glucose.

$$Cu(II) - glucose \rightarrow Cu(III) - glucose + e^- \tag{2.11}$$

$$Cu(III) - glucose \rightarrow gluconolactone + Cu(II) \tag{2.12}$$

Thus, negatively charged glucose (glu^-) complex is formed (because glucose loses one proton to the diatomic anion OH^-) to be further combined with the Cu(II) species and create the Cu(II)-glu^- complex. At this point, since the energy barrier for the oxidation of Cu(II)-glu^- to Cu(III)-glu^- complex is lower than that of the Cu(II) to Cu(III) transition, as shown in Figure 2.10 B), the path via glucose oxidation is preferable. During the same stage, Cu(III) is reduced to Cu(II), catalyzing glucose's oxidation into gluconolactone, a more stable compound.

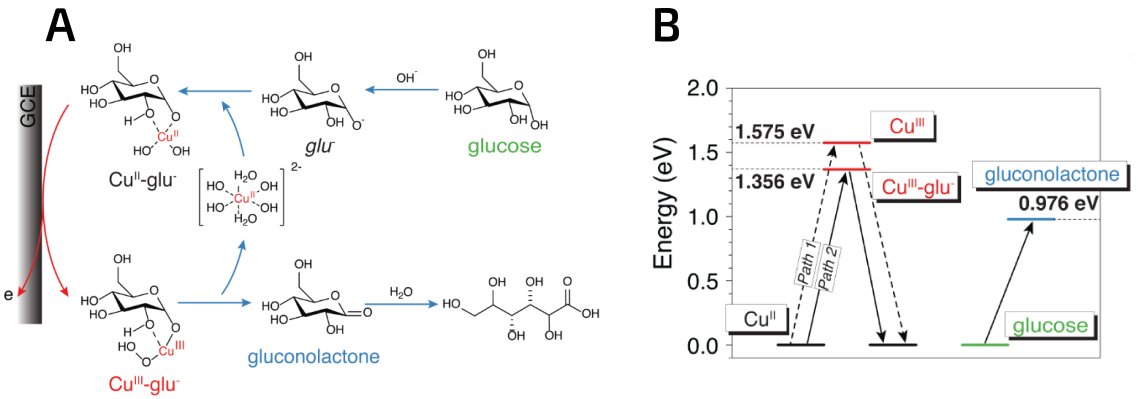

Figure 2.10: Glucose detection system with a CuNPs-based sensor. A) Mechanism of glucose oxidation with the presence of glucose. B) Energy barriers to Cu(II) oxidation, without (path 1) and with (path 2) glucose. Adapted from [71].

When glucose is added, there is an acceleration of the oxidation of Cu(II) to Cu(III), which will be reflected in a current increase. So, the working principle of every CuNPs-based sensor is measuring that current response and correlating it to a glucose concentration. It can be said that the mechanism of the electrocatalytic oxidation process of glucose is possible due to the changes of copper/copper oxides oxidation states and that the Cu(III) species is the primary catalyst in this process [69].

2.4 Paper

Over the past few years, a notable growth of environmental awareness and multiple incentive policies related to a sustainable economy have contributed to companies evolving towards developing "greener" products. Due to some desired paper characteristics, such as cost-effectiveness, flexibility, biodegradability, and non-toxicity, paper has been selected as the substrate to construct several applications [7]. For example, Lab-on-Paper technology, which has been recently widely explored, appropriates paper advantages to develop microfluidic devices for point-of-care testing [72]. Regarding flexible electronics, paper has been used for the fabrication of several electronic devices such as supercapacitors, electronic skin, and sensors [8, 73].

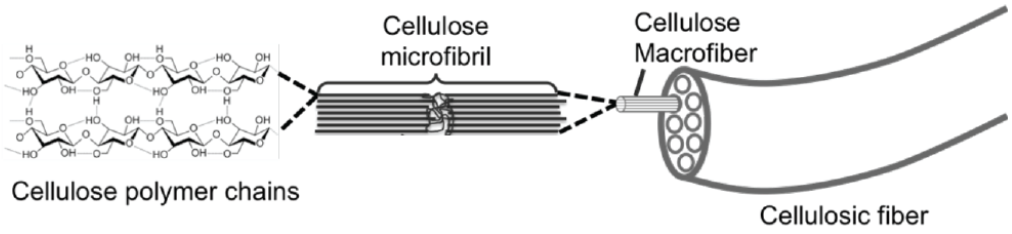

Figure 2.11: Chemical cellulose composition. Cellulose is an organic compound composed of several glucose monomers, linked together to form a chain (adapted from [74]).

Concerning its composition, paper is a thin sheet mainly composed of pressed cellulose fibres, which is the most abundant organic compound on the planet and is synthesised by multiple living organisms. Cellulose fibres are chemically connected through hydrogen bridges to create a 3D random network (Figure 2.11). Depending on the origin of cellulose and the paper manufacturing process, different types of paper with specific characteristics, such as surface area, capillary flow rate, porosity, and thickness [75], can be made. According to its final application, the type of paper to be used can be selected based on the desired features. Based on the cellulose source used to create paper fibres network, two main possible paper raw materials are wood, used to produce the commercial printing paper, and cotton, which generates purer paper, such as filter and chromatography paper [76].

2.5 Glucose monitoring in sweat

Although glucose level detection is nowadays mainly assessed in blood, with finger-prick tests, alternative non-invasive methods are being developed using other body fluids. Among several candidate biofluids that can be used as a sampling medium for glucose sensors, interstitial fluid, tears, saliva, and sweat are the most common. Regarding sweat, glucose concentration is approximately two orders of magnitude lower than the concentration detected in blood (10-200 μM in sweat vs 2-30 mM in blood [4, 77]), so selectivity and sensitivity of the electrodes present in these sensors must be highly refined [78].

Sweat is an epidermal biofluid that is involved in homeostatic functions such as thermoregulation and skin regulation [79]. Also, it can provide a wealth of chemical information that can have a particular interest in non-invasive techniques for biomolecular state analysis of human bodies [77]. Lactate, ethanol, glucose, Na^+ and Cl^- ions, uric acid and ascorbic acid are examples of some analytes that can be found in sweat. There are several applications developed based on sweat analysis such as cystic fibrosis diagnosis [80], drug abuse detection [81], and glucose sensors [82].

There are three types of sweat glands: eccrine, apocrine, and apoeccrine. These sweat glands differ in several aspects, such as body location, structure, quantity, and secretory product composition. Eccrine glands occur in more significant numbers and occupy most of the body surface, being responsible for the major portion of the secreted sweat [83]. Sweat glands are distributed across all three layers of human skin in a non-uniform way. Each eccrine gland is a tubular structure composed of a secretory coil, where sweat is generated initially, and a straight sweat duct that connects the epidermis to the skin surface [84] (Figure 2.12).

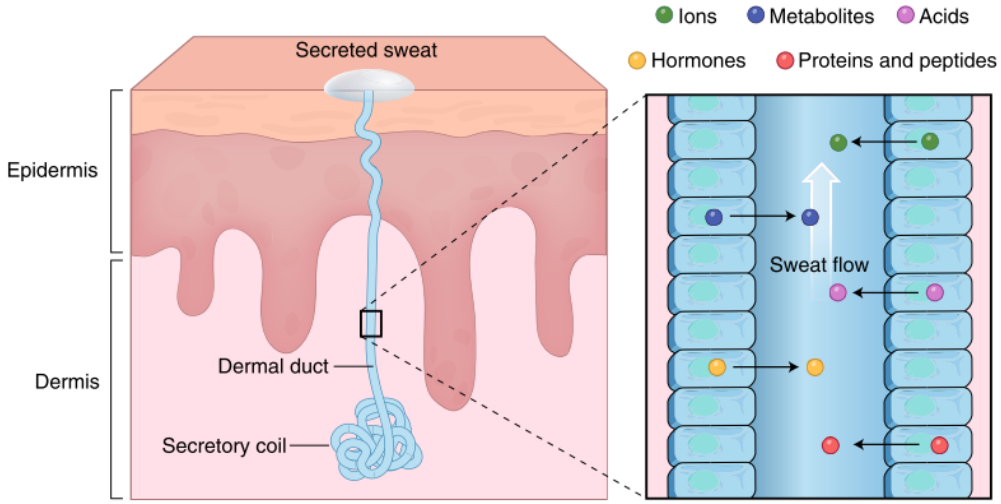

Figure 2.12: Representation of an eccrine gland highlighting analyte diffusion to its sweat duct (retrieved from [77]).

Perspiration, along with skin vasodilatation, is a vital mechanism in maintaining body temperature constant under high-temperature conditions, preventing the body from entering into a hyperthermia condition. When the Sympathetic Nervous System is activated, sweat glands stimulate sweat production. As the secreted product reaches the skin surface, its evaporation allows for the release of thermal energy, enabling a reduction in skin temperature [85]. Rather than hot environments, sweat can also be stimulated due to emotional stress, physical exercise, spicy food, or intentionally by sweat-inducing agents. However, the selected sweat-inducing method can modify sweat composition. Sweat induced through physical exercise shows an increased metabolic activity that does not reflect sweat composition in resting and "pure" state [86]. With that said, sweat-based Wearable Sensors (WS) frequently include iontophoresis interfaces, which use sweat-inducing agents to stimulate the production of sweat in individuals in a resting state [80].

3

State of the Art

As of today, finger-prick blood tests to determine glucose levels still dominate the glucose sensor market. In this method, glucose detection is made through an enzyme-catalyzed reaction, where glucose oxidase (GOx) reacts with glucose, releasing electrons. Through an electrode, the induced current is measured and then converted to blood glucose values [87]. Despite this being the most used and standard glucose test, these sensors present several disadvantages, being the invasive character of the finger prick one of the most significant. Moreover, the cost of this procedure is increased by expensive enzymes and all fabrication methods, preventing access to part of the world's population [37]. Therefore, there is a significant demand for alternative glucose detection methods that do not cause pain, infection, or discomfort to their user. At the same time, it is essential that those methods are affordable and can be deployed in developing countries. To face the disadvantages associated with this method, the evolution of glucose sensors is now moving towards a non-invasive, non-enzymatic, and low-cost glucose detection.

The alternatives to glucose test strips began to appear in innovative ways, focusing on non-invasive methods of collecting biofluids for glucose measurement, as is the case of GlucoWatch (Figure 3.1 A), commercially approved in 2001. This wristwatch used reverse iontophoresis to extract the interstitial fluid through the skin and, at the same time, incorporate a sensor to detect glucose [25]. Although this was a widely well-known device, it had related problems such as skin irritation caused by the electric field applied, so the device was retrieved from the market. Other body fluids were further studied, and different applications started to appear, such as sensors for tear glucose measurements [88, 89] (Figure 3.1 B), salivary glucose sensors in forms of toothbrushes [90] (Figure 3.1 C) and mouthguards [91], and sweat-based sensors including wearable smart wristbands [86] (Figure 3.1 D) and screen-printed tattoos [92].

The discovery of graphene, and later the LIG, boosted the development of new sensors since its unique mechanical, electrical, and optical properties made it a staple component in almost all conventional detection mechanisms. In 2007, Schedin et al. [93] reported the first sensor made of graphene used to detect gases, followed by the development of the first graphene-based glucose sensor, in 2009, by Shan et al. [94], that used glucose

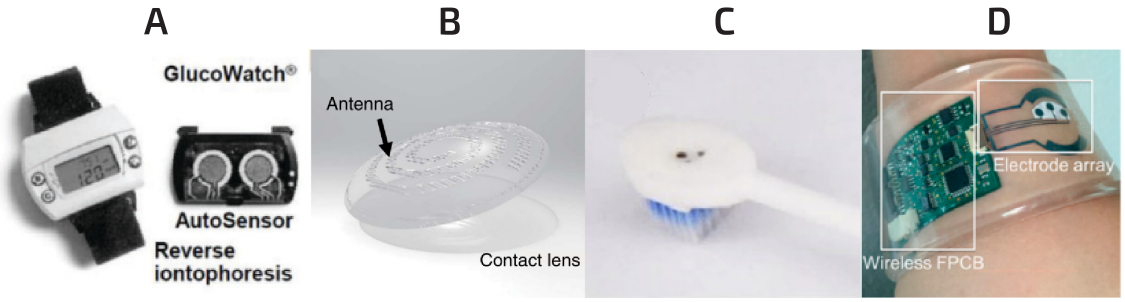

Figure 3.1: Glucose sensors based on different fluids. A) Optical image of GlucoWatch system (reproduced from [78]). B) Schematic of a transparent glucose sensor on contact lens (reproduced from [89]). C) Smart toothbrush with electrochemical sensor for saliva glucose detection (reproduced from [90]). D) Smart wristband a multiplexed sweat monitoring sensor (reproduced from [80]).

oxidase as the glucose oxidizing agent. With the entrance of graphene in the biosensing field, sensors' performance has improved, and the number of published articles reporting glucose sensors has been increasing since then.

Literature reports both enzymatic and non-enzymatic electrochemical biosensors. These two types of sensors have their advantages and disadvantages attached, although the most recent signs of progress include a non-enzymatic mechanism for glucose detection.

Enzymatic sensors have suffered a tremendous evolution over time; their timeline initiates with the first enzyme electrode developed in 1962 [95] and progressions to overcome related issues have led to the third generation of enzyme-based biosensors (Figures 3.2A, 3.2B and 3.2C). In glucose detection, enzymatic sensors depend on enzyme immobilization to make them specific to glucose, using modified enzymes, enzyme immobilization methods, or by application of enzyme stabilizers [25]. The majority of commercialized electrochemical glucose sensors are enzyme-based in their nature, using mostly either GOx or glucose dehydrogenase as a catalyst for glucose oxidation at the electrode surface [96]. Both enzymes have demonstrated advantages and disadvantages in their use. Although GOx reveals high selectivity and stability, the detection of glucose concentration is compromised in humid and hot environments, as well as in extremely high or low pH values. In glucose dehydrogenase, higher activity advantages are counterbalanced by challenges of reactivity towards other sugars, such as maltose and xylose [97]. Moreover, coupled with their high cost, enzymes can be degraded and their activity can gradually decrease, causing problems for the possibility of continuous glucose detection [98].

The upper mentioned problems related to enzyme-based technology applied to biosensors have led scientists to investigate other detection methods. With that said, enzyme-free sensors have received great attention in the past years. The basic principle of this type of sensor relies on the oxidation of glucose directly on the electrode, without the need of enzymes for catalyzing glucose, avoiding their shortcomings. This methodology is possible due to the incorporation of nanomaterials with catalytic properties that act as

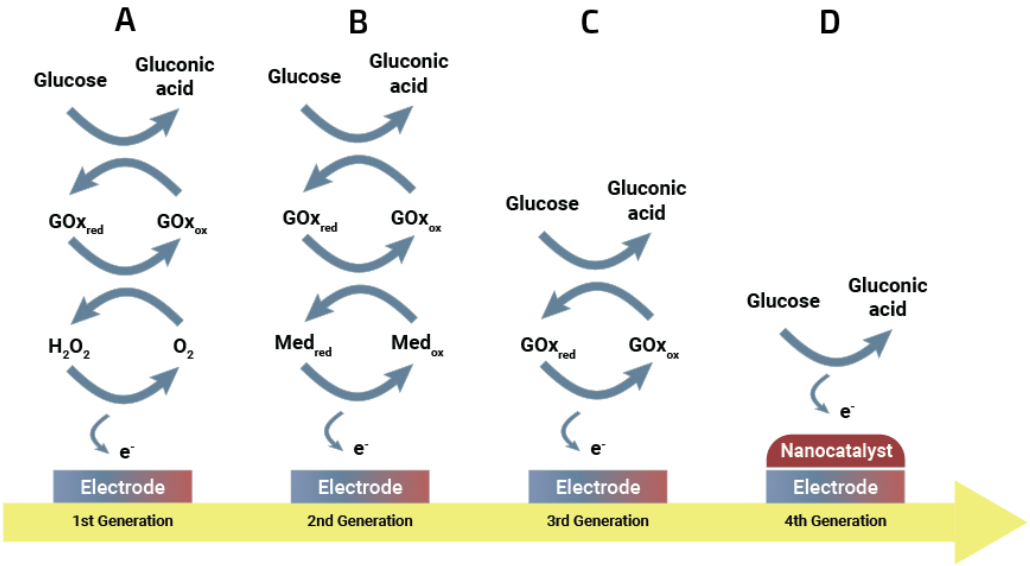

Figure 3.2: Evolution of different generations of electrochemical glucose sensors with their sensing principles. A) The first generation uses GOx to oxidize glucose to gluconic acid with a simultaneous reduction of O_2 to H_2O_2. B) In the second generation, O_2 is replaced by electron synthetic mediators that assist the electron transfer to the electrode surface. C) In the third generation GOx is directly immobilised to the sensing surface. D) Nanocatalyts incorporated into the electrode surface for non-enzymatic glucose detection.

electrocatalysts (Figure 3.2D). Electrocatalytic nanomaterials, including common metals, such as platinum [99], gold [63] and copper [100], are widely used in glucose sensors. Wei et al. [101] even consider those nanomaterials as "nanozymes", due to their enzyme-like activity. These catalytic nanoparticles can act as artificial enzymes, overcoming some limitations of traditional enzymatic sensors, such as pH and temperature constraints, expensiveness, and difficult large-scale production [96]. Nevertheless, non-enzymatic glucose sensors tend to have worse selectivity once their structure does not include any recognition agent.

With that said, the development of modified electrodes has been of paramount importance for the enhancement of electroanalysis devices. Several researchers reported non-enzymatic methods for glucose detection based on the combination of graphene with metallic nanoparticles [102–104]. The synergy between the high conductivity of graphene and the nanoparticles' catalytic properties has proven to improve electrochemical activity and electron transfer rate, resulting in a better sensitivity of glucose sensors. Once this project aims to develop a non-enzymatic glucose detection mechanism based on a CuNPs-LIG sensor, below there is a review of some sensors that conform with the desired characteristics.

One of the first studies including CuNPs in graphene electrodes for glucose sensing is the work carried out by Luo et al. [105]. For the WE, CuNPs were potentiostatically electrodeposited on graphene sheets, previously fabricated through the reduction

of graphene oxide. The sensor exhibited sensitive catalytic performance suggesting copper and graphene as possible and promising candidates for its use in glucose detection sensors. Another work that showed the synergetic effect between these hybrid materials was developed by Tehrani et al. [106], who used an electrodeposition method to form CuNPs on copper-graphene strips. The strips were fabricated by depositing graphene powder on a regular scotch tape as the adhesive substrate. The sensor pad was formed with copper tape, and then a Kapton tape was used as the passivation layer. After that, the sensor was further modified, depositing size-controlled CuNPs on the WE surface, where different applied voltages were tested to obtain the smallest nanoparticles and the greatest population density. A year later, a continuous study was published reporting a sensor based on LIG decorated with copper nanocubes, at this time using pulse electrodeposition [107]. Two of the main advantages of this sensor compared to the previous research are the possibility of engraving complex and miniature patterns of graphene with the LIG technique and the fact that this single fabrication step is easily scalable. Both works showed good sensitivity and low detection limit, confirming great catalytic functionality of LIG and copper-based sensors towards glucose.

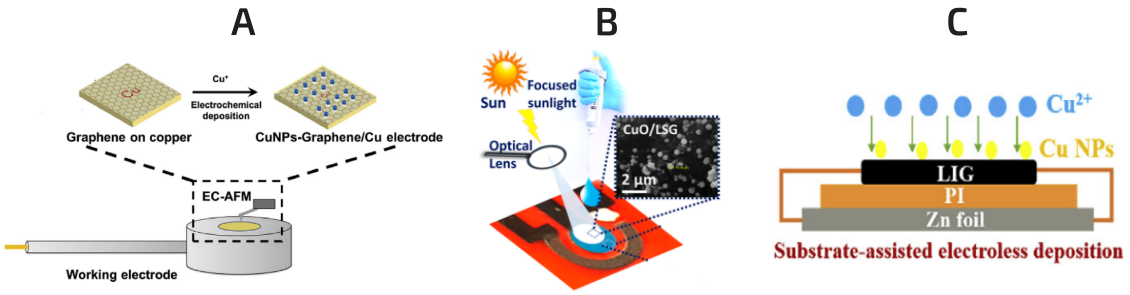

Figure 3.3: Different CuNPs synthesis approaches. A) Electrodeposition of CuNPs on a graphene/Cu electrode (reproduced from [108]). B) Deposition CuO nanoparticles using a focused sunlight technique (reproduced from [37]). C) Substrate-assisted electroless deposition technique for the formation of CuNPs-LIG composites (reproduced from [59]).

As these three examples, several more articles explore the electrodeposition technique (Figure 3.3 A) as a way of producing CuNPs to improve the ability of LIG sensors to catalyze glucose [70, 108–110]. Other approaches have been reported such as the production of a LIG electrode with anchored CuNPs based on a substrate-assisted electroless deposition technique, developed by Zhang et al. [59] (Figure 3.3 C). In this method, after the LIG formation, the electrodes were attached to a zinc foil using silver paste and encapsulated. By dipping the electrodes into copper sulfate solutions, CuNPs were formed through the substrate-assisted electroless deposition method, and to finalize, the zinc unified by the silver paste was removed. This methodology enabled glucose detection with good sensitivity, stability and selectivity towards common interferents. Prabhakaran et al. [37] developed a non-enzymatic glucose sensor compatible with human body fluids such as serum, sweat, and urine. The electrode was made of LIG and modified with copper oxide nanoparticles. After the LIG formation, a precursor salt was drop cast on the WE.

When the electrode was exposed to focused sunlight, CuO nanoparticles of optimized size were conformal deposited (Figure 3.3 B), which resulted in a significant improvement of the sensor catalytic efficacy towards glucose oxidation.

However, the upper-mentioned methods used to synthesize nanoparticles are either time-consuming or require complex procedures, which hinder the fabrication of the sensors. With that said, laser induction emerges as a promising method for nanoparticle formation. Concerning laser-induced production of nanoparticles-graphene composites, the literature reported scarce studies applying this concept for electrode fabrication until recent years. Some articles describe mixing poly (amic acid) with the precursor substance to coat the substrate that will later be exposed to laser to form one-step MnO_2 [111], MoS_2 [112] and Co_3O_4 [113] nanoparticles embedded on LIG electrodes. You et al. [114] developed a manufacturing process of metal (gold, silver, and platinum) nanoparticle-LIG nanocomposites converted from a polyimide film coated with the corresponding metal precursor-chitosan hydrogel ink. More articles reported this concept to synthesize nanoparticles with different nature; however, to what concerns the CuNPs-LIG nanocomposites formation, there have been few published studies in this field.

The first example is the work done by P. Peng et al. [115] in 2019, which resulted in the production of functional Cu/graphene flexible electrodes that were implemented in flexible heaters and planar antennas. The fabrication methodology was based on the application of LDW technique, where a continuous wave diode laser was focused onto a copper ion ink, drop-casted on a polycarbonate substrate, through a focusing lens. After washing the non-irradiated areas, the ink was dissolved, and the as-patterned Cu/graphene electrodes remained. In 2021, Liao et al. [116] reported a similar methodology to fabricate copper-graphene composites for microsupercapacitors, this time using a mixture of several reagents to form the copper ion precursor, which was then drop-casted in a glass or polycarbonate substrate. Another research [117] used $CuCl_2$ as the precursor for Cu and Cu_2O nanoparticles. After dissolving it in ethyl alcohol, the solution was spin-coated onto a polyimide film and submitted to the laser beam to form the copper nanoparticle-graphene nanocomposites. Lastly, the composites were transfered to a nickel foam surface to produce a graphene/Cu_xO-based electrode for electrochemical water splitting. The last work consisted of an in situ synthesis of copper–ruthenium nanoparticles on laser-induced graphene for the detection of hydrogen peroxide [118]. This was accomplished based on a three-step synthesis: a first LIG pattern on polyimide, followed by the deposition of a Cu^{2+} and Ru^{3+} precursor (to be adsorbed by the LIG porous structure) and finished with a second laser scanning.

Although these articles demonstrate the formation of CuNPs-graphene by laser irradiation (Figure 3.4), some of them describe several steps in their procedure until the nanoparticle's synthesis or to make them functional for their use in the final application. Thus one ends up losing the main advantage of this method which is obtaining these compounds in a fast and simple route.

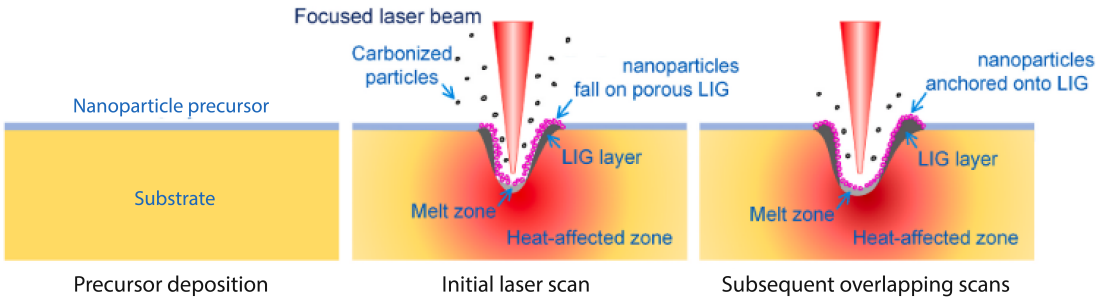

Figure 3.4: Illustration of the synthesis process of nanoparticles anchored on LIG by laser irradiation. Adapted from [119].

Regarding the support substrate, early studies suggested that only polymers structurally similar to polyimide could be converted into LIG, so the majority of published articles using LIG reports electrodes produced in polyimide substrate. However, polyimide presents some shortcomings related to its non-sustainability, higher cost and less accessibility when compared to other mundane materials such as paper. As mentioned before, in 2018, Chyan et al. [62] proved that, through multiple lasing, this technique allows the conversion of a wide range of materials into LIG, either through first conversion in amorphous carbon or direct conversion, in the case of polymeric carbon precursors. With that said, LIG can be produced on multiple substrates, such as renewable materials, including paper. Since this discovery, paper has been used as the carbon source for variable LIG-based applications in flexible and sustainable electronics context [120–123]. However, to date, just one article has yet been published regarding glucose sensing based LIG electrodes produced on paper substrate [38] and none reporting a non-enzymatic glucose detection method.

4

Materials and Methods

This chapter reviews the experimental techniques explored throughout this thesis. Firstly, the equipment necessary for the fabrication of LIG and CuNPs-LIG composites is described, followed by a brief description of the morphological, chemical, electrical and electrochemical equipment used to characterize the fabricated samples. Secondly, the methodology employed in the production of both optimization samples and sensors are stated.

4.1 Experimental fabrication and characterization equipment

4.1.1 Commercial CO_2 infrared laser system

The laser used in this work is a Universal Laser System (ULS) CO_2 VLS 3.5 (Figure 4.1 A), a desktop model system. This is a pulsed cutting laser, with a wavelength of 10.6 µm, associated with a plan-convex lens, with a focal distance of 50.8 mm and a spot size of 0.127 mm, as shown in Figure 4.1 B).

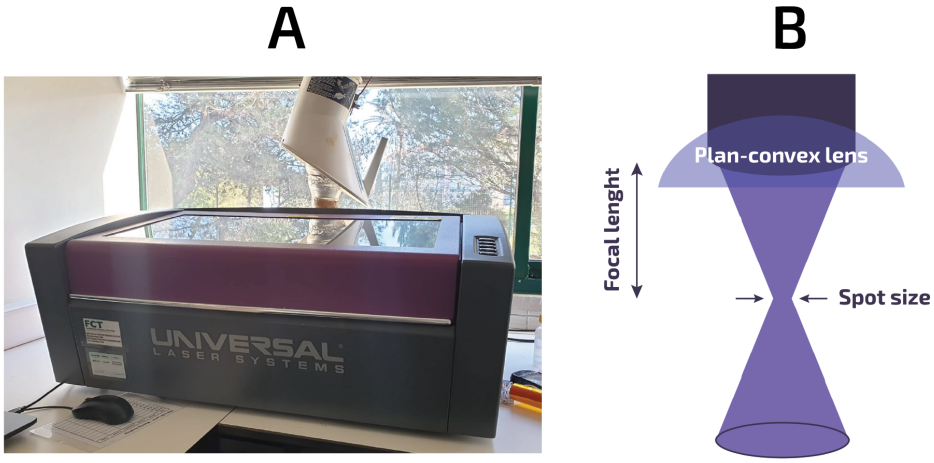

Figure 4.1: Universal Laser System CO2 VLS 3.5. A) Photograph of the desktop model and B) a schematic of the laser lens.

The laser setup is composed of a CO_2 laser, a beam delivery system contains three mirrors that guide the beam to a focusing lens and the moving stages (X and Y axes) that move according to the selected pattern, while the vertical positioning (Z-axis) is defined by a moving platform that supports the substrate (Figure 4.2).

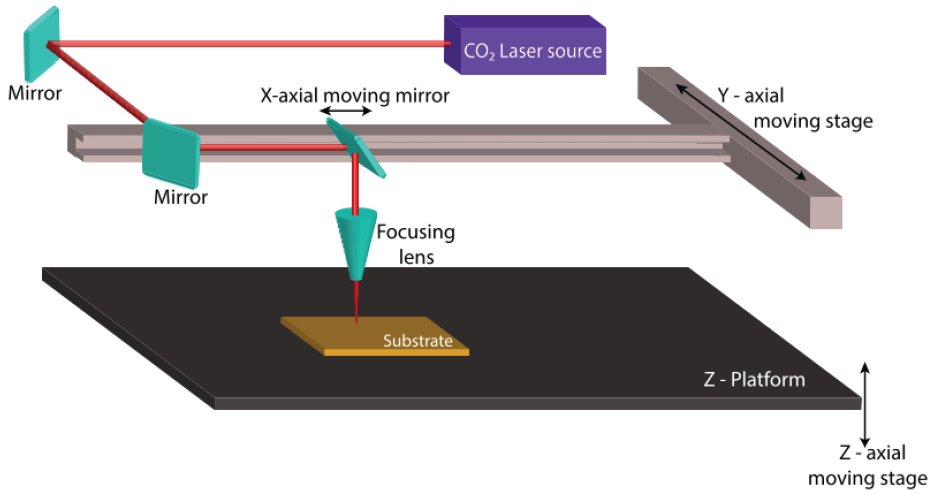

Figure 4.2: Schematic of the laser setup (retrieved from [124]).

The equipment is based on a computer-assisted system that can send a vectorial image input to be engraved onto a wide range of materials. Also, it comes with an interface that enables the user to select specific operation parameters such as laser power, PPI (number of laser pulses per linear inch), and scan speed, in the form of a Red, Green, and Blue (RGB) color map. The maximum operational values for this equipment's laser power and laser beam linear velocity are 50 Watts and 1.27 m s^{-1}, respectively. These two parameters can be modified by selecting smaller percentages of these maximum speed and power values in the engraving process. PPI has a maximum resolution of 39370 pulses per meter and can be altered by changing the repetition rate of the pulses in accordance with the speed.

This equipment can also operate in two different modes: raster and vector mode. In the raster mode, a previously selected vectorized model is engraved into a material at the maximum PPI value. This mode is usually preferred for engraving and photo imaging. In contrast, in the vector mode, the laser follows a two-dimensional path to cut or mark a shape into the material.

4.1.2 Characterization equipment

4.1.2.1 Scanning Electronic Microscope (SEM) and Energy Dispersive X-Ray Spectroscopy (EDS)

SEM is a widely used technique for morphological and compositional analysis of surface materials with high spatial resolution. The sample surface is initially bombarded with an electron beam emitted through a capillary tungsten filament, resulting in elastic and inelastic interactions between the beam and the sample atoms. Different mode types can detect different signals. Secondary electrons, resulting from inelastic interactions between the electron beam and the sample, can be detected through a Secondary Electron (SE) detector and are usually used to obtain topographical images of the sample's surface. Back-scattered electrons result from elastic collisions, coupled with changes of direction in the electrons' trajectory, can be detected through an Energy selective Backscattered (EsB) detector. This is a good technique for analyzing the distribution of the elements in a sample since the intensity signal is dependent on the element's atomic number (i.e., heavier atoms produce stronger electron scatters).

The EDS, which allows a chemical characterization of the samples, is usually attached to SEM setups. X-rays can be emitted through the atom's ionization, and the EDS detector can measure the energy of these X-rays. Sample mappings can be created with this information, reflecting the abundance and distribution of different present elements [125].

For this work, the models Hitachi TM 3030Plus Tabletop and ZEISS Crossbeam AURIGA FIB-SEM were used as SEM and Bruker QUANTAX EDS as EDS equipment, for the morphological and elemental sample's characterization (Figure 4.3 A).

4.1.2.2 Raman Spectroscopy

Raman Spectroscopy is a light scattering and high-resolution image technique used to determine chemical information about the material under study [126]. Raman uses a monochromatic light beam to interact with the sample to produce elastic/Rayleigh or inelastic/Raman scattering. In the first-mentioned situation, when the scattered light has the same wavelength as the incident light, the scattering does not contribute to the Raman spectrum beacause of an optical filter that reflects Rayleigh scattered light. In contrast, in the second situation, when the light is scattered with a different wavelength as the laser source, the energy difference of the laser photons is used to shift up or down in the molecule vibrational levels. This energy difference between the initial and final vibrational levels is characteristic of the sample chemical structure. The obtained plot that features characteristic peaks shows the intensity vs the wavenumber of the shifted light, corresponding to a specific molecular bond vibration [127].

In this work, the LabRAM HR Evolution equipment was used to obtain the Raman spectras (Figure 4.3 B).

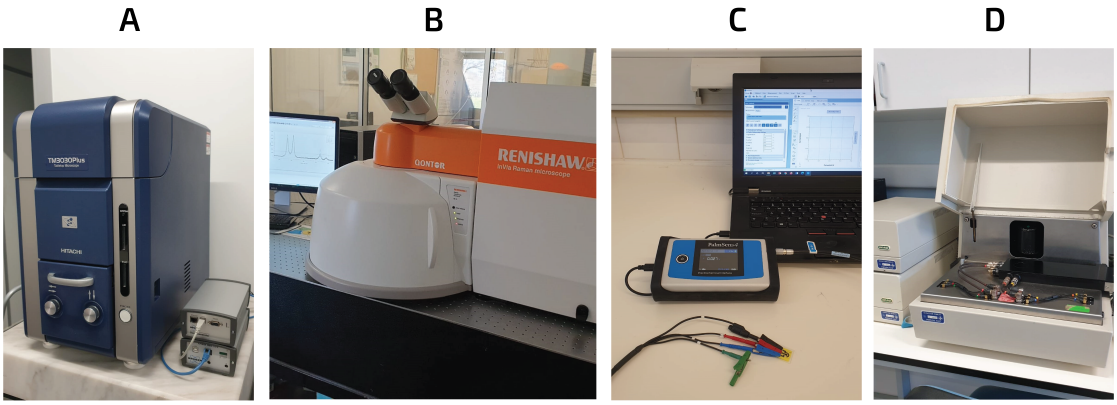

Figure 4.3: Characterization equipment used for the study of LIG and CuNPs-LIG composites. A) SEM and EDS equipment, B) Raman microscope, C) potentiostat and D) 4-point probe resistivity measurement device.

4.1.2.3 Potentiostat

A potentiostat is an analytical instrument that features two main function modes differentiated by the electric quantity that can be controlled. In the potentiostatic mode, a specific potential is applied, and the current that flows through the cell can be measured. The operation principle of the galvanostatic mode is precisely the opposite of the one described above. In this work, the PalmSens4 Potentiostat was used to electrochemically characterize the produced sensors (Figure 4.3 C). All experiments were performed using the potentiostatic mode with different measuring techniques, where the voltage difference between the WE and RE of the electrochemical cell could be controlled.

4.1.2.4 4-Point Probe

The four-point probe technique is a non-destructive technique widely used for determining the sheet resistance of a solid-state matter, as a measure to quantify its electrical conductivity. Current (I) is passed through probes 1 and 2 and voltages (V) is measured between probes 3 and 4. The process is then repeated for a different contact pair. Figure 4.4 illustrates the experimental arrangement for this sheet resistance measurement.

Sheet resistance is given by the following equation

$$R_{sh} = \frac{\pi}{2ln(2)}\left(\frac{V_{43}}{I_{12}} + \frac{V_{23}}{I_{14}}\right)F(Q) \tag{4.1}$$

, where F is a correction factor for geometrical asymmetry, obtained by reference to graphs, that depends on the symmetry factor Q ($Q = \frac{V_{43}I_{14}}{I_{12}V_{23}}$).

In this work, the Accent HL5500PC Hall Effect Measurement System was used to measure the sheet resistance values of samples (Figure 4.3 D).

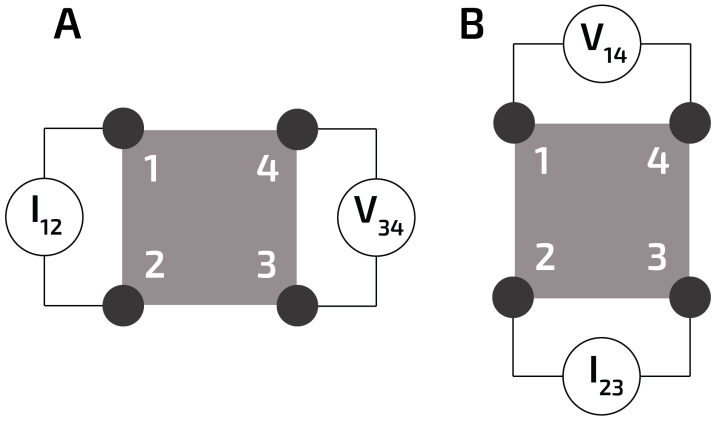

Figure 4.4: Sheet resistance measurement for a square probe configuration. A) First and B) second experimental arrangements of the current flow in the sample.

4.1.2.5 X-Ray Diffraction (XRD)

XRD is a non-destructive technique that provides detailed information about the crystallographic structure of materials. XRD works by irradiating a material with an X-ray radiation beam with different incidence angle and then measuring the respective intensities of the diffracted beam and scattering angles. Crystalline materials are composed by atoms arranged in a periodic array, that form distinct planes separated by a specific distance. Since the wavelenght of an X-ray is similar to the distance between atoms in a crystal, diffraction can be used to measure that distance. Diffraction occurs when light is scattered by repeated arrangement of atoms, producing constructive interference at specific angles. A diffractogram can be obtained by varying the incidence angle and each peak results from a corresponding distance between planes of atoms, which can be known through Bragg's Equation.

In this work, the PANalytical XPert PRO MRD equipment was used to obtain the diffractograms for CuNPs-LIG samples (Figure 4.5 A).

4.1.2.6 XPS

XPS is a surface analysis technique based on the absorption of X-rays by the atoms of the sample. The sample's surface is bombarded with an X-ray beam to excite the molecules present at the sample, which causes photoelectrons (electrons emitted due to the incidence of electromagnetic radiation) to release. The XPS spectra is obtained by counting these photoelectrons over a range of kinetic energies. By analyzing the energies and intensities of the peaks that are visible in the plot, this technique allows for the identification and quantification of the surface elements as well as the determination of their oxidation states.

In this work, the Kratos Axis Supra XPS equipment was used to characterize LIG and CuNPs-LIG composites (Figure 4.5 A).

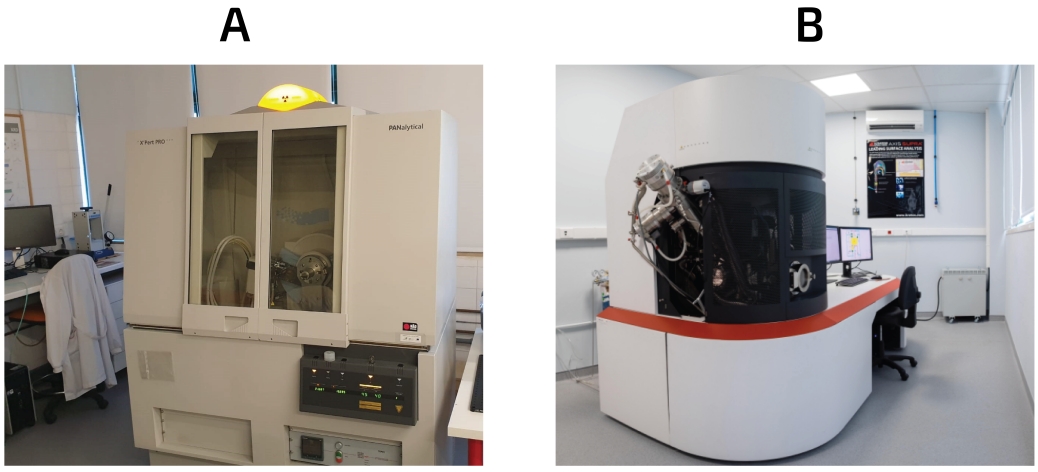

Figure 4.5: Characterization equipment used for the study of CuNPs-LIG composites. A) XRD and b) X-Ray Photoelectron Spectroscopy (XPS) equipment.

4.2 Experimental procedure

4.2.1 Substrate preparation

Whatman paper was selected as the substrate for the LIG formation since previous studies suggested better chemical, electric and kinetic graphene properties when compared to commercial office paper [38].

Firstly, a sheet of Whatman paper was cut into standard A6 size pieces. Before submitting these sheets to the laser beam, they were first treated with a fire-retardant, a sodium tetraborate solution, to prevent chemical degradation. Adding a fire-retardant to the chromatography paper will prevent it from burning at approximately 230 °C, by promoting dehydration and oxygen elimination reactions, which will result in an amorphous char resistant to laser ablation [120]. Therefore, these paper sheets were immersed in a container containing 0.1M of this solution for 10 min each side and then were placed at room temperature until completely dry.

Next, a wax printer was used to print a solid yellow wax layer in the previously treated paper to attain a hydrophobic form. The waxed paper sheets were then placed in a hotplate at 120 °C until they became semi-translucent, meaning that the wax was properly widespread; this process of completely melting the wax took about 1 min.

Since the paper treatment with sodium tetraborate made the paper wavy, the last step before exposing it to the laser beam was to tape-fix the prepared paper into a glass plate. This process allowed to fix the substrate only on one plane, so once the laser focuses on the paper, the conversion to LIG occurs uniformly at the same height.

4.2.2 Optimization matrices

Here the first step of the work will be described, which consisted in the production and optimization of LIG and CuNPs-LIG composites by exploring which laser parameters led to the formation of the desired materials without compromising the substrate.

4.2.2.1 LIG optimization

Initially, optimization matrices were created to investigate which laser conditions led to LIG formation without destroying the paper substrate. Matrices were generated at different heights and with different numbers of laser scans, by varying the laser power and speed percentages within a range of 1-8 %, which correspond to a variation of 0.5 to 4 W and 0.00127 to 0.1016 m s^{-1}, respectively. Matrices were created by small squares, with 2 mm per side, previously designed using a vector image software (Adobe Illustrator, Adobe Systems software). Each matrix row maintained a constant speed while varying different powers and for the columns vice versa, as shown in Figure 4.6.

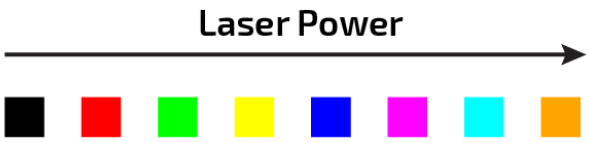

Figure 4.6: Representation of a row in the LIG optimization matrix. The different colors represent different laser powers to be printed in the substrate.

After observing which speed and power combinations led to LIG formation without compromising the substrate integrity, those conditions were used to fabricate LIG samples to be latter characterized.

4.2.2.2 CuNPs and LIG optimization

First it is important to mention that in this section the substrate used was the same as the described in Section 4.2.1, except that the yellow wax layer was printed on paper with blank squares, which would be later occupied by the copper precursor solution. The barriers created by the melted wax allowed the solution not to disperse over the substrate.

For the purpose of the CuNPs synthesis, the reagent copper(II) sulfate pentahydrate ($CuSO_4 \cdot 5H_2O$) was selected as the precursor. Initially, a solution of 0.8 M was prepared with deionized water and then diluted two times to additionally obtain two other concentrations, 0.08 M and 0.008 M. To study different possible combinations of volumes and concentrations, a matrix with these two variables was made. For this step, three different volumes of copper sulfate solution were selected, 50 μL, 100 μL and 200 μL, to be pipetted into 2 cm long and 1 cm wide rectangles. The prepared samples were left to dry at room temperature until completely dry. After this procedure, it was decided to add an intermediate volume of 150 μL for the following experiments.

For the formation of CuNPs-LIG composites, copper precursor solution was pipetted into 4 mm wide squares delimited by infused wax. In this step and other phases of the development of this thesis, the volume of copper precursor solution had to be adjusted because different characterization techniques required different sample areas. Therefore, throughout this document, the copper precursor volume to surface area ratio (VA ratio) will be used for the reader's better understanding. With that said, the copper sulfate solution VA ratio of 0.25, 0.5, 0.75 and 1 μL mm^{-2} corresponded to the 50, 100, 150, and 200 μL initial optimization rectangles, respectively. Figure 4.7 shows the synthesis process of CuNPs-LIG composites, through laser induction.

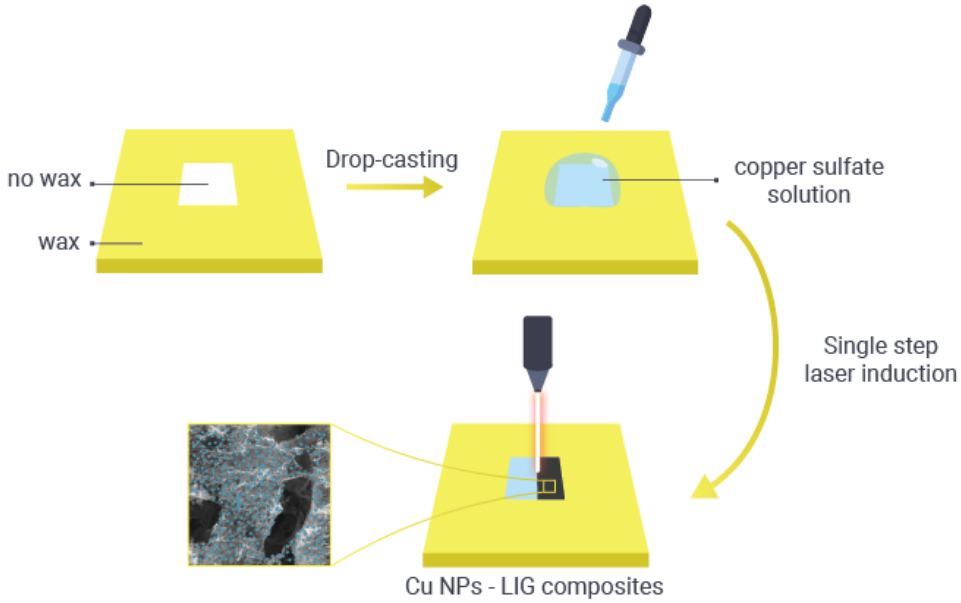

Figure 4.7: Schematic illustration of the steps for the fabrication of CuNPs-LIG composites.

The methodology used to fabricate the CuNPs and LIG matrices were similar to the one described in the sections above. The optimization matrices were created for different combinations of power and speed, and for each of the copper precursor VA ratios. The laser was used to create 5 mm squares overlapped with 4 mm squares with the copper sulfate solution. A simple visual analysis allowed to discard the conditions that perforated the substrate, reducing the sample quantity to characterize.

4.2.3 Sample characterization

All samples were characterized using the following characterization techniques, except the XRD measurements, that were just performed on the CuNPs-LIG samples.

4.2.3.1 Sheet resistance measurements

All the conditions that led to the formation of graphene were selected to analyze each sheet resistance value afterward. For the LIG optimization, samples were replicated in bigger squares, with 5 mm on each side and, for statistical purposes and reproducibility assurance, each LIG square was produced four times for each laser parameter. For the CuNPs-LIG optimization, only one measurement was performed for each laser parameter combination and copper precursor conditions due to the longer sample fabrication process. Silver ink contacts were deposited on four vertices of each square to improve the contact with the probes of the equipment used to determine the sheet resistance. To better control the shape and amount of silver ink deposited on each vertex, a plastic mask with the desired circle pattern was made using the CO_2 laser (Figure 4.8); this mask was placed over the squares for the later ink application.

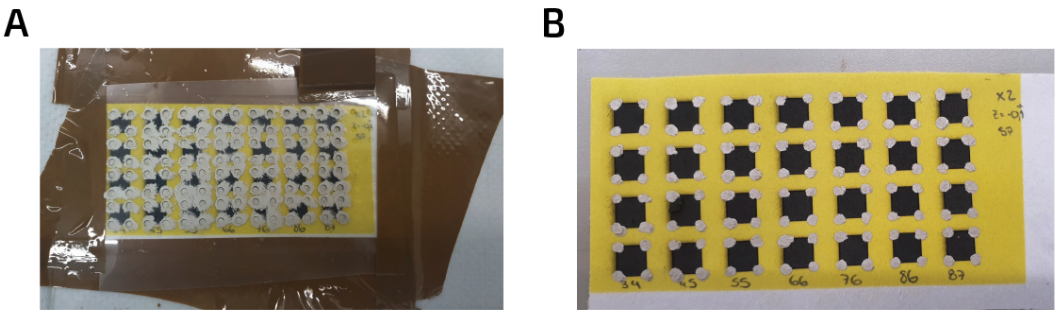

Figure 4.8: Preparation of LIG samples for electrical measurements. LIG square samples A) during and B) after depositing silver ink on the square vertices, using a plastic mask.

After applying silver ink, the samples were left to dry in a hotplate at 65 ºC for 30 minutes. This approach resulted in a rapid method for mass sample production and, at the same time, guaranteed less variability between the LIG squares. For the sheet resistance measurement was used a four-point probe equipment. The samples to be measured were attached with tape to a glass plate and then inserted into the equipment. Then, the four probes were put in contact with each vertice containing silver ink, and measurements were made (Figure 4.9).

4.2.3.2 SEM and EDS measurements

Since this method of measuring sheet resistance is a non-destructive technique, samples were reused to perform morphological and chemical characterization, except the XRD analysis, which required samples with a larger area. Tabletop SEM Hitachi TM3030Plus was used to morphologically analyze the surface of the LIG samples. Images were taken with 15 kV of accelerating voltage and with the SE detector.

Considering the CuNPs-LIG samples, the aim of this part of the study was to investigate whether there actually was a conversation of the copper precursor solution to copper

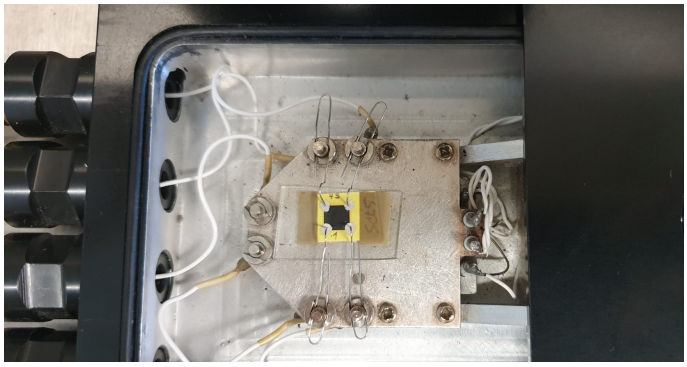

Figure 4.9: Setup for sheet resistance measurements.

agglomerates with the laser pass or not. For this purpose samples were analyzed in the ZEISS Crossbeam AURIGA FIB-SEM, since this equipment provided a better resolution. This time, images were taken with 5 kV of accelerating voltage and with the SE and EsB detectors. The preparation of both types of samples was based on gluing them to the SEM holder with double-sided carbon tape and adjusting the height holder to facilitate the image focusing.

This study was complemented by the information acquired from the Bruker QUANTAX EDS equipment, where the relative elemental composition of the samples was examined three times for each sample. The measurements were performed with the sample focus and magnification obtained from the SEM images, during 60 s.

4.2.3.3 Raman measurements

Raman spectroscopy analysis was performed on LIG and CuNPs-LIG samples fabricated with the final optimized conditions to evaluate the quality of the LIG structures. The equipment used was the inVia confocal Raman microscope. Raman spectras were obtained using a laser with 532 nm of wavelength, for 10 seconds, 3 cycles with a 10 % power.

4.2.3.4 XRD measurements

The X-ray diffractometer (PANalytical X Pert PRO MRD) was used to characterize CuNPs-LIG samples by assessing their crystallographic structure. For this purpose, sample squares with 1 x 1 cm were fabricated using the different copper precursor VA ratios. Measurements were performed using incident angles ranging from 10 to 90 degrees, with a scanning step of 0.33 degrees in a continuous scanning mode and operating at 45 kV with 45 mA.

4.2.3.5 XPS measurements

XPS analysis was performed on LIG and CuNPs-LIG composites to determine the hybridization of carbons and the copper oxidation states of the elements present at the

sample surface. The Kratos Axis Supra XPS was used to obtain the XPS spectras using an X-ray power of 150 W and a 10.00 mA emission current.

4.2.4 Sensor fabrication

For this work, two types of sensors were produced: the first was based on LIG and was fabricated to electrochemically characterize the electrodes; the second one, composed by CuNPs and LIG was fabricated for the glucose electro-oxidation. Both types of sensors were produced based on the same methodology, apart from the substrate preparation. The LIG-based sensor used Whatman paper treated with sodium tetraborate and a full wax layer as the substrate, while for the CuNPs-LIG sensor wax was printed in the same pretreated paper but with a specific wax design. The empty circles were designed to be filled with the copper sulfate solution, so when the laser passes, that area would correspond to the active area of the WE (Figure 4.10 A). Despite these circles being printed with a specific radius, when submitted to the heat of the hotplate to completely difuse the wax, it was observed that the circle area decreased. To correct this wax overspreading, the radius of circles was adjusted by excess.

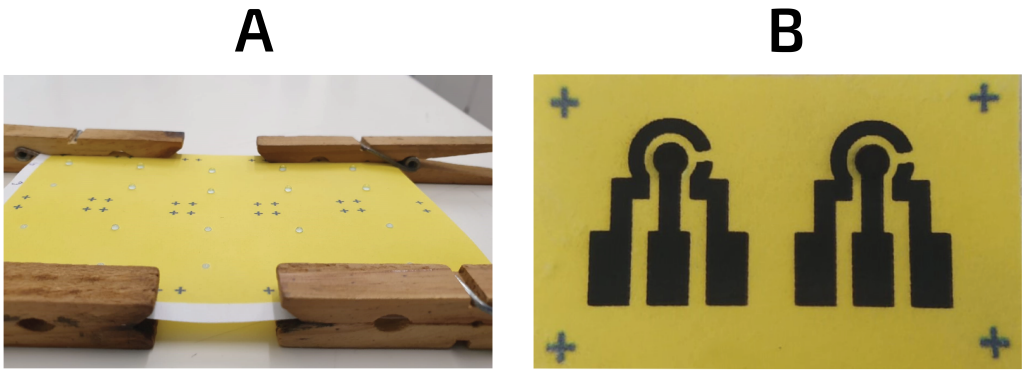

Figure 4.10: Substrate used in the fabrication of the CuNPs-LIG sensors. Substrate A) during the drying process of copper precursor and B) after the laser scanning. The crosses were designed to facilitate the alignment of the substrate with the laser beam.

All the developed sensors had these three-electrode architecture, shown in Figure 4.10 B), including a WE, RE and CE, projected on the Adobe Illustrator software. After laser engraving the selected pattern, plastic laminating sheets covered with adhesive tape were cut using the same laser. The mask pattern was designed for the working area of the electrode and the conductive tracks to be open. This mask allowed the creation of a passivation layer that protects the printed electrodes from impurities and rough handling, preventing their degradation. Moreover, it allows for a contained release of the supporting electrolyte when performing CV sets for the electrochemical characterization. Following this step, the electrodes were encapsulated using a commercial pouch laminator. By painting the cutted rectangles with silver conductive ink, which can be seen in

Figure 4.11, conductive tracks could be established. Also, to pattern the RE, the LIG area corresponding to this electrode was painted using Ag/AgCl ink.

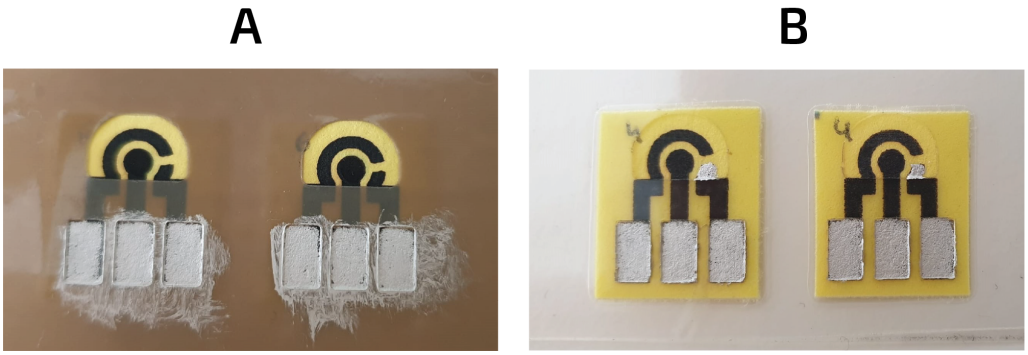

Figure 4.11: LIG sensors. Sensors A) before and B) after removing the adhesive tape.

The purpose of the adhesive tape, shown in Figure 4.11 A), was to facilitate the painting process of the RE and the conductive tracks with the corresponding inks without establishing contact with the electrodes between them. The electrodes were then put in a hot plate at 65 ºC for 1 hour to cure the paint, and then the adhesive tape was removed.

4.2.5 Electrochemical characterization

To perform the electrochemical characterization of both LIG and CuNPs-LIG electrodes, a potentiostat was used to execute CV experiments. Electrical contact was established by connecting the potentiostat electrical crocodile clips to the silver contacts of the electrode, as shown in Figure 4.12.

Figure 4.12: Connection established between the potentiostat and sensor. The cell cable connects to the WE, RE and CE on one end and the potentiostat cell cable connector on the other end.

A pretreatment was performed in all sensors during 5 cycles ranging from -2 and 2 V, with a scan rate of 150 mV s^{-1} and using the supporting electrolyte (0.1 mM KCl), since it has been reported before as a simple method to improve the electrochemical activity of the sensors [38]. After pretreatment, all electrochemical assays were performed using

5 M ferri/ferrocyanide, $[Fe(CN)_6]^{3-/4-}$ as the redox probe, prepared in the supporting electrolyte, at multiple scan rates of 10, 30, 50, 70, 90, 110, 120, 130 or 150 mV s^{-1}, for 6 cycles each. 60 μL of this mixture were pipetted to the electrode working area delimited by the plastic mask. For LIG based sensors, potentials were scanned from –0.3 to +0.7 V, while for the CV assays carried on CuNPs-LIG based sensors, this window was shortened to –0.2 to +0.6 V. Electrochemical Impedance Spectroscopy (EIS) was carried with a pulse of 10 mV in amplitude, 57 data points, over a frequency range from 100 000 to 0.1 Hz, using the same redox probe solution.

4.2.6 Glucose sensing performance

The nonenzymatic glucose sensing performance was evaluated using CV and chronoamperometry techniques. Figure 4.13 shows the experimental setup used for all glucose measurements. A retort stand and a three-claw clamp were used to hold the sensor, which was connected to the potentiostat through crocodile tips in each electrode.

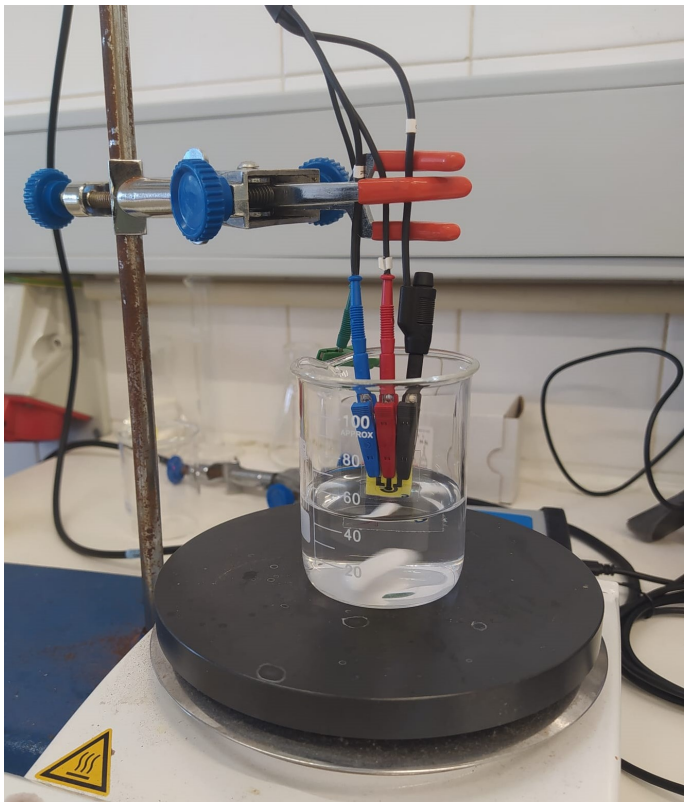

Figure 4.13: Experimental setup used to perform glucose sensor tests.

Solutions with different glucose concentrations were added to a 50 mL beaker containing 0.1 M NaOH as the supporting electrolyte, and a magnetic stirrer. The beaker was placed on a magnetic stir plate and all assays were performed at a stirring rate of 180 rpm.

For observing the transitions in copper oxidation states, CV sets were performed at a scan rate of 10 mV s^{-1} and potentials were scanned from -1 to +1 V. For both

discrete and continuous measurements, the chronoamperometric technique was selected to monitor the current increases with the addition of glucose. In discrete measurements, a specific glucose concentration was added to the beaker, and chronoamperometry was set to 150 s, leaving enough time for the current to stabilize. This process was repeated for different glucose amounts. In continuous measurements, successive glucose additions were consistently spaced by 50 seconds. Before adding a specific volume of the glucose solution, the same volume was extracted from the beaker. This procedure ensured that the content of the beaker would never reach the sensor's electrical contacts since its volume never exceeded 50 mL. Different applied potentials (0.4, 0.5, and 0.6 V) were tested to investigate which allowed a better electrochemical response and select the most suitable as the standard potential. The selectivity tests of these sensors were carried out using the same method as the continuous measurements. The influence of sodium chloride, ascorbic acid and uric acid was monitored.

5

Results and Discussion

In this chapter, the results obtained throughout this master thesis are presented and discussed in correlation with theoretical concepts. This chapter is divided into four sections: Section 5.1 presents the results of the LIG fabrication and optimization, mainly based on its electrical and electrochemical properties; Section 5.2 followed an identical methodology for the CuNPs-LIG fabrication and optimization with the complementary use of some nanoparticle characterization techniques; Section 5.3 analyzes the performance of the developed sensors towards glucose; finally Section 5.4 presents a prototype of a wearable and non-invasive system for glucose detection in sweat.

5.1 LIG Optimization

The study of Laser-Induced Graphene (LIG) started with the identification of laser parameters at different heights and the number of laser scans where there was a LIG formation. Sheet resistance tests were performed on these samples to analyze the most conductive graphene. Lastly, LIG was optimized to enhance its electrochemical properties by varying the laser parameters and the number of scans.

5.1.1 Laser power and speed study

As it was stated in Section 4.2.2.1, the first step of the work consisted of probing which laser conditions allowed for the LIG formation in the paper substrate. For this purpose, the matrices were constructed with all combinations of laser power and speeds, from 1 to 8 % of maximum operational values for each parameter. In this arrangement, the columns correspond to the laser scan speeds and the rows to the laser power.

Figure 5.1A) shows the obtained matrix, where LIG was produced at a z height of -0.1 in (corresponding to a distance from the focal plane of 0.79 mm), which was the z plane where the substrate was as close as possible to the laser source. It can be noticed that three different distinct regions are created. On the one hand, for S coordinate much lower than P, a damage threshold is surpassed and the laser provokes destruction of the substrate, with visible cracks. On the other hand, when the S coordinate is higher

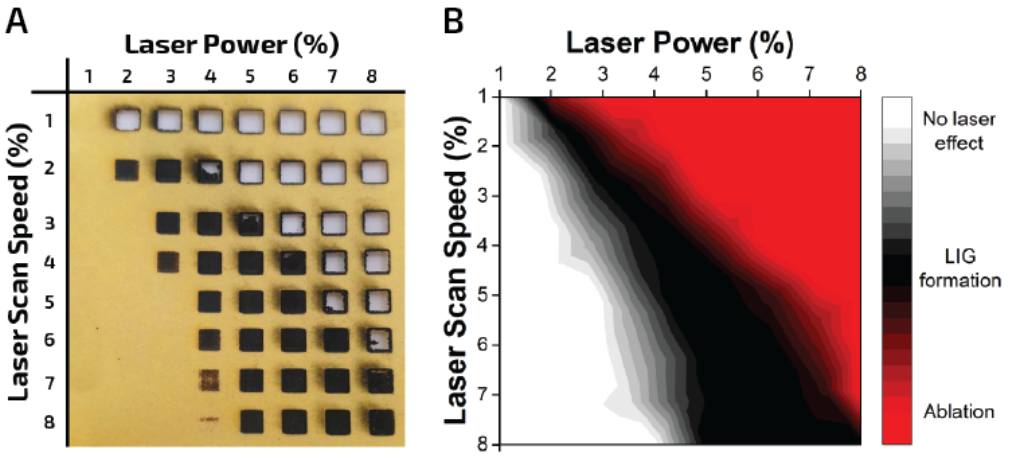

Figure 5.1: LIG parameter optimization at -0.1 in height. A) Matrices of laser operation parameters (P, power; S, scan speed) on paper substrate. B) Heatmaps of laser irradiation effect.

than *P*, or the laser has no effect on the paper substrate, or this effect is less notorious, producing a thin LIG only on the superficial paper fibers. This phenomenon happens because when the laser power is lower than the scan speed, the energy transferred to the paper substrate throughout the lasing process is not enough to break its C-O, C=O, and N-C bonds, leading to an incomplete graphitization. On the opposite side, when the laser scan speed is set with a lower value than the laser power, too much energy is applied to the substrate and instead of achieving a charred paper, the laser will provoke a complete or partial paper drilling.

The matrix results were transposed to a heating map (Figure 5.1 B) created with these three different regions, showing each parameters combination that allows the LIG synthesis. In this graph, white regions corresponded to a non-formation of LIG, the red regions represent the paper degradation, and the black regions represent the effective LIG formation. With a simple analysis, it is possible to conclude that there is a clear LIG formation for similar percentage values of laser power and scan speed and for slight variations of one parameter in relation to the other.

5.1.1.1 Morphological Characterization

Of all possible laser power and speed combinations that allowed LIG synthesis, three of them were chosen to perform a morphological study. Those three conditions were selected from the matrix diagonal, where the *S* coordinate equals *P*, to investigate the influence of an increase of these laser operation parameters on the substrate. Scanning Electronic Microscope (SEM) images of coordinates P2S2, P4S4 and P6S6 are presented in Figure 5.2.

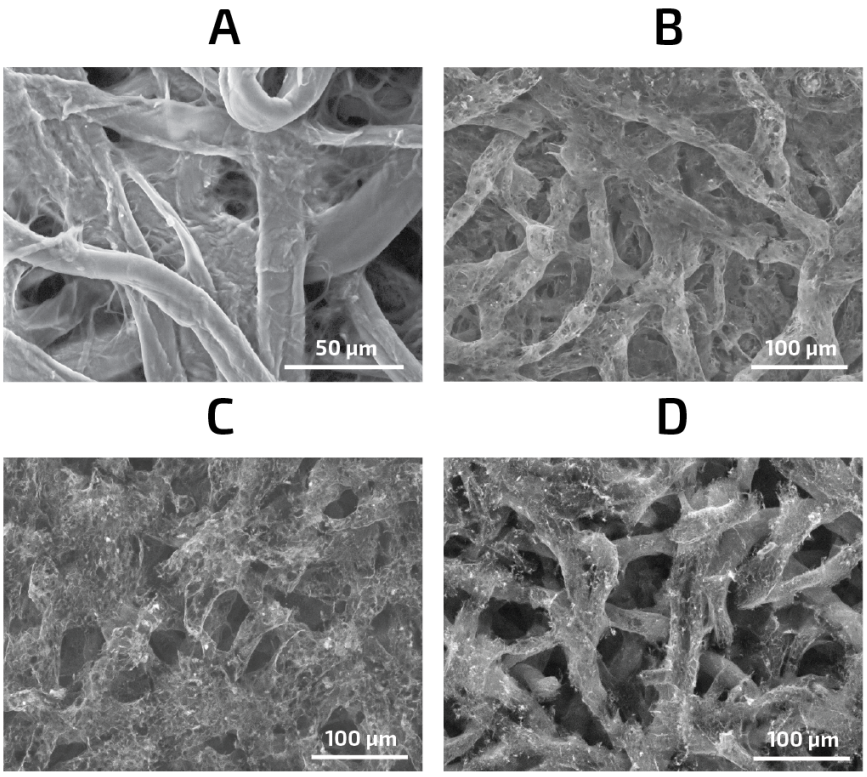

Figure 5.2: Morphological study of LIG. SEM images obtained for A) pre-treated Whatman paper and LIG on paper produced with B) P2S2, C) P4S4 and D) P6S6 laser parameters.

It is suggested that the higher the laser operation conditions that the substrate is submitted, the higher the cellulose fibers degradation and the higher the 3D network porosity will be. This high LIG porosity, related to a rapid liberation of gaseous products during the substrate thermal degradation, is a desirable characteristic in the sensor context since it will improve sensor surface area, which then will be reflected in an enhancement of the sensor's performance. On the other hand, for LIG electrodes with higher graphitization levels, structural integrity is not entirely preserved, which will compromise their electrochemical properties, so sensors will be most prone to leak sample solutions. With that said, a trade-off between low and high laser operation parameters is needed.

5.1.1.2 Chemical Characterization

Energy Dispersive X-Ray Spectroscopy (EDS) analysis

Chemical characterization started with the use of EDS technique, to study the influence of an increase of the laser power and speed parameters in the relative elemental composition of carbon and oxygen in LIG samples. Since the energy deposited in the paper substrate through the laser irradiation leads to a rupture of its chemical bonds, oxygen is released and there is a recombination of the carbon atoms to form graphene; so

it was expected an increase of the carbon content and a decrease in the oxygen portion upon laser irradiation of the chromatography paper. In Figure 5.3, an increase of the laser conditions from P2S2 to P4S4 revealed a reduction in oxygen content from 24.1 to 9.4 % and a rise in carbon content from 75.9 to 90.6 % is noticeable.

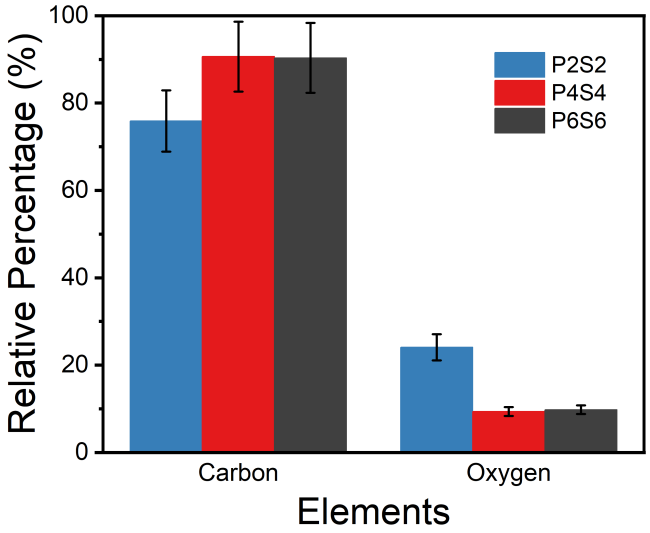

Figure 5.3: EDS analysis of LIG. Relative elemental composition of LIG produced on paper substrate for different laser operation parameters.

This leads to the conclusion that the graphitization process becomes more intense for higher power and speed coordinates, though the raising in carbon content and reduction of oxygen stabilizes when a certain threshold is reached, observed when comparing the EDS results for P4S4 and P6S6 parameters. These findings are aligned with previous work done by Lin et al. [61], where it is proved that carbon content reaches a maximum value and further increase of the laser parameters results in a slight decrease of carbon relative abundance paired with an increase of the same percentage of oxygen.

Raman analysis

To complement the EDS analysis, an evaluation of the LIG quality was carried out using Raman spectroscopy. The Raman spectrum obtained for a LIG sample produced with the optimal condition for the glucose sensor, P4S4, is presented in Figure 5.4.

Three main peaks were identified, the conventionally D, G, and 2D bands at 1346, 1586 and 2691 cm^{-1} respectively, reported in the literature as characteristic peaks of graphitic structures [61]. The D band is associated with the disorder in graphene layers, while the G (responsible for the stretching vibrations in all sp^2 carbons) and 2D (characteristic of all sp^2 carbon) bands reflect the presence of graphene and graphite; a prominent 2D peak is usually suggestive of high-quality graphene [70]. Two ratios are usually used to characterize the produced graphene: the I_D/I_G is used to determine the

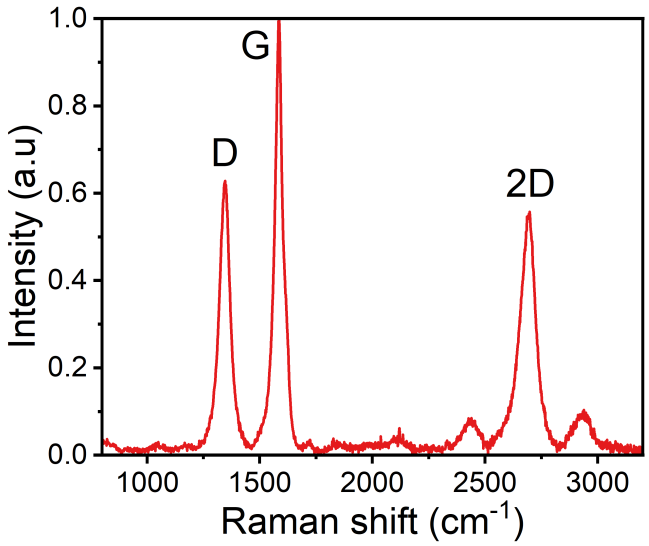

Figure 5.4: Raman analysis of LIG. Raman spectrum of LIG produced using P4S4 as the laser parameters.

quality of graphitization or the defective disorders on LIG and the I_{2D}/I_G gives information about the nature of graphene layers. Considering that $I_{2D}/I_G > 2$ is a typical feature of monolayer graphene, the obtained I_{2D}/I_G ratio of 0.58 suggests that the fabricated LIG presents a multilayer structure. To what concerns the I_D/I_G ratio, and taking into consideration that a high quality graphene presents a value for this ratio closest to 0, the obtained value of 0.63 indicates that during the laser induction, highly defective carbon-based structures are being formed. Although these results do not reflect pristine graphene, the ultimate application of LIG is the fabrication of a glucose sensor, so the key factor is that the electrodes reflect a good response to glucose.

X-Ray Photoelectron Spectroscopy (XPS) analysis

XPS measurements were performed to characterize the surface chemical composition of LIG, produced with the same P4S4 laser parameters as the Raman sample. Figure 5.5 A) shows the survey scans, which indicate the presence of carbon, oxygen and sodium in the sample. The exhistance of sodium is related to the paper pretreatment with fire-retardant. The high-resolution spectrum of C1 s shown in Figure 5.5 B) revealed the presence of six different carbon bonds were found at the following binding energies: C=C (sp^2) at 284.3 eV, C–C (sp^3) at 285.5 eV, C–O at 286.6 eV, C=O at 287.5 eV, O=C–O at 288.6 eV, and π–π^* satellite at 290.7 eV. Literature reports the C–O peak as the dominant one in the C 1s XPS spectrum for a paper substrate [123], while the results from the analysed LIG sample revealed that the fabricated material is dominated by sp^2 carbon atoms. This analysis confirms that during the laser scan, a graphitization occured from the paper substrate into a network of sp^2-hybridized carbon atoms, i.e. LIG.

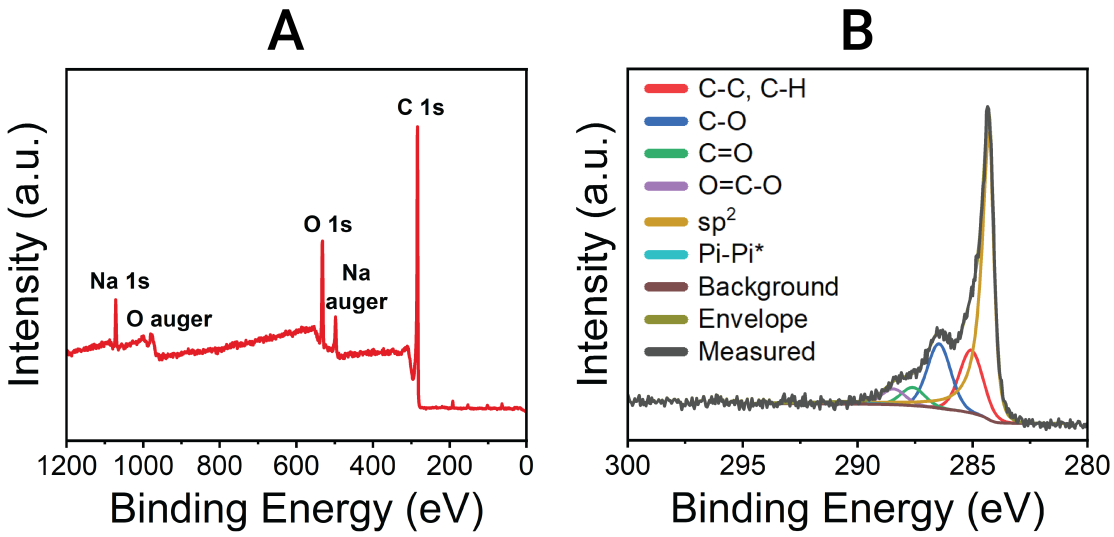

Figure 5.5: XPS analysis of LIG. A) Survey XPS spectrum of LIG. B) High-resolution XPS spectrum of C1s peaks.

5.1.2 Laser power, speed and height study

With the aim of investigating the influence of the height of the laser moving platform in LIG quality, the initial process of creating a matrix varying laser power and speed parameters was then repeated three times for the following heights z=-0.05 in, z=0 in and z=+0.05 in, which corresponded to a distance from the focal plane of 0.48, 1.75 and 3.02 mm, respectively. Figure 5.6 shows the location of the different plans used for LIG synthesis in relation to the focal plane, with the respective spot sizes, designed in proportion to the actual distance.

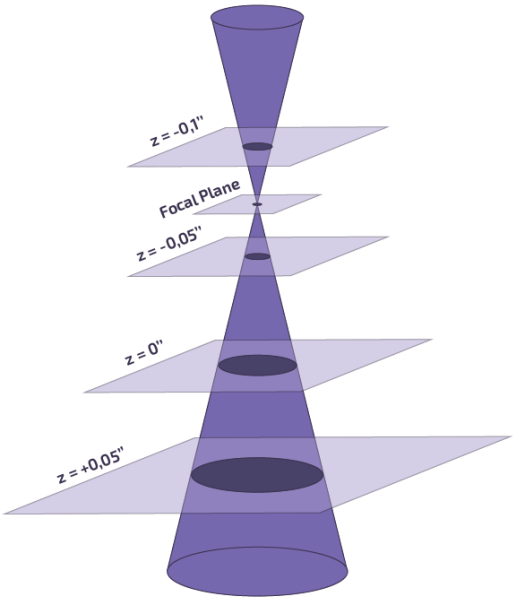

Figure 5.6: Representation of the different plan heights with the respective spot sizes.

Along with the optimization matrices, heatmaps were constructed for each z height (Figure 5.7). The results of this z height variation reveal that as the platform goes down, the black area in the heatmaps that represents LIG formation decreases. Thus, less possible power and speed combinations allow the LIG synthesis on paper substrate.

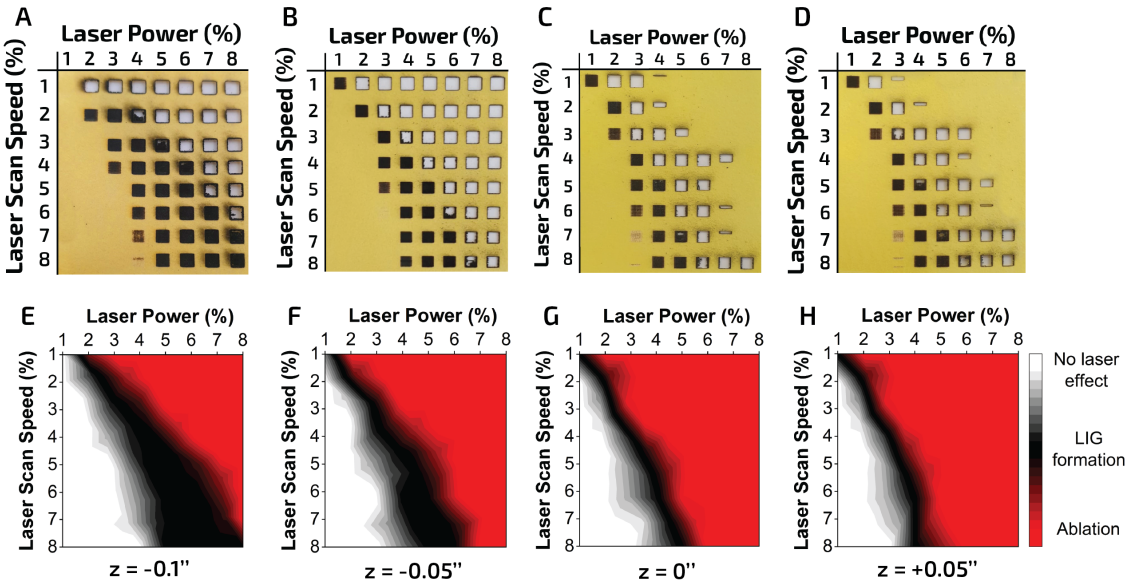

Figure 5.7: LIG parameter optimization for different heights. Matrices of laser operation parameters (P, power; S, scan speed) on paper substrate at A) z=-0.1 in, B) z=-0.05 in, C) z=0 in and D) z=+0.05 in. Heatmaps of laser irradiation effect at E) z=-0.1 in, F) z=-0.05 in, G) z=0 in and H) z=+0.05 in.

Furthermore, the results show that for lower heights, the LIG formation region starts

to shift to the left on the graph; this means that LIG is being formed for S coordinates slightly higher than P coordinates and stops being so concentrated on similar values of laser power and speed.

5.1.2.1 Electrical Characterization

After optimizing the laser parameters for the LIG formation, sheet resistance tests were performed with the four-point probe equipment for four samples of the same laser power, speed and height combination. Since the basic function of an electrode is to conduct current, the lower its sheet resistance, the higher the material electrical conductivity, which will result in a faster and more efficient sensor. A table with all sheet resistance measurements (Table I.1) is presented in annex I. The sheet resistance values that are not presented in the table is either because those laser power and speed combinations do not allowed for LIG synthesis without drilling the substrate, or even though there was a LIG formation, the equipment was not able to measure their sheet resistance, probably due to its high value. Through the table analysis, it was verified that with the decrease of the laser platform level, sheet resistance values tend to increase. This means that the most conductive LIG was obtained for the laser platform at z=-0.1 in height, surpassing all sheet resistance values of the remaining heights. Attending to the distance of the different planes from the focal plane, it can be said that sheet resistance values show the same tendency demonstrated by Chyan et al. [62] for LIG samples in poly(ether imide). It was proven that by defocusing the laser, significant improvements in the respective sheet resistance values were registered until a certain distance from the focus; when the induced defocus surpasses this limit, electrical LIG properties tend to get worse. This effect can be seen when analyzing the order of magnitude of sheet resistance values for all heights. While most of the values measured for z=-0.1 in height have 1 order of magnitude, for z=-0.05 in this order is increased to 2 and for z=0 in and z=-0.05 in planes, it was raised to the 4^{th} power. This means that increasing the defocus level from 0.48 mm to 0.79 mm causes a great improvement in LIG electrical properties; yet, major increases in defocus, namely to 1.75mm and 3.02mm, resulted in higher sheet resistance values, or in other words, in a less conductive material. To correlate this data with the study mentioned above, it is assumed that raising or lowering the z-platform from the focal plane to achieve a specific defocus creates the same effect on LIG electrical values. This assumption is made by the fact that the laser beam must irradiate the same conical shape for the part above and below the focal point, and so height variations of the same amplitude should produce LIG with identical properties. In order to prove this hypothesis, a more detailed study would be needed since no research on this subject has to date been published. With this study, it was concluded that the LIG with the best electrical properties was fabricated for the operating condition where the z-axis distance between the substrate and the laser tip is minimum, z=-0.1 in. With that said, this was selected as the optimal height to synthesize LIG.

For further study on the influence of the laser parameters for this optimized height on the fabricated LIG, Figure 5.8 shows a sheet resistance heatmap as a function of laser power and speed. It can be noticed that the same tendency applies to all measurements:

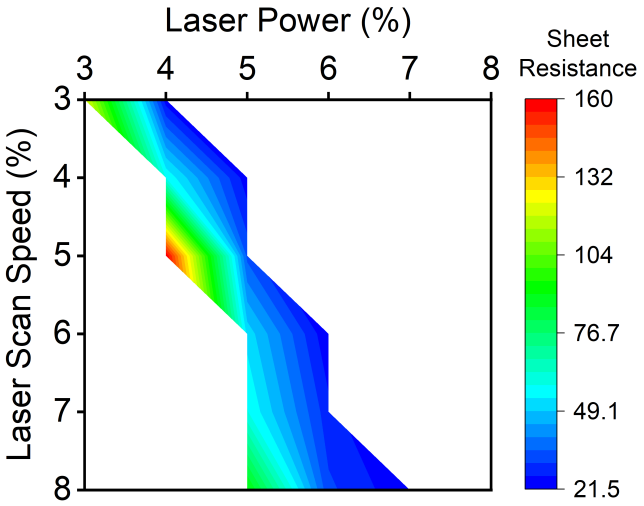

Figure 5.8: Sheet resistance heatmap as a function of the laser power and speed parameters.

fixing a laser power percentage, the lowest sheet resistance can be found for speed coordinates increasingly smaller. From another perspective, setting a certain laser scan speed and analyzing data from the lowest to higher power percentages, it can be said that warmer colors associated with higher sheet resistance measures start to shift to colder colors. This means that for higher power coordinates, LIG is fabricated with better electrical conductivity properties. Despite these results suggesting the choice of the higher laser power percentage for a certain scan speed, these combinations of laser parameters are associated with a more intense substrate degradation. Since the final application of the LIG is a wearable sensor that should be resistant to handling, the sensor quality must not be compromised by an over-optimization that pushes the sensor integrity to the limit.

5.1.3 Number of laser scans study

Additionally, the influence of number of laser scans on LIG was investigated. This variation was based on the premise that multiple exposures that should increase the substrate carbonization degree will ultimately result in an improvement in LIG conductive properties. For this purpose, matrices with the same power and speed range were created with two and three laser scans and the results were transposed to the respective heatmaps.

Comparing all three situations shown in Figure 5.9, it can be said that the differences between them are minor and that a variation in the number of laser scans has almost no impact on the combinations of laser power and scan speed that allow LIG synthesis. Nevertheless, as the number of scans increases, the area colored in black gets slightly smaller, which means that the more laser scans the substrate is submitted, the greater the

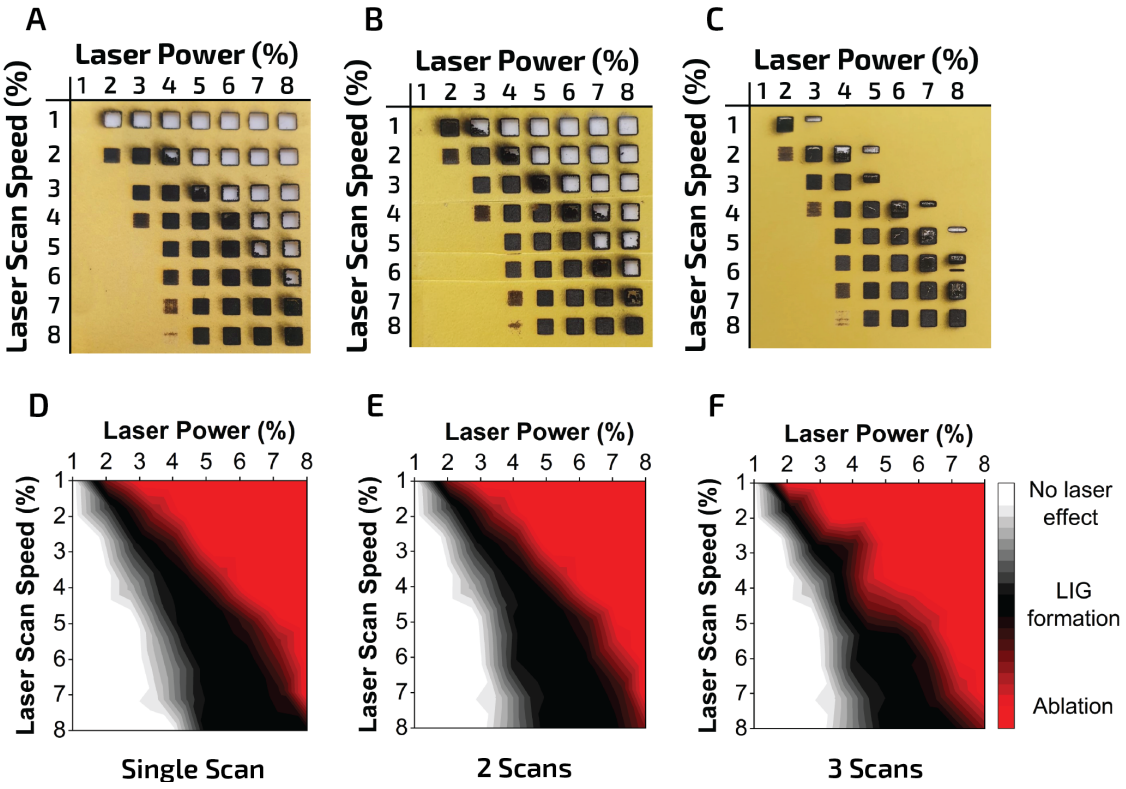

Figure 5.9: LIG parameter optimization for different number of laser scans. Matrices of laser operation parameters (P, power; S, scan speed) on paper substrate with A) one, B) two and C) three laser scans. Heatmaps of laser irradiation effect with D) one, E) two and F) three laser scans.

paper degradation will be. These results are expected simply because more laser exposure will result in further graphitization.

5.1.3.1 Electrical Characterization

The electrical characterization results obtained for LIG samples produced with one, two, and three laser scans are presented in Figure 5.10.

Although no significant difference was noted for LIG produced with a different number of laser scans, sheet resistance values reflect variations in the electrical properties for these samples. Firstly, it can be seen that with the increase in the number of laser scans, the window of LIG samples that can be measured is shortened, and fewer laser operation conditions can generate LIG suitable for electrode production. Secondly, and more importantly, lower sheet resistance values can be achieved by increasing the number of laser scans. These results follow the upper mentioned premise: multiple laser scans result in greater conversion of cellulose fibers in graphitic material, therefore producing a more conductive material. With a single pass, the P6S6 and P7S8 conditions stand out with their low sheet resistance value of 21.9 Ω sq^{-1}. The lowest sheet resistance value was 14.8 Ω sq^{-1}, obtained for P7S8 laser parameters with a double laser pass.

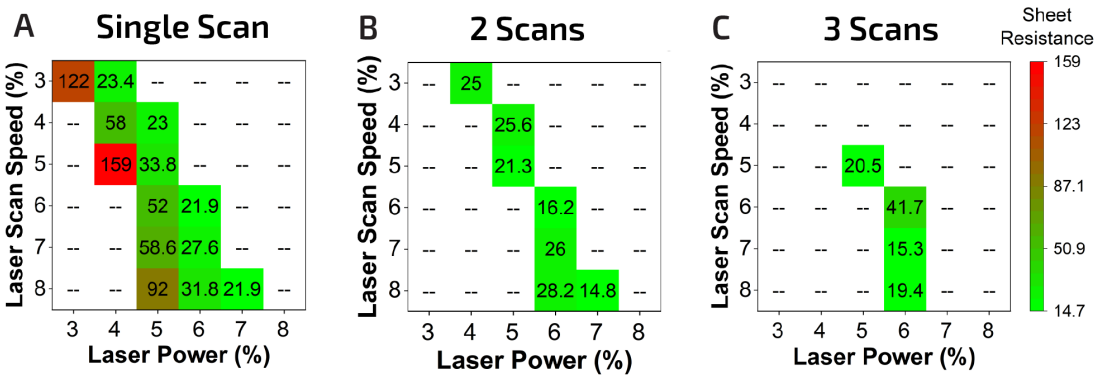

Figure 5.10: Electrical characterization of LIG. Sheet resistance matrices as a function of power and speed parameters for A) one, B) two and C) three laser scans.

Table 5.1 shows a comparison between the sheet resistance values obtained in this work and other published articles for LIG produced in paper substrate. These values indicate that the optimized LIG in terms of electrical performance presents a lower sheet resistance value when compared with other reports. Thus, the fact that the fabricated LIG exhibited excellent conductivity leads to the belief that a sensor made of this material will have a good electrochemical performance.

Table 5.1: Comparison of sheet resistance values obtained for LIG produced in Chromatography paper.

Ref.	[128]	[129]	[123]	This work
Sheet Resistance (Ω sq^{-1})	56	61.5	32	14.8

5.1.4 Electrochemical Characterization

After all the fabrication steps, the electrochemical behavior of the LIG based sensors was evaluated through Cyclic Voltammetry (CV). This technique allowed the extraction of important kinetic parameters that reflect the electrochemical sensor performance.

5.1.4.1 Sensor architecture study

Firstly, a simple electrode architecture study was performed to improve the electrochemical sensor performance. For all sensors fabricated with the purpose of this section, the architecture study, the laser parameters used for the LIG synthesis were P7S8. Taking as the starting point the generic sensor design used in several published articles [37, 38, 107], the first modification was testing two different electrode dimensions for the same architecture. The insets of Figure 5.11 show the difference between those two layouts, being version 1 the oversized format and version 2 the miniaturized sensor. For these two design possibilities, it was not possible to establish a comparison based on their electrochemical active surface area (A_e) and heterogeneous electron transfer rate (k^0) intrinsic

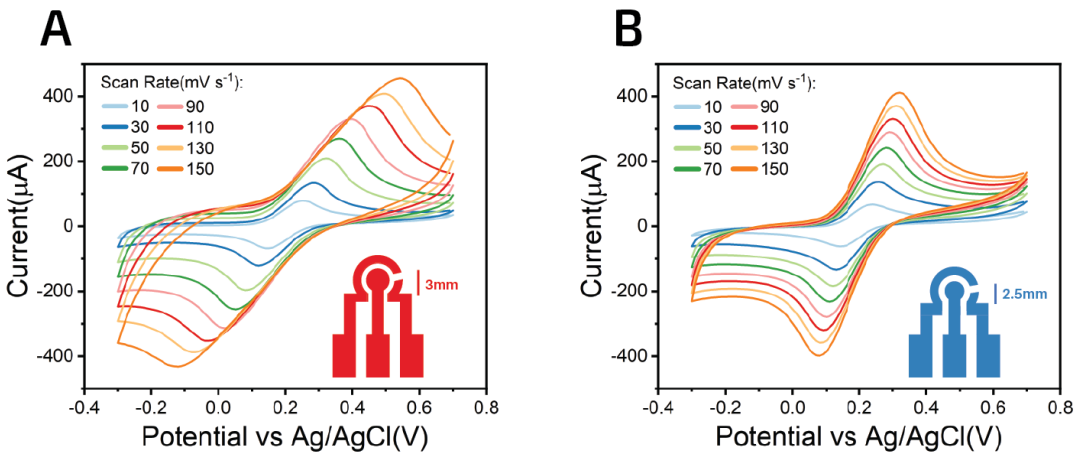

Figure 5.11: Electrochemical characterization of the oversized and miniaturized sensor designs. Cyclic voltammograms obtained for the scan rate range of 10 to 150 mV s^{-1} using 5×10^{-3} M $Fe(CN)_6{}^{3-/4-}$ as redox probe for the versions A) 1 and B) 2 of sensor architectures. The insets of the graphs represent the electrode design versions used.

parameters since the first version did not fulfill the requirements to apply the equations mentioned in Section 2.2.1.2, namely due to its high peak separation. Nonetheless, by simply analyzing Figure 5.11, it is possible to conclude that the second design version represents a sensor with better electrochemical performance compared to the first version. As the scan rate increased, version 1 showed a much greater increase in the distance between the cathodic and anodic peaks, as seen in the voltammograms for the highest scan rate values. This high peak separation reflects slow electron transfer at the electrode surface, which is not an ideal indicator for a good sensor. One possible explanation is that the effect of ohmic drop on the oversized sensor is more impactful. As stated in Section 2.2.1.2, a greater distance separating the Working Electrode (WE) and the Reference Electrode (RE) can be reflected on the voltammogram through an increase in the peak separation. With that said, since in the miniaturized version, the WE and RE are closer, the ohmic drop contribution will be much smaller.

To complement this study, Electrochemical Impedance Spectroscopy (EIS) was used to collect information about electron transfers between the electrolytes and the electrode surface. The obtained data was analyzed by fitting Nyquist plots (presents the negative of the imaginary part as a function of the real part) with Randles modified circuit, an equivalent electrical circuit model of the sensor. This fitting makes it possible to extract parameters such as the electron transfer resistance (R_{CT}) and solution resistance (R_S). Figure 5.12 shows the obtained Nyquist plots, where the symbols represent the measured data, and the black lines indicate the fit to the equivalent Randles modified circuit. It can be said that the R_S parameter, related to the geometry and electrode area [130], presents significantly lower fitted values for the miniaturized sensor (115 Ω) compared with the oversized version (144 Ω). Regarding the R_{CT} values, the same tendency is observed; the

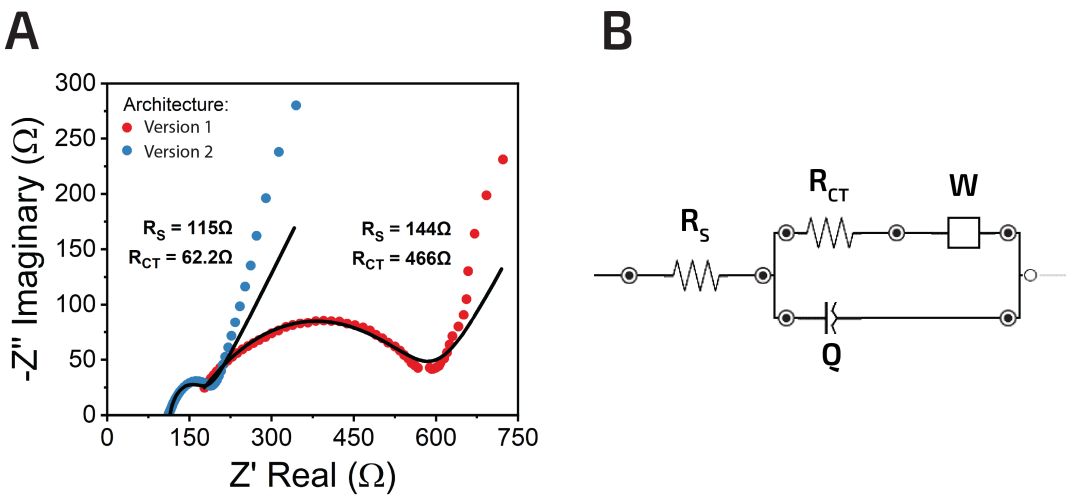

Figure 5.12: Impedance spectroscopy study for different sensor geometries. A) Nyquist plots of EIS and B) the equivalent Randles modified circuit. The symbols represent the measured data while the black lines indicate the fit to the equivalent circuit.

oversized sensor revealed a R_{CT} of 466 Ω, decreasing for 62.2 Ω for the miniaturized sensor. The R_{CT} parameter can be retrieved from the semicircle diameter of the Nyquist plot and reflects the electron transfer process and electrode conductivity [108]. With that said, the values of both parameters are in accordance with the ones obtained for CV measurements. Based on the previous results, the miniaturized sensor version was selected to pursue the following tests. Beyond the better electrochemical performance, this electrode architecture allows for a less time-consuming fabrication process, since the input design to be printed has smaller dimensions.

Another architecture variation was made regarding the shape of the electrodes, consequently influencing their size. Since the rounded version corresponds to the miniaturized design presented above, Figure 5.13 shows the electrochemical response of the squared sensor and a comparison between the two designs. Through the analysis of the voltammograms (Figures 5.11 B and 5.13 A), it can be concluded that these electrodes can be categorized as quasi-reversible systems since peak separation increases when the scan rate follows the same trend.

It was possible to withdraw the A_e value by plotting the square root of scan rate as a function of the peak current and then relating the obtained with the Equation 2.4 (Figure 5.14 A). Since the peak currents are linearly proportional to the square root of scan rate (R^2 = 0.9944 for anodic and 0.9936 for cathodic peaks), this reaction is a diffusion-controlled process, which allows the application of the Equation 2.5 developed by Nicholson. For the calculation of the α constant, the slopes of the linear portion of the calibration curves for anodic and cathodic peak currents vs. log scan rate were deduced (Figure 5.14 B), which reunited all the parameter values for then apply the Equation 2.6.

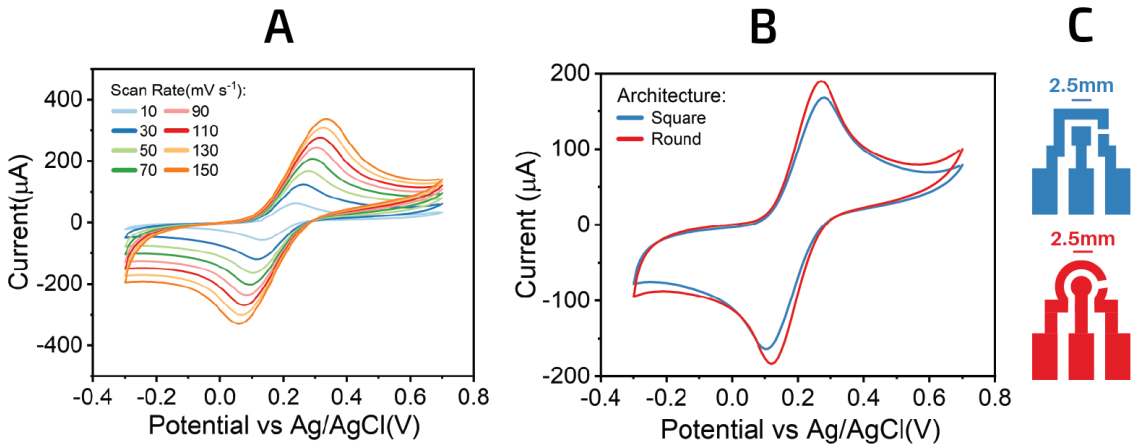

Figure 5.13: Electrochemical characterization of the squared and rounded sensor designs. A) Cyclic voltammograms of the squared electrode design, obtained for a scan rate range of 10 to 150 mV s^{-1}. B) Plot of the obtained voltammograms of both sensor architectures for a scan rate of 50 mV s^{-1}. C) Squared and rounded electrode designs. CVs were recorded using 5×10^{-3} M $Fe(CN)_6{}^{3-/4-}$ as redox probe.

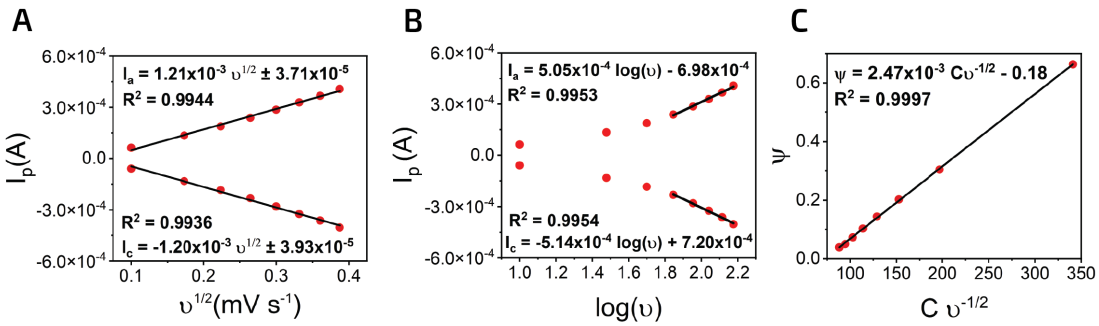

Figure 5.14: Auxiliary plots for the determination of A_e and k^0 parameters for the round version. A) Plot of peak currents vs square root of corresponding scan rate. B) Plot of anodic and cathodic peak currents vs logarithm of scan rate. C) Plot of the kinetic parameter Ψ vs $C\,v^{-1/2}$.

Once the α coefficient was known, the dimensionless kinetic parameter Ψ was calculated through Equation 2.8. Finally, plotting the graph that results from the simplification of the Nicholson Equation 2.5,

$$\Psi = Ck_0 v^{-\frac{1}{2}} \tag{5.1}$$

, where $C = \left(\frac{D_O}{D_R}\right)^{\frac{\alpha}{2}} \sqrt{\frac{RT}{\pi n F D_O}}$, it was possible to extract the k^0 value.

Table 5.2 gathers the kinetic parameters information for the squared and rounded electrodes, where the A_g parameter corresponds to the geometric area of the WE. First, it can be said that for both sensor designs, the A_e is greatly enlarged when compared to the A_g. Nevertheless, for the rounded version A_e was increased by 4.1 times, while for the

squared sensor, A_e was only 3.2 times that of WE geometric area. For the k^0 parameter, the same trend is observed. Since both A_e and k^0 parameters present improved values for the rounded version of the electrodes, this design was selected as the optimized sensor architecture for the following analysis.

Table 5.2: A_e and k^0 parameters as a function of different sensor architectures.

Kinetic Parameters	$A_e(\text{mm}^2)$	$k0(10^{-2}\ \text{mm s}^{-1})$	A_e/A_g
Rounded design	20	2	4.1
Squared design	16	1.8	3.2

It is noteworthy that for all the following calculated A_e and k^0 values of sensor variations in this section, the same upper mentioned calculation methodology was used.

5.1.4.2 Laser parameters study

The subsequent study was performed to evaluate the influence of different laser parameters for the LIG formation in the electrochemical behavior of the sensors. Due to the high number of laser parameter combinations and thus to reduce the number of samples to be tested, only the ones that presented the lower sheet resistance values were selected to fabricate the sensors and perform an electrochemical analysis. Figure 5.15 highlights the difference between the voltammograms obtained for a scan rate of 50 mV s^{-1} for all laser parameters combinations considered.

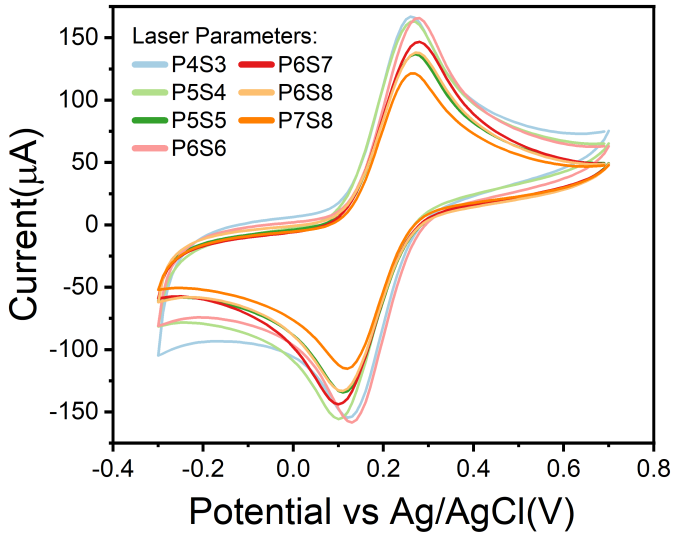

Figure 5.15: Voltammograms obtained for LIG-based sensors fabricated at different laser parameters. CV experiments were performed at a scan rate of 50 mV s^{-1} using 5×10^{-3} M $Fe(CN)_6^{3-/4-}$ as redox probe.

It can be noted that there is a slight variation for the different laser parameters in the position of the cathodic and anodic peaks, as well as in their intensity. These disparities

are reflected in the values of the A_e and k^0 parameters, summarized in Table 5.3.

Table 5.3: A_e and k^0 parameters of LIG sensors produced at different laser power and speed conditions.

Laser Parameters	**P4S3**	**P5S4**	**P5S5**	**P6S6**	**P6S7**	**P6S8**	**P7S8**
$A_e(mm^2)$	29	21	26	28	22	22	20
$k0(10^{-2}$ mm $s^{-1})$	1.9	1.7	2	2.6	2.1	1.9	2

Since the geometric area of the WE in this electrode configuration is approximately 4 mm^2, by analyzing the table it can be concluded that in all laser parameter combinations the A_e parameter increased. LIG sensors fabricated with the laser parameters P4S3 and P6S6 stand out for their high specific catalytic activity, showing A_e values of 29 mm^2 and 28 mm^2 respectively. Regarding the transfer kinetics, the P6S6 condition emerges as the laser parameter combination that allows the LIG fabrication with the best charge transfer properties, reaching a k^0 value of 2.6×10^{-2} mm s^{-1}.

To continue the study of multiple scans, an electrochemical study was performed on sensors fabricated with the same laser operation conditions, but with two laser scans. Figure 5.16 presents the results of the CV experiments for a scan rate of 50 mV s^{-1}.

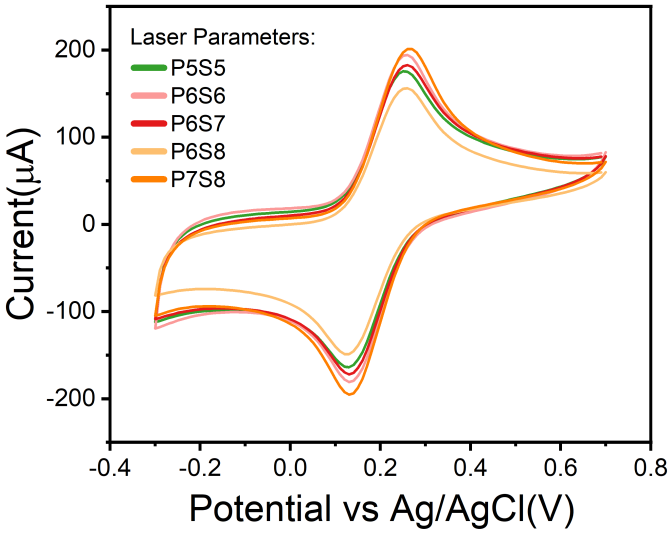

Figure 5.16: Voltammograms obtained for LIG-based sensors fabricated at different laser parameters with two laser scans. CV experiments were performed at a scan rate of 50 mV using 5×10^{-3} M $Fe(CN)_6{}^{3-/4-}$ as redox probe.

The combinations of laser parameters that do not appear in the graph experienced solution leakages, making it impossible to use those conditions to produce feasible sensors. Compared to the previous results, these voltammograms point out a greater current intensity of the peaks, almost reaching 200 mV, as well as a smaller peak separation,

which suggests an enhanced electrochemical performance. Table 5.4 presents the values of A_e and k^0 related to each laser condition.

Table 5.4: A_e and k^0 parameters of LIG sensors produced at different laser power and speed conditions, for two laser scans.

Laser Parameters	**P5S5**	**P6S6**	**P6S7**	**P6S8**	**P7S8**
$A_e(\mathrm{mm}^2)$	23	29	27	28	33
$k0(10^{-2}\ \mathrm{mm\ s}^{-1})$	2.3	2.9	2.7	2.5	3.3

To highlight the differences in A_e and k^0 values, comparative graphs of these parameters were made for LIG sensors produced with one and two laser scans (Figure 5.17).

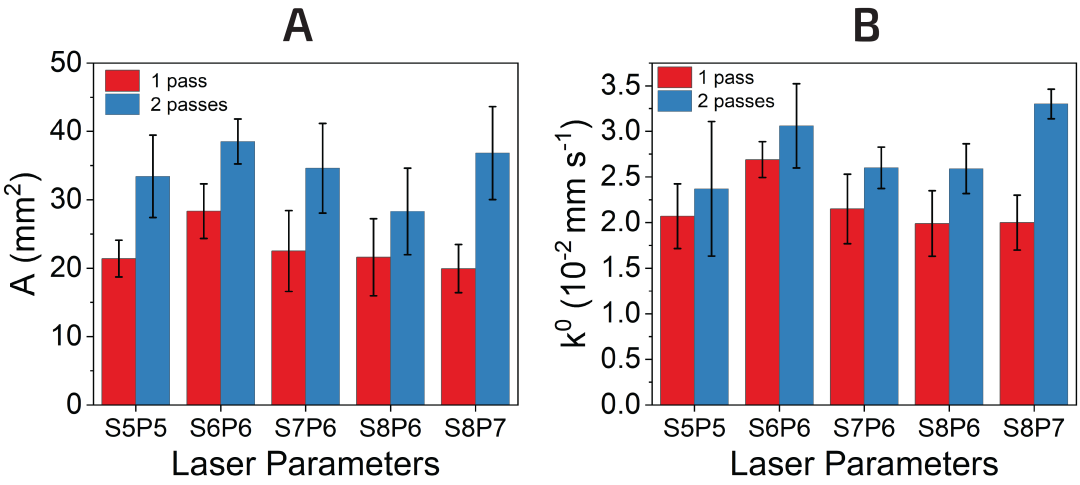

Figure 5.17: Comparison of kinetic parameters for one and two laser scans. Plots of A) A_e and B) k^0 as a funtion of laser parameters, for one and two laser scans.

By analyzing the graphs, it can be seen that there is an increase in all combinations of laser power and speed for both A_e and k^0 values. As verified by sheet resistance tests and proven with this electrochemical characterization, the number of laser scans seems to have an influence on the LIG properties. These results confirm that with multiple lasing, there is an improvement in the quality of graphene, which can be clearly seen by the increase of A_e and k^0 kinetic parameters. However, this improvement does not rise linearly with the increase of one laser scan for all laser parameter combinations, as verified for the large improvement in both electrochemical parameters for the P7S8 condition. Moreover, it is interesting to note that the results of the electrical and electrochemical characterizations coincide; both measurements indicate the selection of P6S6 parameters for one laser pass and the P7S8 condition for two laser scans, which both present the best results within the tested laser power and speed combinations.

5.2 CuNPs-LIG Optimization

The study of copper nanoparticles (CuNPs) and LIG synthesized through laser induction started with a simple optimization of the copper precursor. Then, a study to identify the laser parameters that do not lead to the destruction of the substrate was performed. Several techniques were used to characterize the CuNPs. The electrochemical performance was evaluated on sensors produced with the laser parameters that led to the lower sheet resistance.

5.2.1 Copper precursor optimization

Regarding the fabrication of CuNPs-LIG composites, a study of the precursor volume and concentration was performed. Figure 5.18 shows the obtained results, where each row in this matrix corresponds to a different concentration, and the columns represent a volume variation.

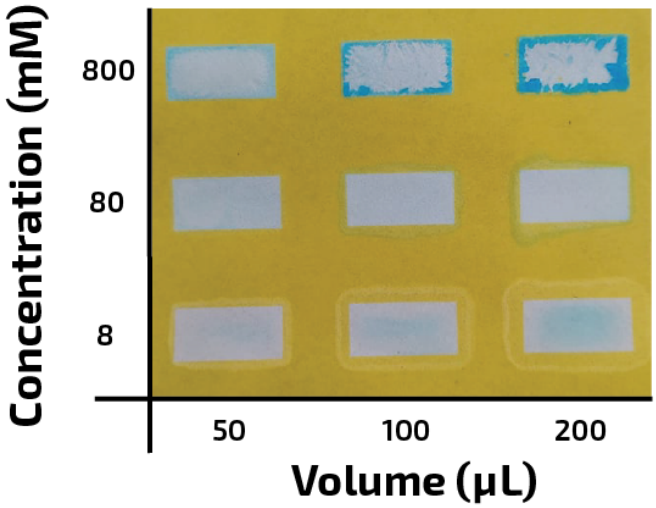

Figure 5.18: Copper sulfate solution in paper substrate. Photograph of samples prepared with different copper precursor volumes and concentrations.

Based on a visual analysis of the samples, precursor concentrations of 800 mM and 8 mM were discarded since when dried, they resulted in a crystal formation and a non-uniform distribution of the copper sulfate solution, respectively.

5.2.1.1 Morphological Characterization

Figure 5.19 shows the images obtained from SEM measurements of paper substrate after the copper precursor solution was dried. Figure 5.19 A shows an homogeneous distribution of the copper sulfate crystals on the cellulose fibers surface, and in the magnified version (Figure 5.19 B), it is possible to observe their flower-like structures.

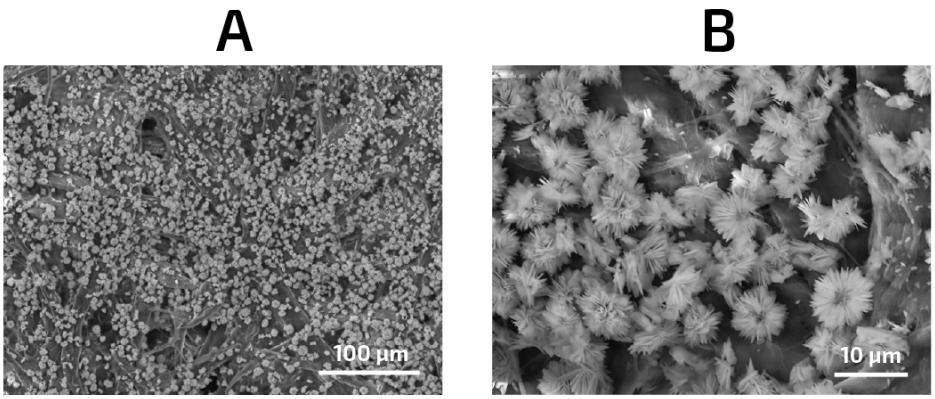

Figure 5.19: Morphological study of copper sulfate solution in paper substrate. A) SEM image obtained for 1 μL mm^{-2} volume to surface area ratio (VA ratio) of copper precursor and B) shows a magnified version.

5.2.1.2 Chemical Characterization

EDS was used to identify and quantify the chemical elements present in the paper sample containing the drop-casted copper sulfate solution. The main objective of this analysis was to later compare the atomic percentages of each element, before and after the submission of the sample do the laser. Figure 5.20 shows the region in which this EDS analysis was carried out, with the respective mappings of each element. It can be said that the contribution of the carbon element comes from the Whatman paper, copper and sulfur derive from the copper precursor, and oxygen results from both materials. By analyzing the relative percentages of copper and sulfur (10.7 and 4.7 %, respectively) and only considering these two elements, it is possible to state that the relation between these two is approximately 7:3.

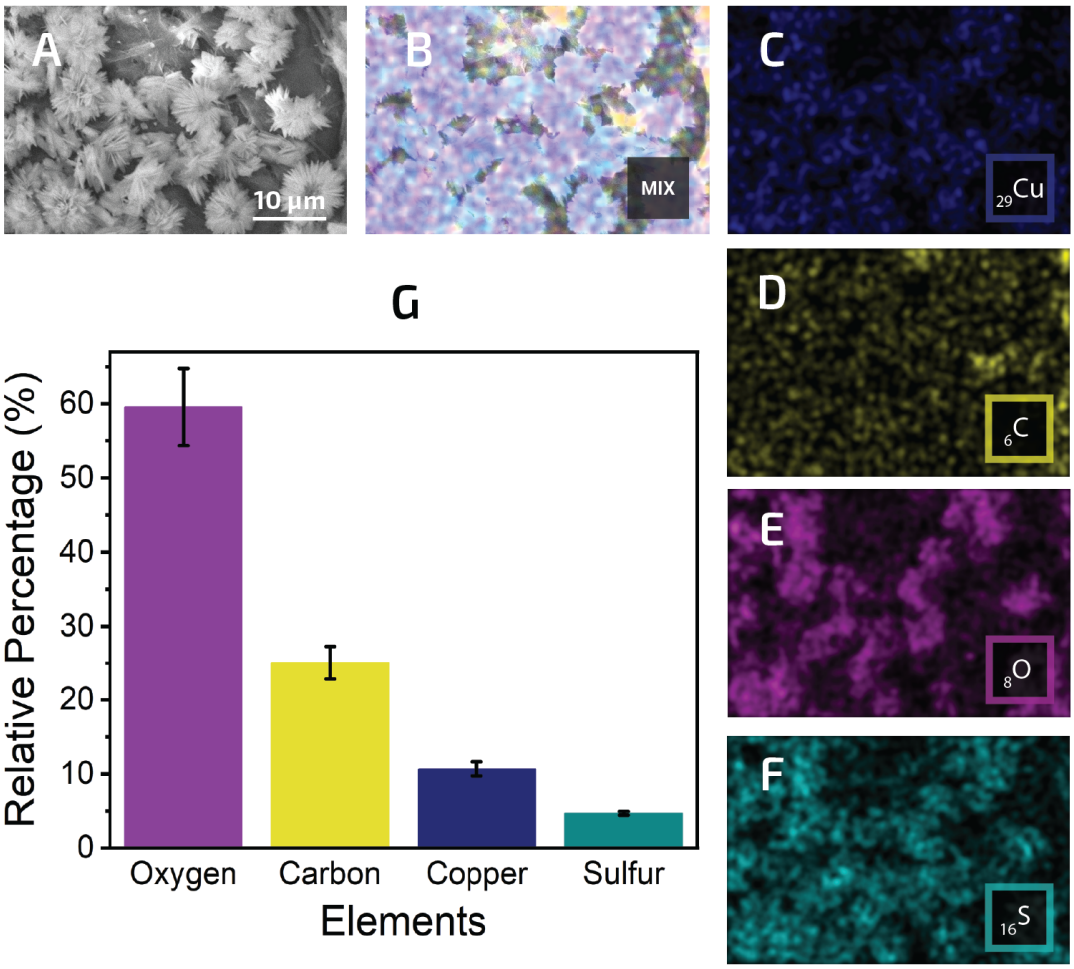

Figure 5.20: Chemical study of copper sulfate solution in paper substrate. A) SEM image obtained for 1 μL mm^{-2} VA ratio of copper precursor and B) shows a magnified version.

5.2.2 CuNPs-LIG optimization

After selecting the precursor concentration to be used in the following steps, samples with different volumes of the copper sulfate solution were submitted to laser irradiation. Similar to the LIG optimization described in the previous section, several combinations of laser power and scan speed were tested in order to identify those that produced LIG without damaging the substrate. For this purpose, all laser parameter combinations that resulted in LIG formation were tested in this modified paper substrate. Figure 5.21 shows the resultant matrix, where each line corresponds to a particular VA ratio of the copper precursor.

Firstly, comparing these results with the ones obtained for the LIG optimization, it can be said that with the addition of copper precursor solution to paper, the substrate becomes weaker and more prone to degradation. One possible explanation is that the places intended for the copper precursor deposition were not previously submitted to wax treatment (because of its hydrophobic character), being this way less resistant to the

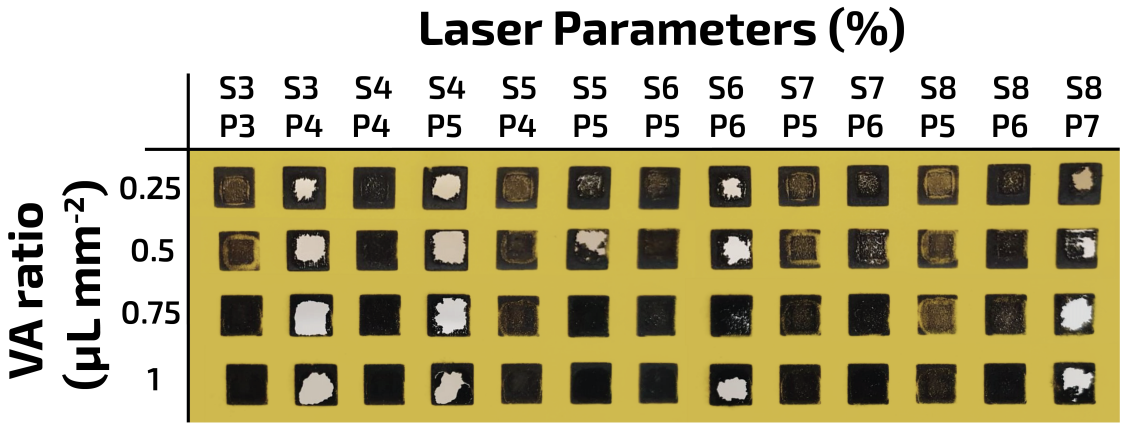

Figure 5.21: Laser parameters optimization for the fabrication of CuNPs-LIG composites. Matrix of laser operation parameters (P, power; S, scan speed) as a function of the copper precursor VA ratio.

laser beam. Therefore, combinations of power and speed that in the previous section allowed LIG synthesis without compromising the substrate, this time led to unviable and cracked LIG samples. Other information that can be retrieved from this matrix is that as the copper precursor VA ratio increases, lesser is the degradation that is laser-induced in the substrate. In terms of sample viability, from 13 tested combinations of laser power and speed, 5 of them were discarded since they provoked substrate destruction.

5.2.2.1 Morphological Characterization

The characterization by SEM was performed to investigate whether or not there was a synthesis of nanoparticles with the laser scanning. Figures 5.22 A) and B) show the LIG fibers coated with nanoparticles. In greater detail, in Figure 5.22 C) it can be seen that the nanoparticle size and shape are not uniform. In terms of size, it can be spotted some bigger clusters (with a size range between 100 and 500 nm) and the nanoparticles themselves (with a size smaller than 100 nm). As to the shape, most nanoparticles resemble a sphere.

Figure 5.22 D) shows the same sample region as Figure 5.22 B), but obtained using the EsB detector. This SEM operation mode is a suitable morphological characterization technique when there is a clear compositional contrast in the sample under study. The EsB detector highlights the material contrast between the CuNPs and the LIG fibers, in a way that the regions that corresponded to nanoparticles in the sample appear brighter in the image (since copper is an heavier element than both oxygen and carbon).

It is important to mention that when operating the SEM equipment it was noticed that the nanoparticle distribution in the LIG surface was not uniform, so there were regions on the sample where the nanoparticles were not displayed.

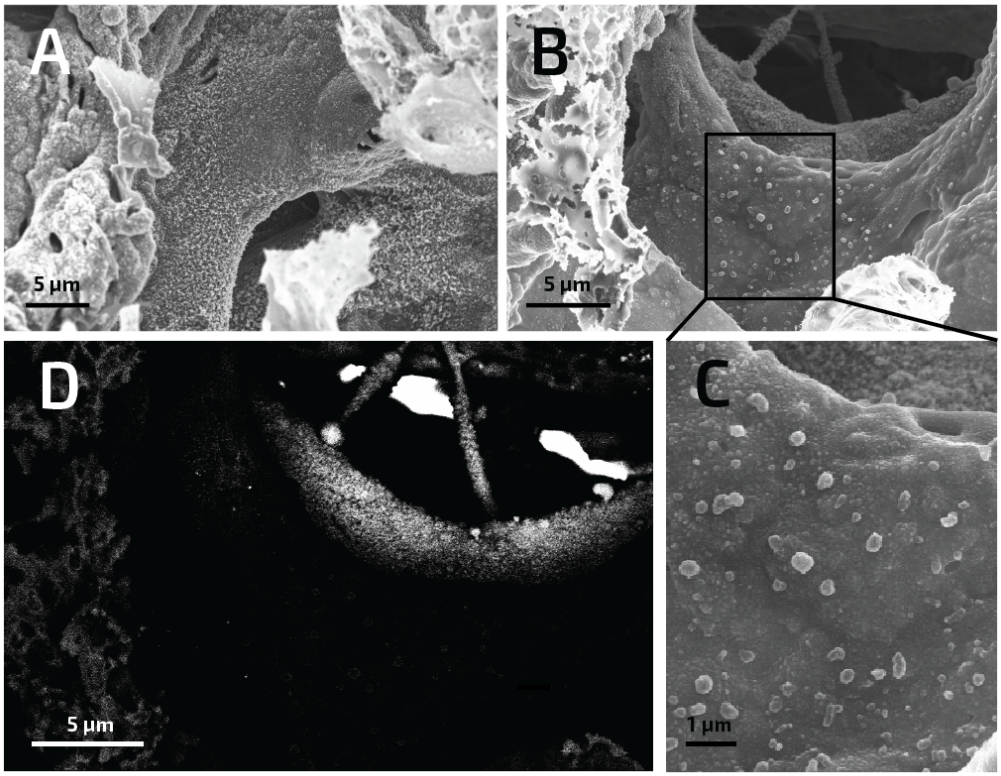

Figure 5.22: Morphological study of CuNPs-LIG composites. A) and B) represent SEM images obtained for a CuNPs-LIG sample using 1 μL mm^{-2} VA ratio of copper precursor and P4S4 for the laser parameters. C) shows an amplified image of B). D) SEM image obtained with the Energy selective Backscattered (EsB) detector.

5.2.2.2 Chemical Characterization

EDS analysis

With the SEM images, it was possible to observe that there were nanoparticles anchored to the surface of LIG structures and that their composition was different from the LIG fibers. To determine their elemental composition, an elemental analysis was performed by EDS (Figure 5.23). The results show that regions in Figure 5.23 B) that have a blueish color correspond to the zones in Figure 5.23 A) where the nanoparticles are located. In fact, by analyzing Figure 5.23 C), a more intense shade of blue appears in the center of the image, which means that copper is more concentrated in the areas containing nanoparticles. Considering Figure 5.23 G), first, it can be seen that sulfur relative percentage in the sample is insignificant. Sulfur, previously present in the structures resulting from the crystallization of copper sulfate, decreased from 4.7 to 1.4 %. This indicates that, with laser scanning, sulfur is largely released from the sample, probably as sulfur dioxide (SO_2). As a consequence, the ratio between copper and sulfur increased to approximately 9:1. Regarding the oxygen and carbon relative percentages, it can be said that there is

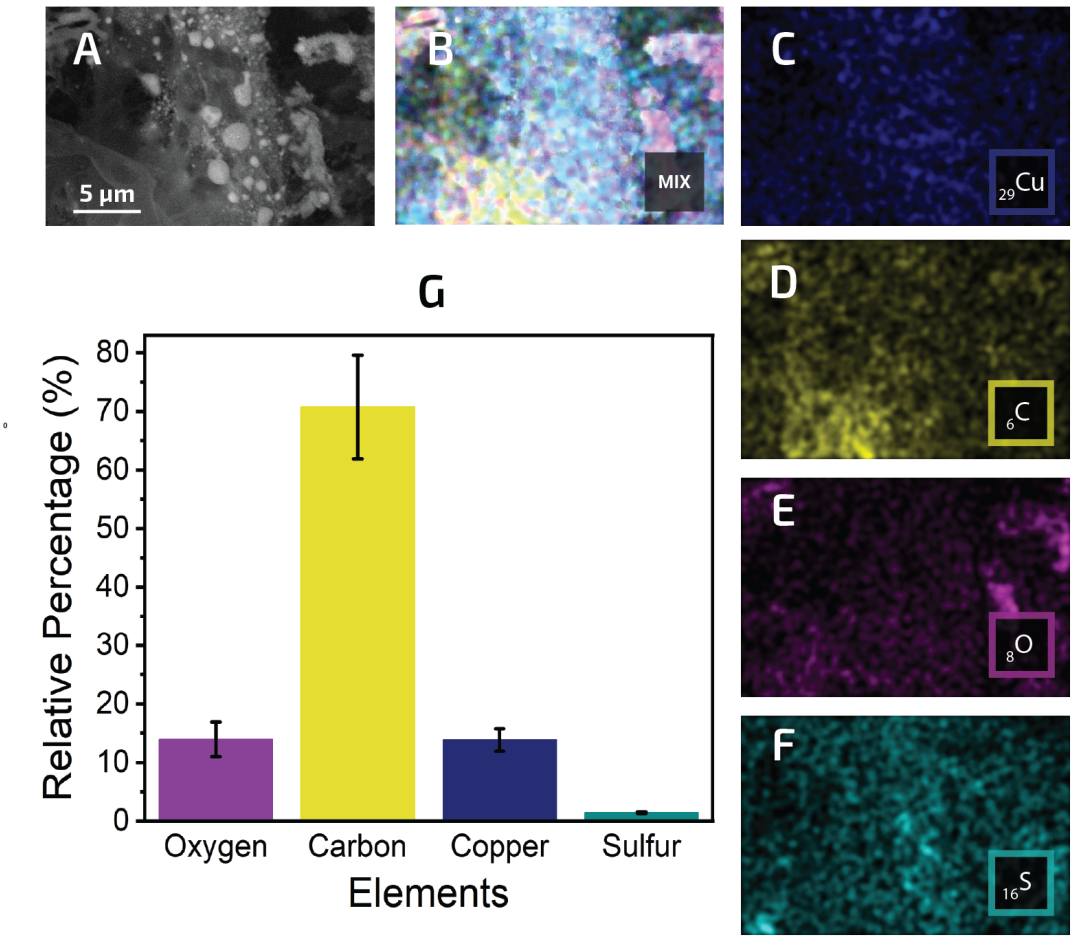

Figure 5.23: EDS analysis of CuNPs-LIG composites. A) SEM image of the sample area to be analysed, obtained with 1 μL mm^{-2} VA ratio of copper precursor and P4S4 laser parameters. EDS mappings of B) all four elements, C) copper, D) carbon, E) oxygen and F) sulfur. G) Relative elemental composition of the used sample.

an increase in the carbon content from 25 to 70.7 %, paired with a reduction in oxygen from 59.6 to 14 %. These results are expected since the laser induces carbonization of the paper substrate, which results in a release of a large portion of oxygen, together with LIG formation.

X-Ray Diffraction (XRD) analysis

Structural characterization of CuNPs-LIG composites was performed by XRD, through the identification of their crystalline structures. To better understand the influence of the laser in the formation of the nanoparticles, samples of pre-treated paper with deposited copper sulfate solution and the same substrate with a laser pass were analyzed. Figure 5.24A) shows the diffractograms obtained for each mentioned condition. Three characteristic peaks of cellulose type I, presented in Whatman paper, located at 2θ = 14.8 °,

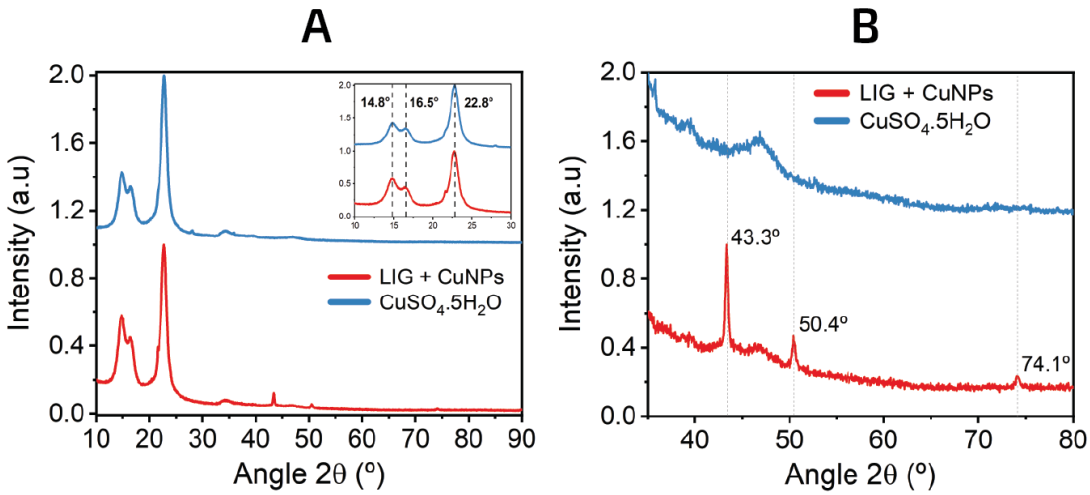

Figure 5.24: XRD analysis of CuNPs-LIG composites. A) XRD diffractogram obtained for a sample produced with 1 μL mm^{-2} VA ratio of copper precursor and the same sample submitted to a laser scan using P4S4 as the laser parameters, for an angle range of 10 ° to 90 °. The inset shows the same diffractogram from 10 ° to 30 °. B) shows a magnified version of A), obtained for angles between 35 ° and 80 °. In both figures the diffraction peaks are identified.

2θ = 16.5 ° and 2θ = 22.8 ° are distinctly visible in both samples [128]. Shrinking the observation window to the range of 30–80 ° (5.24B), three major peaks at 43.3, 50.5, and 74.1 ° can be assigned to the diffraction from the (1 1 1), (2 0 0) and (2 2 0) crystal planes of metallic copper phase, respectively [115]. These results confirm that crystalline CuNPs are successfully synthetized through laser along with LIG.

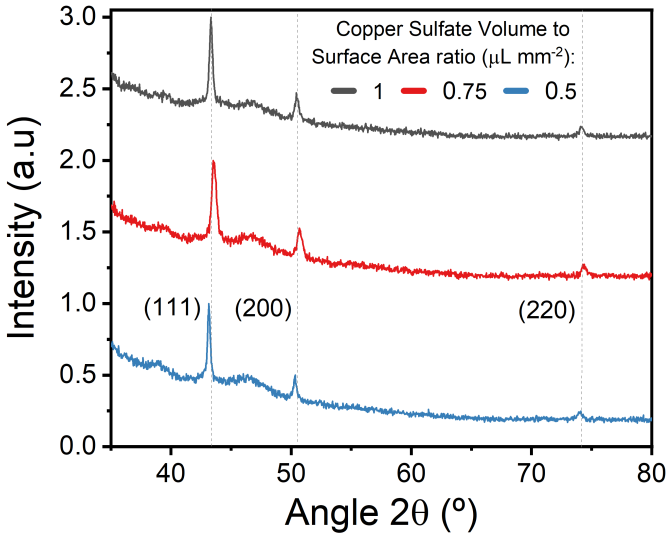

Figure 5.25: XRD diffractograms obtained for different copper precursor VA ratios of CuNPs-LIG composites. The sample was fabricated using the laser parameters P4S4.

Additionally, XRD technique was performed on LIG samples with different VA ratios of copper precursor to investigate the influence of this modification in the fabricated

CuNPs. In Figure 5.25 the planes that correspond to the diffraction peaks of metallic copper are identified. The results indicate that there are no significant differences between samples produced with different VA ratios of copper precursor, and all samples present the same diffraction peaks, namely the ones that belong to the metallic copper phase. This leads to the belief that variations in the volumes of the deposited copper precursor solution do not affect the composition of the laser-induced nanoparticles.

XPS analysis

XPS was used to complement information acquired from XRD measurements, by analysing the chemical state and composition of CuNPs-LIG composites. Figure 5.26 A) compares the survey scans for LIG and CuNPs-LIG samples. The spectrum indicate the presence of the same elements (carbon, oxygen and sodium) except for the copper element, which is only identified in the CuNPs-LIG sample. Figure 5.26 B) shows the high-resolution spectrum of C 1 s of CuNPs-LIG composite, which is similar to the one presented in Section 5.1.1.2 for LIG, confirming the conversion of cellulose fibers into LIG. Concerning the high-resolution Cu 2p XPS spectrum of the CuNPs-LIG surface

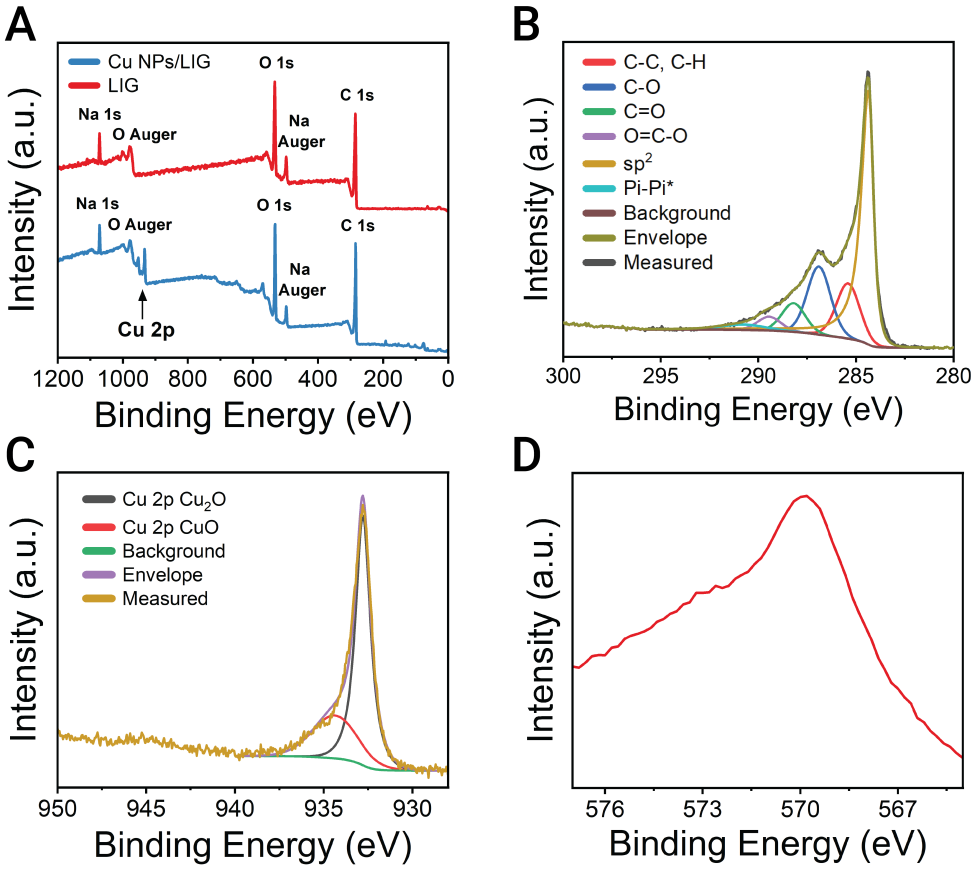

Figure 5.26: XPS analysis of CuNPs-LIG composites. A) Survey XPS spectra of LIG and CuNPs-LIG composites. B) XPS spectrum of C 1s peaks of CuNPs-LIG. C) XPS spectrum of Cu 2p peaks of CuNPs-LIG. D) Cu LMM Auger spectrum of CuNPs-LIG.

Figure 5.26 C), the results show that at least two copper species with different chemical states are present in the sample. The peak located at 934.4 eV can be assigned to CuO (or Cu(II)) [131], while the peak with the binding energy of 932.8 eV could not be identified by simply analyzing the Cu 2p XPS spectrum. Since the Cu(0) and Cu(I) species have similar binding energies, they can be distinguished through the Auger parameter (calculated through the sum of the Cu LMM kinetic energy and the Cu 2p3/2 binding energy). Figure 5.26 D) shows the Cu LMM Auger spectrum, with a dominant peak located at 569.8 eV (corresponds to a kinetic energy of 916.89 eV). This corresponds to an auger parameter of 1849.4, characteristic of Cu_2O (or Cu(I)) [132].

The presence of a small amount of CuO may be related to the oxidation suffered from the superficial copper elements when exposed to the air. The fact that XPS analysis suggested the presence of different oxidation states of copper, when compared to XRD measurements, may be explained by XPS being a material surface analysis and XRD a technique for detecting crystalline materials. With that said, metallic copper with a crystalline structure can be located in deeper LIG fibers and the superficial CuO and Cu_2O are both amorphous species. Combining these two analysis, it can be affirmed the presence of a mixture of the copper and copper oxide species in the CuNPs-LIG composites.

Raman analysis

Raman spectroscopy was used to evaluate the LIG quality in CuNPs-LIG samples. Figure 5.27 shows the Raman spectrum obtained for the mentioned sample. The three

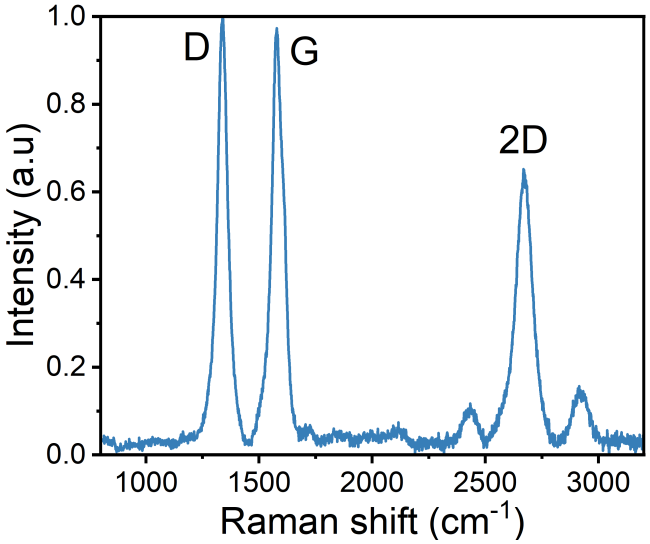

Figure 5.27: Raman analysis of CuNPs-LIG. Raman spectrum obtained for CuNPs-LIG composites produced using P4S4 as the laser parameters.

Raman peaks characteristic of graphene D, G and 2D are visible at 1339, 1583 and 2668 cm^{-1}. The D peak is now found to be the one with the highest intensity, when comparing

the Raman spectra obtained for the CuNPs-LIG with the LIG samples. Consequently, the I_D/I_G ratio increased to 1.03, which indicates that there is a bigger density of defects and a more disordered lattice structure, probably related to the presence of a higher percentage of amorphous carbon that was not converted to LIG in these CuNPs-LIG samples. As to the I_{2D}/I_G ratio of 0.67, although it has increased slightly, this value suggests that the number of LIG layers has not changed significantly.

5.2.2.3 Electrical Characterization

For these seven possible power and speed combinations that allowed the induction of graphene without damaging the substrate, sheet resistance tests were performed for all four copper precursor VA ratios. By analysing Figure 5.28 it is not possible to establish a clear trend with regard to the link between the sheet resistance values with the increase of the copper sulfate VA ratios in the samples, for a fixed combination of laser parameters.

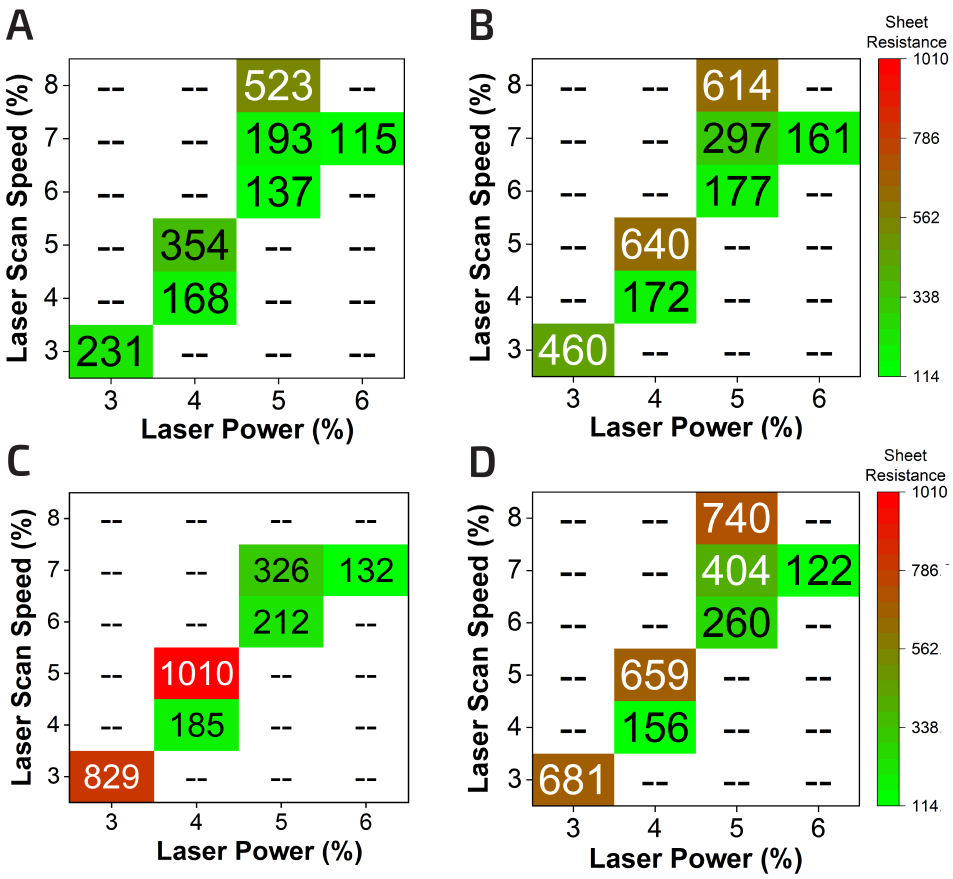

Figure 5.28: Electrical characterization of CuNPs-LIG composites. Sheet resistance matrices as a function of power and speed parameters, obtained for A) 0.25, B) 0.5, C) 0.75 and D) 1 μL mm^{-2} VA ratios of copper precursor.

From all samples, the sheet resistance values varied from 114 to 1010 Ω sq^{-1}, which shows that laser parameters have a huge influence on this resistance measure in LIG samples modified with copper sulfate. Comparing these results with those obtained in

the previous Section 5.1, it can be said that copper sulfate addition has a negative effect on the electrical conductivity of the samples, which was expected. Although copper is notable for its high conductivity, reference values show that the electrical conductivity of graphene can be as much as 70 % higher than copper's [133]. With that said, the results obtained for sheet resistance measurements are aligned with the literature.

Nevertheless, two laser power and speed combinations stand out due to their low sheet resistance measurements in the four samples with different VA ratios, P4S4 and P6S7 coordinates.

5.2.2.4 Electrochemical Characterization

The electrochemical performance was evaluated for the two conditions that resulted in improved sheet resistance values, considering the seven laser parameter combinations tested. CV experiments were performed on sensors fabricated with the rounded design selected in Section 5.1, except that the WE was modified with CuNPs.

Initially, it was thought of a configuration that could maximize the electrochemical properties of the sensor, by combining the laser parameters that resulted in the best electron transfer kinetics for the LIG sensor and the CuNPs-LIG sensor. This would allow to fabricate a sensor with optimized laser parameters for the three electrodes except for the functional area of the WE. The region that contained the CuNPs would be produced with a second combination of laser power and speed parameters that would not perforate the substrate. In fact, these sensors were fabricated, with the design shown in Figure 5.29 A). However, when performing CV sets, they led to solution leakages (Figure 5.29

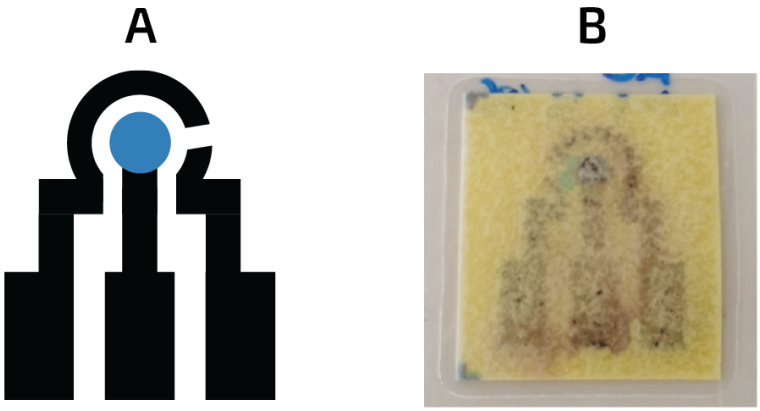

Figure 5.29: Sensor design for optimized laser parameters. A) In this image, black corresponds to the optimized laser parameters for LIG and blue refers to the CuNPs-LIG. B) Back of the sensor after CV experiments.

B). When the vector image intended to be engraved is configured with more than one condition of the power and speed parameters, the laser sections the design by that number of parameters. In this case, the laser performs the first condition line by line and when it performs the second condition, which corresponds to the circular area of the WE, there

is a small overlap in the transition region of the copper sulfate and wax substrate. With that said, a possible explanation for this infiltration is a higher substrate degradation in this zone. Thus, this design was discarded, and sensors were engraved with the same combination of laser power and speed parameters in all three electrodes.

Figure 5.30 A) shows the obtained cyclic voltammograms for a sensor produced with P6S7 laser parameters and a 0.5 μL mm^{-2} VA ratio of copper precursor. By analysis of the

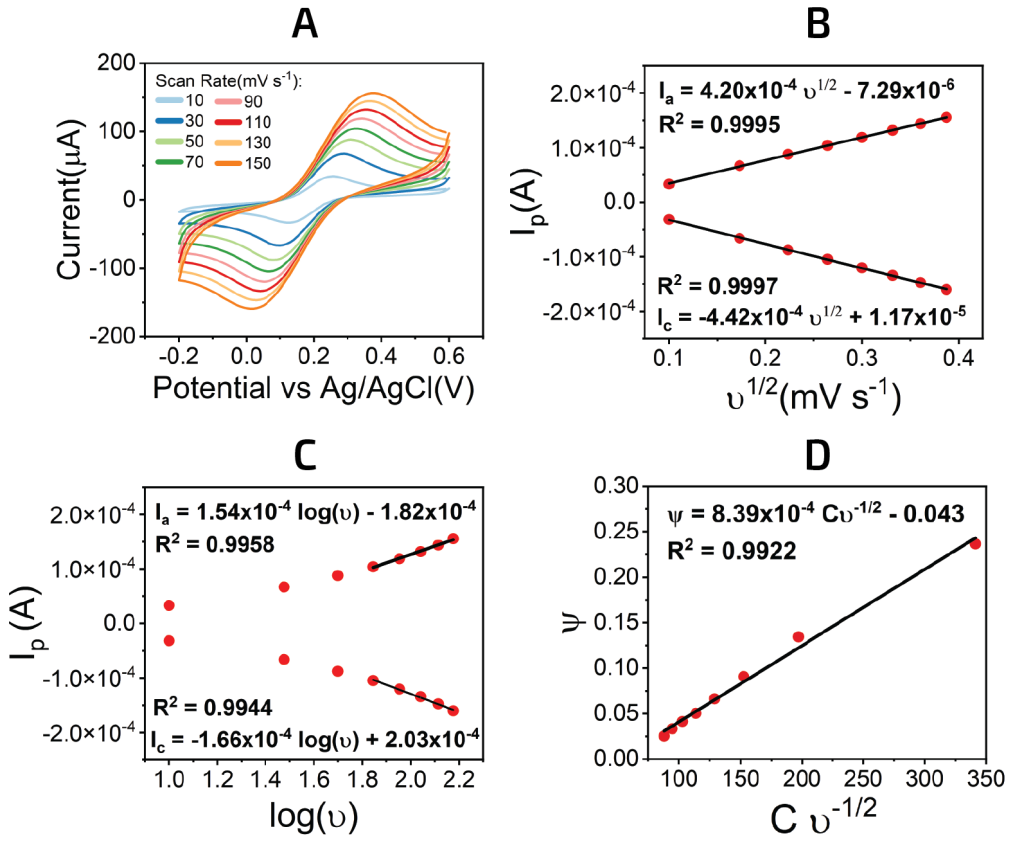

Figure 5.30: Electrochemical characterization of CuNPs-LIG composites. A) Voltammogram obtained for a sample with 0.5 μL mm^{-2} VA ratio of copper precursor and P6S7 as the laser parameters, for the scan rate range of 10 to 150 mV s^{-1} using 5 × 10^{-3} M $Fe(CN)_6^{3-/4-}$ as redox probe. B) Plot of peak currents vs square root of corresponding scan rate. C) Plot of anodic and cathodic peak currents vs logarithm of scan rate. D) Plot of the kinetic parameter Ψ vs $C\,v^{-1/2}$.

results, it can be said that the scan rates from 50 to 150 mV s^{-1} produced voltammograms with a peak separation from 230 to 360 mV. Since Equation 2.8 is only suitable for $\Delta E_p < 220mV$, Equation 2.7 was used for the determination of k^0 in sensors containing CuNPs. Except for this alteration, the methodology used to extract the A_e and k^0 parameters was the same as described in Section 5.1.4. In Figures 5.30 B), C) and D) are shown the auxiliary graphs used for the determination of the electrochemical parameters.

This process was repeated for the two mentioned combinations of laser parameters, for all VA ratios of copper precursor (Figure 5.31). By analysis of the results, not many conclusions can be retrieved from the voltammograms obtained, since there is not a clear

trend when relating the peak separation or peak currents with the VA ratios of copper precursor.

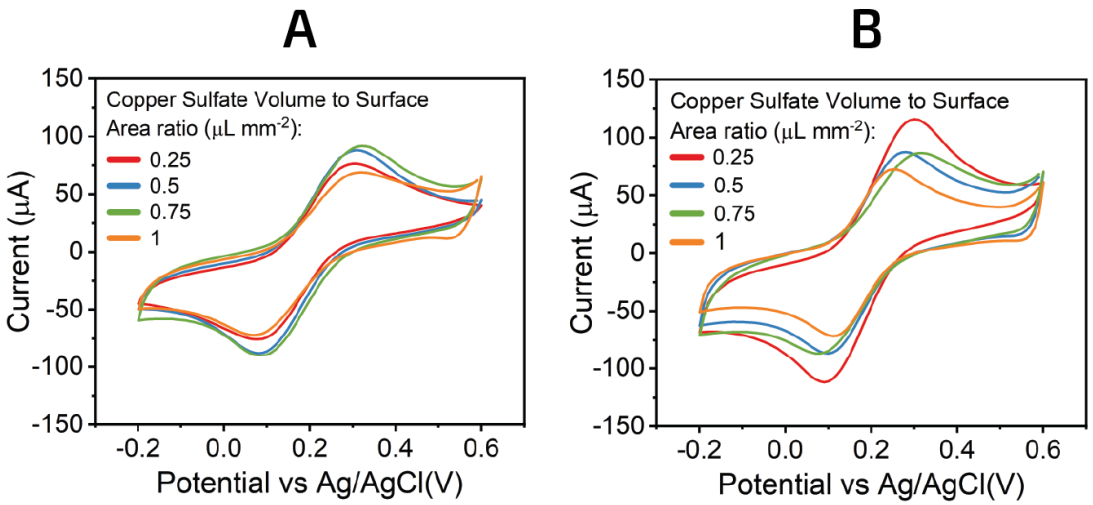

Figure 5.31: Comparison of the electrochemical performance of CuNPs-LIG sensors for different laser parameters. Voltammograms obtained for all VA ratios of copper precursor, for A) P6S7 and B) P4S4 laser parameters, using a scan rate of 50 mV s^{-1} and 5×10^{-3} M $Fe(CN)_6^{3-/4-}$ as redox probe.

To better understand the actual performance of the sensors, Table 5.5 presents the A_e and k^0 parameters extracted for each sensor. Firstly, comparing the LIG-based sensors, described in Section 5.1, with these CuNPs-LIG sensors, it can be said that the electrochemical performance of the second-mentioned decreased substantially. This can be verified by the general decrease of the A_e parameter and the k^0 values have dropped by one order of magnitude (even though this parameter was determined through a different method). These differences in electrochemical parameters may be related to how the laser acts on the substrate. Considering the case where the substrate was only composed of paper, all the energy deposited by the laser was used for the photothermal conversion of cellulose fibers into graphitic material. In this case, where the copper precursor solution was deposited on the paper, the laser energy will be divided into two parts: one part will continue to result in the carbonization of the paper, while the other part will be allocated to the synthesis of nanoparticles from the precursor solution. This premise can be corroborated by the previous Raman and EDS results. Taking into account the Raman results, the increase of the I_D/I_G ratio of CuNPs-LIG compared to the LIG samples, paired with the decrease of the I_{2D}/I_G ratio, suggest that in the first-mentioned there is not such a good conversion of the substrate into LIG. Considering now the EDS analysis, LIG samples presented an oxygen and carbon content of 9.4 and 90.6 %, respectively, for P4S4 laser parameters. For the same operational conditions, samples with CuNPs-LIG composites presented an increase in the relative composition of oxygen and a decrease of carbon content, to 16.5 and 83.5%, respectively (these percentages were adjusted from the EDS

results shown in Section 5.2.2.2, so that oxygen and carbon were the only elements in the sample taking into consideration). These percentages prove that, on a paper substrate with copper sulfate, the laser scanning is not as effective in converting paper into LIG as on a paper-only substrate.

Table 5.5: A_e and k^0 parameters of CuNPs-LIG sensors produced at different laser power and speed conditions.

Laser Parameters	**P6S7**				**P4S4**			
VA ratios (μL mm^{-2})	**0.25**	**0.5**	**0.75**	**1**	**0.25**	**0.5**	**0.75**	**1**
$\boldsymbol{A_e}$ (mm^2)	10	12	13	10	17	16	15	12
k0 *(10^{-2} mm s^{-1})*	0.72	0.84	0.91	0.81	0.92	0.88	0.8	0.67

Apart from the comparison with the LIG sensors, the results of the sensors produced with the P4S4 laser parameters suggest a relation with the copper precursor VA ratios. As the volume of the drop-casted copper solution increases, the values of the A_e and k^0 parameters worsen. This poorer electrochemical performance of sensors produced with higher volumes of copper sulfate is aligned with the previously presented theory. Since there is a larger volume of copper precursor for the same amount of paper, for the same energy deposited by the laser, the portion used for converting the paper fibers into LIG will decrease and the one used to form CuNPs will be higher.

Nevertheless, worse A_e and k^0 values do not necessarily indicate that these sensors exhibit a weaker response to glucose. With these results, it was decided to pursue the glucose tests with CuNPs-LIG sensors produced with P4S4 laser parameters. Not only just by the fact that overall this operational condition led to improved A_e when compared to the P6S7 combination of power and speed, but also this last mentioned, due to its elevated porosity, some sensors experienced solution leakages.

5.3 Glucose sensing performance

Testing the performance of CuNPs and LIG based sensor toward glucose was the ultimate goal of this work. In this section the step-by-step reactions that lead to the formation of copper and copper oxides with different oxidation states were studied. Both discrete and continuous glucose measurements were carried out, with the respective sensor calibrations. Lastly, a cost analysis of the proposed sensor was performed.

5.3.1 Electro-oxidation mechanism

Since the mechanism of the glucose electro-oxidation is based on the ability of copper to change its oxidation states by reacting with the ion OH^-, as mentioned in Section 2.3.2, all experiments were performed in a 0.1 M NaOH solution. Figure 5.32 shows the voltammogram obtained for the CuNPs-LIG sensor when cycling the potential between -1 and 1 V.

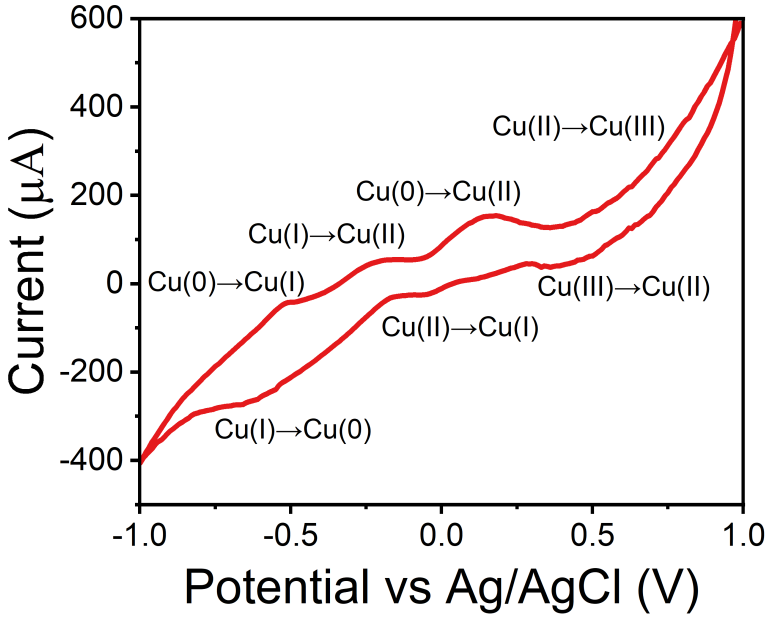

Figure 5.32: Cyclic voltammogram of CuNPs-LIG sensor. Experiment performed at sensor produced with 1 μL mm^{-2} of copper precursor VA ratio, at a scan rate of 10 mV s^{-1} in 0.1 M NaOH solution.

This experiment was performed to identify the oxidation and reduction peaks, related to the formation of different electrochemically active species. As demonstrated before, the WE of the developed sensor is composed of Cu(0), through XRD analysis and Cu(I) and Cu(II), through XPS. Since the glucose oxidation can be attributed to the conversion of Cu(II) to Cu(III) in an alkaline solution, next, the chemical reactions related to the transformation of Cu(0) in Cu (I), Cu(II), and Cu(III) are presented and correlated with the multiple peaks visible on the graph. According to the literature [70, 134–136], it

can be concluded that, during the upscan of the voltage, the copper oxidation process is initiated with the Cu(0) to Cu(I) transition, described by the following reaction:

$$2Cu + 2OH^- \rightarrow Cu_2O + H_2O + 2e^- \tag{5.2}$$

This first peak at -0.5 V is followed by the conversion of Cu(I) in Cu(II), at approximately -0.2 V:

$$Cu_2O + 2OH^- \rightarrow 2CuO + H_2O + 2e^- \tag{5.3}$$

$$Cu_2O + 2OH^- \rightarrow 2Cu(OH)_2 + 2e^- \tag{5.4}$$

The last visible oxidation peak, at around 0.16 V, can be attributed to the transformation of Cu(0) in Cu(II):

$$Cu + 2OH^- + H_2O \rightarrow Cu(OH)_2 + 2e^- \tag{5.5}$$

$$Cu + 2OH^- \rightarrow CuO + H_2O + 2e^- \tag{5.6}$$

Cu(II) ions in an alkaline solution are known to undergo the following reactions, to form Cu(III) oxides:

$$Cu(OH)_2 + OH^- \rightarrow CuOOH + 2H_2O + e^- \tag{5.7}$$

$$CuO + OH^- \rightarrow CuOOH + e^- \tag{5.8}$$

$$CuO + H_2O + 2OH^- \rightarrow Cu(OH)_4^- + e^- \tag{5.9}$$

$$Cu(OH)_2 + 2OH^- \rightarrow Cu(OH)_4^- + e^- \tag{5.10}$$

These step-by-step reactions led to the formation of Cu(II) species, that by donating one electron to form Cu(III), in the presence of glucose act as the active substances for its oxidation. In this case, the formation of Cu(III) is not visible on the graph, which may be related to the fact that its oxidation peak can only be discernible at high hydroxide concentration [136].

Submitting the LIG and CuNPs-LIG sensors to a 0.1 M NaOH solution, with and without the presence of glucose, allowed to understand the vital role of Cu(III) as a glucose oxidizing agent. As it can be seen from Figure 5.33, the LIG sensor shows almost no alteration in current response, when comparing the two situations before and after adding glucose, while the same is not verified for the CuNPs-LIG sensor. In the last mentioned, in addition to the fact that the the overall electrical current generated is much

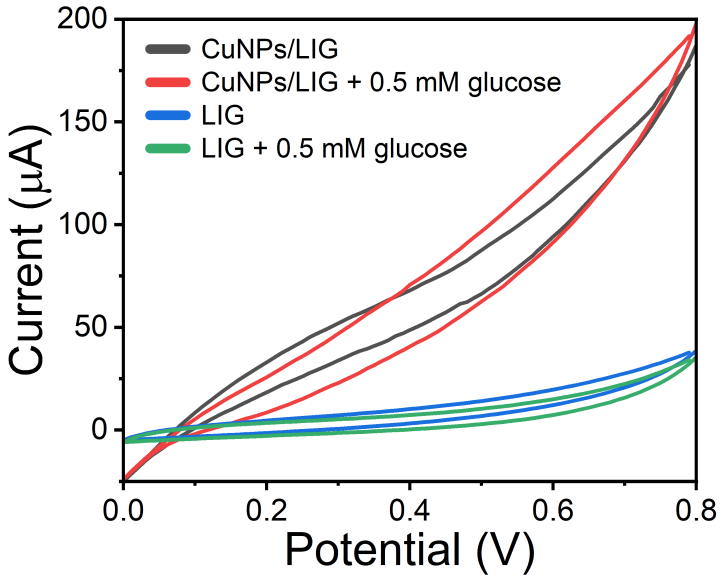

Figure 5.33: Cyclic voltammograms of LIG and CuNPs-LIG sensors in the absence and presence of glucose. The CuNPs-LIG used sensor was produced with 1 μL mm^{-2} of copper precursor VA ratio and all experiments were performed at a scan rate of 75 mV s^{-1} in 0.1 M NaOH solution.

higher than that registered for the LIG-based sensor, in the situation where glucose was added there is a spike in current beginning at 0.4 V. This indicates that the produced sensors have a clear catalytic oxidation effect on glucose and that CuNPs are the most responsible medium for that electron transfer.

5.3.2 Copper precursor VA ratio selection

To explore and select the best copper precursor VA ratio, CuNPs-LIG sensors produced with different VA ratios were submitted to chronoamperometric sets, using the same applied potential. The criteria to select the copper precursor VA ratio to be used in the following experiments was based on which sensor had the highest current response for the same amount of glucose. To present these results, the baseline current was removed from graphs to allow a better comparison of the current responses between sensors fabricated with the different VA ratios. To do so, the baseline was considered for the time instant just before the current rise, after the addition of glucose, which in Figure 5.34 corresponded to 505 seconds.

To calculate the current increase with the glucose addition, current values were taken on 525 s instant, corresponding to a stabilization time of 20 seconds. Although this response time seems high, it has to be considered that the volumes of glucose added are minimal when compared to the total volume of the beaker and that the stirring of glucose into the NaOH solution is not instantaneous. With that said, it is expected that in a real context situation of glucose measurement, this response time will be much smaller. The values of 4.8, 6.5, 7, and 7.9 μA corresponded to the 0.25, 0.5, 0.75, and 1 μL mm^{-2} of

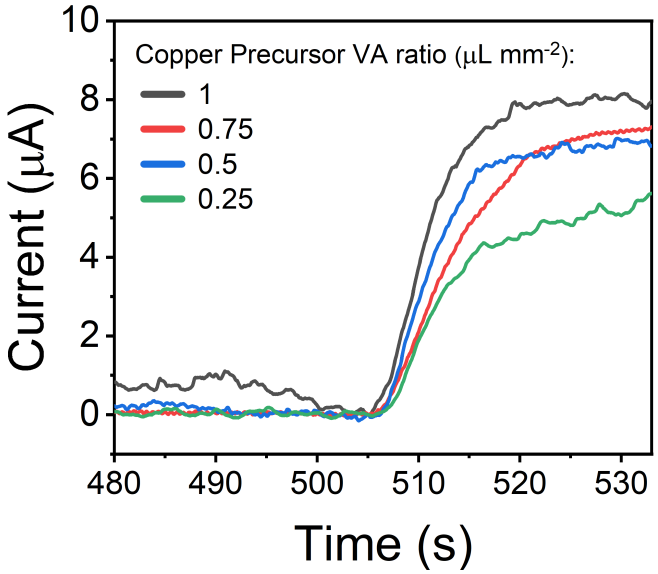

Figure 5.34: Chronoamperometric responses of the CuNPs-LIG sensors produced with different copper precursor VA ratios. The chronoamperograms were obtained using the glucose sensor at an applied potential of 0.5 V and 0.2 mM glucose additions.

copper precursor VA ratios, respectively. By analyzing these values and Figure 5.34, it is possible to conclude that there is a relation between the different copper precursor VA ratios and the corresponding current response. As the VA ratio of copper sulfate increases, the greater the increase in current. In fact, considering that higher VA ratios correspond to higher amounts of copper precursor, with the laser scanning, these sensors may possess a higher amount of CuNPs. With that said, since an increase in the electrical current promoted by a glucose addition is related to the electron transfer caused by Cu(III) and a higher initial copper concentration will correspond to a higher amount of Cu(III), through the chain of reactions, it was expected that the VA ratio of 1 μL mm^{-2} as the copper precursor had a better electrocatalytic performance. The other copper precursor VA ratios were discarded for the purpose of this thesis.

5.3.3 Discrete glucose measurement

After the selection of 1 μL mm^{-2} as the optimized copper precursor VA ratio, the chronoamperometric responses of the CuNPs-LIG sensor were studied as a function of increased concentrations of glucose. For this test, twice of each 0.1, 0.2, 0.4, 1, and 2 mM concentrations were added to the same beaker. Figure 5.35 A) shows the cumulative glucose concentration measured by the sensor after each new addition. It can be seen that the electrodes reach a steady-state current level very quickly, around 50 s, even though the measurements were made for 150 s. A simple analysis of the graph makes it possible to conclude that there is a notorious increase in the measured current when a particular glucose concentration is added to the beaker; this demonstrates that the CuNPs-LIG sensor successfully reacts to glucose, and, since all measurements were registered for the same

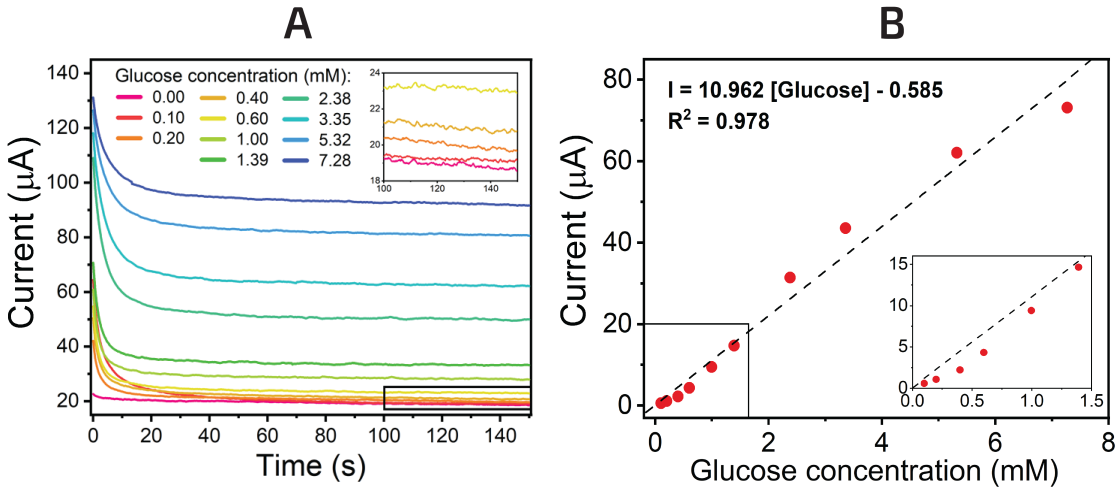

Figure 5.35: Chronoamperometric responses of the CuNPs-LIG electrode to different glucose concentrations. A) Chronoamperograms obtained using the glucose sensor at an applied potential of 0.4 V (the inset shows the magnified section for a time window of 100 to 150 seconds, belonging to the baseline and the first five applied concentrations of glucose). B) Correspondent calibration curve (the inset shows the magnified section considered for the first six glucose additions).

sensor, the application of this sensor to continuous glucose measurement is promising. Figure 5.35 B) shows the corresponding calibration curve. The calculated sensitivity (S) was 223.7 μA mM^{-1} cm^{-2}, which was calculated from the slope of the curve divided by the WE geometric area of the CuNPs-LIG sensor. Since this test was performed once, with the purpose of inferring on the sensor current dependence on glucose concentration, other sensing properties were not yet calculated.

5.3.4 Continuous glucose measurement

5.3.4.1 Potential selection

The following experiments, shown in Figure 5.36, were performed on the same glucose sensor, to select the most suitable potential to apply in the subsequent tests. Twice of each 0.02, 0.04, 0.1, 0.2, 0.4, 1, 2, and 4 mM glucose concentrations were successively added. As it is visible on the inset of Figure 5.36, the current response to the applied potential of 0.4 V for lower glucose concentrations is much more prominent when compared to the other potentials. For the 0.5 V potential, slight current variations can be detected; however, no well-defined steps are observed, and for the 0.6 V potential, only noise can be identified. Since these two concentrations, of 20 and 40 μM, are included within the glucose range in sweat (10–200 μM), and being the glucose detection in sweat the eventual application of this sensor, the 0.4 V potential was selected to pursue the following experiments.

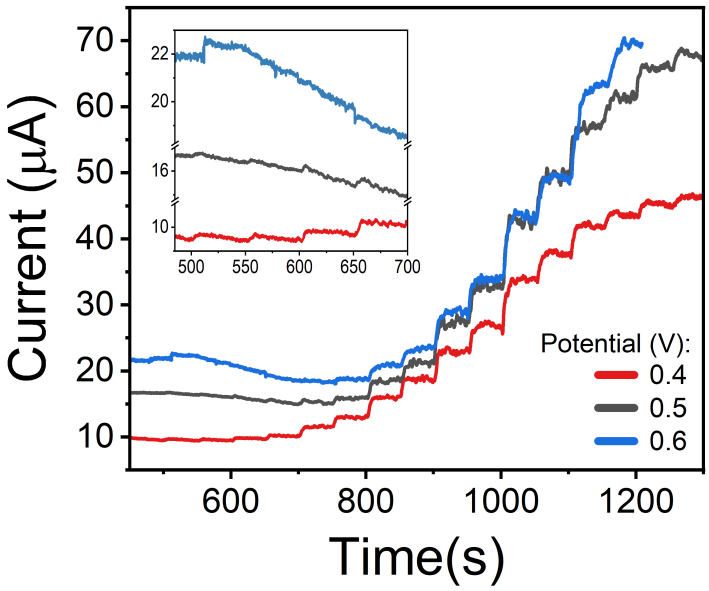

Figure 5.36: Continuous amperometric sensor response to different glucose concentrations and applied potentials. The chronoamperograms were obtained using the glucose sensor at 0.4, 0.5, and 0.6 V. The inset shows the magnified section of amperograms for a time window of 490 to 700 seconds, corresponding to the additions of the two lowest concentrations of glucose.

5.3.4.2 Calibration

Figure 5.37 illustrates the current calculation process for calibration, where the data extracted from the chronoamperograms was treated as follows:

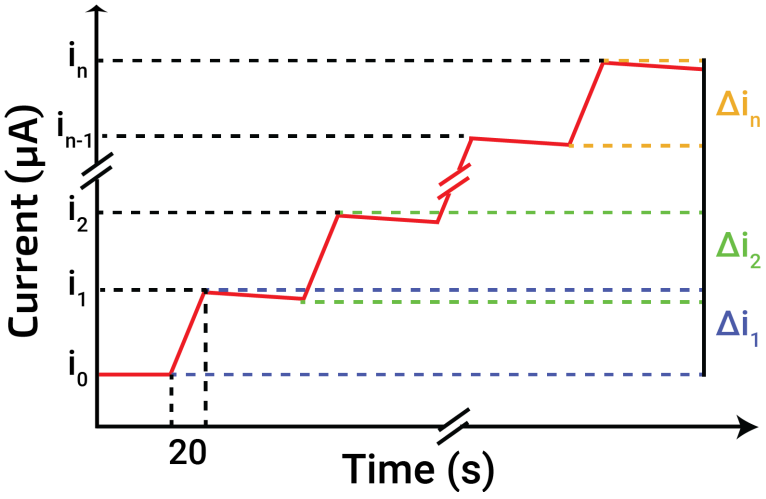

Figure 5.37: Schematic of the methodology adopted for signal processing.

1. The current values were extracted in the instant before each glucose addition and 20 seconds after that, which was the time interval for the current stabilization;

2. Next, the i_{n-1} value was subtracted from the i_n to determine the current variation (Δi_n) corresponding to each glucose addition;

3. Finally, the Δi_n value was added to the cumulative current responses previously registered ($\sum_{m=1}^{n} \Delta i_{n-1}$) so that each current response is dependent on the total glucose concentration inside the beaker.

It is important to note that for the first glucose addition, the current was calculated just with the subtraction of i_0 from i_1. Instead of simply subtracting the baseline i_0 to the i_n value, the current corresponding to the total glucose concentration was calculated as described in item 3 due to its non-stabilization. By way of explanation, although a clear distinction in different steps correlated to glucose additions can be visible in Figure 5.36, there is always experienced a slight current decrease between the moment it stabilizes and the exact instant before the subsequent glucose addition. So, this calculation method allows for a more realistic calibration, without current losses.

In Figure 5.38 A) the obtained amperograms for three different sensors using the same protocol are presented and Figure 5.38 B) shows the corresponding calibration curve calculated for the 0.4 V potential. By analyzing the graph, it is possible to notice

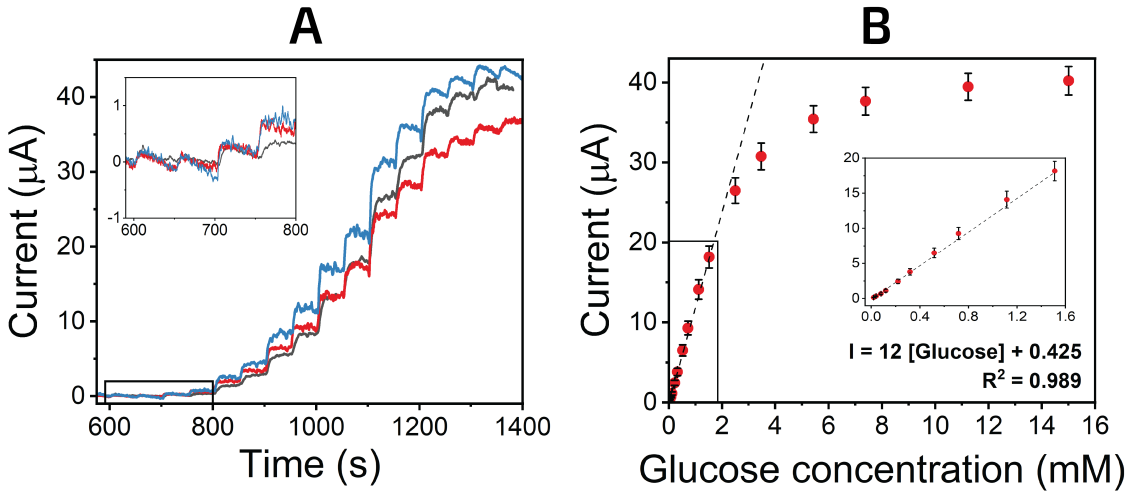

Figure 5.38: The dependence of the current response vs. glucose concentration. A) Amperometric sensor responses of three sensors to different glucose concentrations, for a 0.4 V applied potential; the inset shows the magnified section for a time window of 590 to 800 seconds, corresponding to the additions of the two lowest concentrations of glucose. B) The Correspondent calibration curve; the inset shows the magnified section considered for a linear range response.

that the sensor response to the addition of glucose loses linearity above a specific glucose concentration. At this point, additions of higher glucose concentrations correspond to equal or smaller current variations, meaning that the sensor is saturated. With that said, the glucose concentration range was considered linear from 0.02 to 1.51 mM. The calculated sensitivity (S) was 244.9 μA mM^{-1} cm^{-2}. Error bars were included using the standard deviation, and the detection limit of 14 μM (LOD) was calculated through the following equation:

$$LOD = 3\sigma/S \tag{5.11}$$

Another continuous measurement was made, this time by adding the same amount of glucose. This test allowed for sensitivity comparison between two different continuous tests and, since the glucose additions were very low, 0.1 mM each, a better definition of the linear range of the sensor was possible. Figure 5.39 shows the measurement results with the respective current variations calculated. As it can be seen in Figure 5.39 A), the

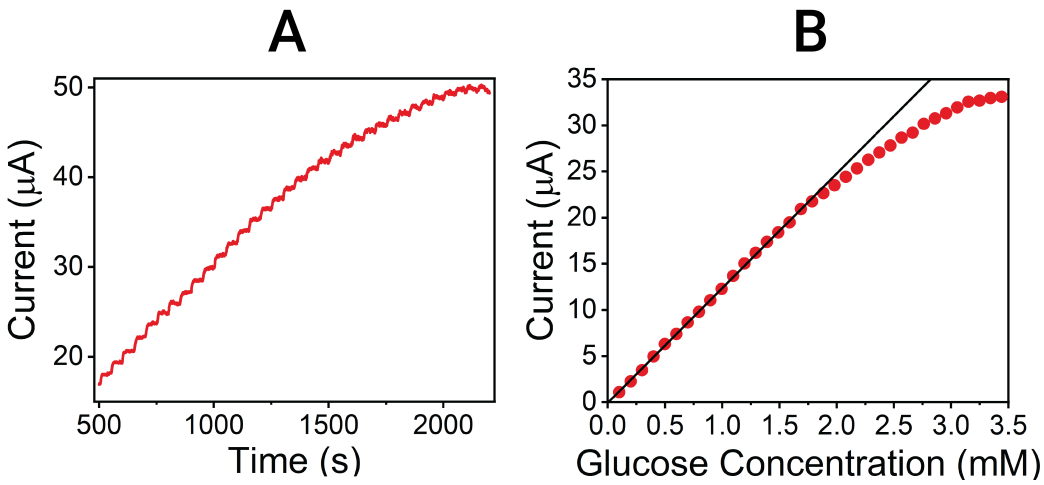

Figure 5.39: Sensor response to successive additions of 0.1 mM glucose. A) Continuous amperometric response obtained using an applied potential of 0.4 V. B) Representation of the current variations as a function of the total glucose concentration.

current response to successive glucose additions was registered until the sensor reached a complete saturation state. The calculations for the current increments were based on the same methodology presented before, and the linear fitting identified as a black line in Figure 5.39 B) shows at what glucose concentrations the sensor response is no longer linear. Again, the test with continuous 0.1 mM glucose additions was performed on two other sensors, for statistical purposes. The calibration results are presented in Figure 5.40. The current measured was linearly correlated to the glucose concentration from the first

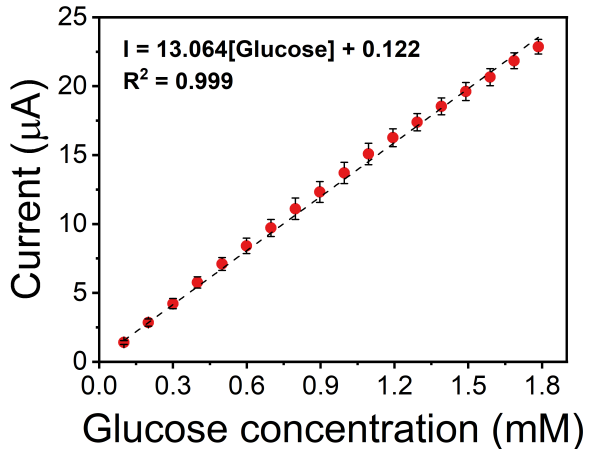

Figure 5.40: Calibration curve for continuous glucose measurements. Dependence of the current response vs. glucose concentration for the considered linear range of the sensor.

glucose addition of 0.1 mM until the total concentration of 1.79 mM. The sensitivity was estimated to be 266.53 μA mM^{-1} cm^{-2}, based on the WE area of the CuNPs-LIG sensor. Comparing the sensitivities for the two calibrations made with different glucose addition protocols, it can be said that the obtained values are very similar, which corroborates the sensor viability. The limit of detection of 11 μM was determined.

The sensing properties of several copper-based glucose sensors reported in published articles, as well as those related to the sensor developed in this work, are summarized in Table 5.6. The table shows that the performance of the proposed glucose sensor composed of CuNPs and LIG simultaneously synthesized through laser induction is comparable to other literature reports that use commonly known fabrication approaches.

Table 5.6: Comparison of the performance for several copper-based glucose sensors.

Materials	Nanoparticle Deposition Method	Linear Range	LOD (μM)	Sensitivity (mAμM^{-1}cm^{-2})	Ref.
Cu NPs, LIG, polyimide	Substrate-assisted electroless deposition	1 μM - 6 mM	0.39	495	[59]
Cu NPs, graphite sheet	Hydrothermal	0.1 - 3.4 mM	1.05	7254	[134]
CuO NPs, LIG, polyimide	Focused sunlight	1 μM - 5 mM	0.1	-	[37]
Cu NCs, LIG, polyimide	Electrodeposition	25 μM - 4 mM	0.025	4532	[107]
Cu NPs, LIG, polyimide	Electrodeposition	1 μM - 0.5 mM	-	84	[70]
Cu NPs, LIG, paper	Laser induction	20 μM - 1.79 mM	11	267	This work

Although the sensor sensitivity is highly satisfactory, some measures could be applied to improve this parameter, such as a slight increase in the copper precursor volume or concentration to maximize the current growth with the addition of glucose.

5.3.4.3 Reproducibility and Selectivity

Figure 5.41 A) shows the reproducibility tests, analyzed for six CuNPs-LIG sensors prepared with the same conditions. The amperometric responses were measured during the addition of 0.1 mM glucose in 0.1 M NaOH solution. The relative standard deviation of 2.84% was calculated, suggesting that the developed sensors have good glucose-sensing reproducibility.

A selectivity test was carried out by measuring the sensor response to the addition of interferents that usually are present in human sweat, along with glucose. Figure 5.41 B) presents the response of the CuNPs-LIG sensor for the consecutive addition of 1 mM glucose, 0.1 mM NaCl, 0.1 mM ascorbic acid and 0.1 mM uric acid. The results show that the presence of NaCl and uric acid interfering species produce almost negligible current

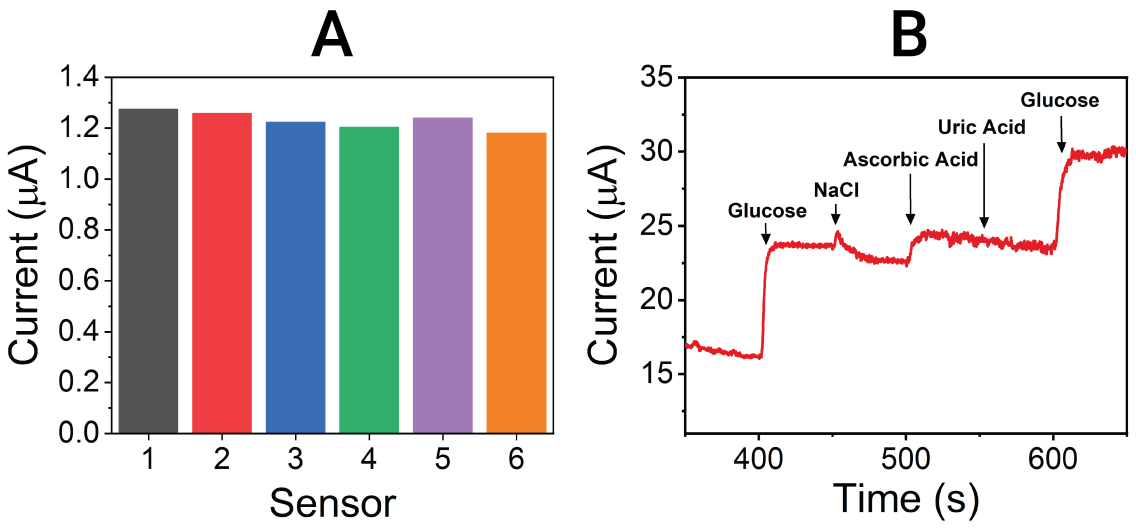

Figure 5.41: Reproducibility and selectivity studies. A) Reproducibility tests performed on six CuNPs-LIG sensors. B) Selectivity study for the addition of 1 mM glucose in the presence of interfering species (each 0.1 mM).

responses. Considering the ascorbic acid interference, although a slight increase in the sensor current response can be observed in the graph, that rise is not significant when compared to the glucose additions. It can be said that CuNPs and LIG composites act as selective catalytic materials towards glucose.

5.3.5 Cost analysis

Lastly, a cost-analysis of the optimized CuNPs-LIG sensor was performed. Table 5.7 presents the total cost related to the sensor fabrication, as well as the costs by material. As it can be seen, the calculated cost was approximately 2.22 cents per sensor, which is a very reasonable price compared to other alternatives available on the market. The most commercially successful test strips, associated with the fingerstick glucose meters, have a current market value rounding 0.17 to 0.9 €[137]. This price window is related to different characteristics of the glucose detection method, such as the amount of blood required, the time to result, and their compatibility with meter models. In this analysis, it was not included the energetic costs associated with the use of the following equipment: the CO_2 laser to synthesize LIG, the commercial pouch laminator to encapsulate the electrodes, and the hotplate to dry the sensor's Ag and Ag/AgCl inks. Although these electrical costs were not summarized in the table, they are considered insignificant compared to the value of other materials. With that said, the sensor developed in this thesis presents production costs that are much lower than those mentioned above, which fulfills one of the main objectives of this thesis, the development of a low-cost glucose sensor.

Table 5.7: Cost analysis of CuNPs-LIG sensors produced in paper substrate.

Material	Price/Quantity	Quantity/Sensor	Price/Sensor
Whatman Paper	5.96×10^{-4} €/cm^2	3.75 cm^2	2.24×10^{-3} €
Wax	5.38×10^{-5} €/cm^2	3.75 cm^2	1.98×10^{-4} €
Sodium Tetraborate	8.22×10^{-2} €/g	9.17×10^{-3} g	7.54×10^{-4} €
Silver Ink	2.92 €/g	3.6×10^{-3} g	1.05×10^{-2} €
Silver/Silver Chloride Ink	4.26 €/g	4×10^{-4} g	1.7×10^{-3} €
Laminating pouches	1.8×10^{-3} €/cm^2	3.75 cm^2	6.75×10^{-3} €
Copper Sulfate	1.76×10^{-1} €/g	1.6×10^{-4} g	2.82×10^{-5} €
		Total	2.22×10^{-2} €

5.4 Non-invasive wearable sensor

As an attempt to integrate the developed sensor in a wearable and non-invasive system for glucose detection in sweat, Figure 5.42 shows a first prototype of the LIG biosensor. The design includes an iontophoretic system to induce sweat generation, represented by the two iontophoresis electrodes, and the electrochemical sensor for glucose detection in sweat produced in this thesis. The concept for the sweat stimulation would be realized by placing a hydrogel containing pilocarpine (a sweat-inducing agent) underneath the iontophoresis electrodes and the generated sweat would be used for glucose detection. This design was first engraved in the pretreated paper substrate, as all fabricated sensors in this work, and then the whole functional pattern was transferred to polyurethane tape, using a method developed at CENIMAT/i3N. The substrate used was selected due to its flexible and adhesive properties that ensure high conformability to curvilinear body parts and allow for the development of skin-worn patches.

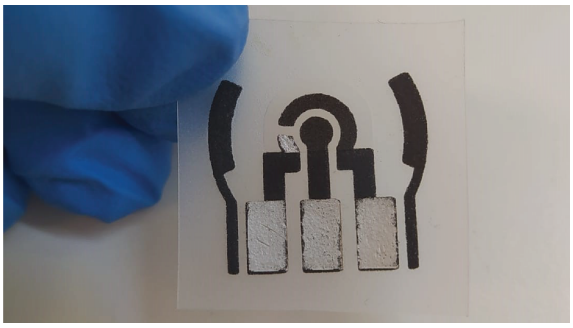

Figure 5.42: Wearable sensor for glucose detection in sweat. Fabricated sensor with printed Ag/AgCl RE, LIG Counter Electrode (CE) and CuNPs-LIG WE over the Polyurethane tape.

6

Conclusion and future perspectives

This work focused on the development of a CuNPs-LIG based non-enzymatic glucose sensor. A new and simple fabrication method was developed to produce the glucose-sensing electrode, which does not require high-cost materials or complex fabrication procedures. In this method, a copper precursor solution was drop-casted to a paper substrate, and through a single laser irradiation step, both CuNPs and LIG were simultaneously synthesized.

An initial LIG study was performed, to optimize some fabrication conditions that have a significant impact on LIG electron transfer properties. The laser parameters of power, speed, platform height, and the number of scans were optimized through different characterization techniques such as SEM, EDS, Raman spectroscopy, XPS, four-point probe sheet resistance measurements, CV and Impedance spectroscopy. It was noted that the LIG formation region was concentrated for similar percentages of laser power and speed. Also, SEM and EDS results showed that a more intense and in-depth LIG synthesis occurs for higher percentages of these laser parameters. Sheet resistance measurements allowed to select the z=-0.1" as the optimized height for the LIG fabrication and indicated that the electrical properties improve with the increase in the number of laser scans, obtaining a sheet resistance value as low as 14.8 Ω sq^{-1} for P7S8 conditions and two laser passes. The electrochemical characterization of LIG-based sensors was aligned with the electrical one: the combination of P7S8 laser conditions for a double scan exhibited the highest A_e and k^0 parameter values of all and for a single scan, the better electrochemical properties were registered for LIG synthesized through P6S6 parameters. This optimization not only adds value to this thesis but also contributes to an improvement in the flexible and sustainable electronics area since it provides an extensive and complete characterization of LIG synthesized on paper.

A CuNPs-LIG optimization was performed based on the set of laser parameter combinations that allowed the LIG formation at the selected height, for four different copper sulfate VA ratios. It was noticed a more intense substrate ablation, when compared to LIG synthesis, and this was also verified for the lower copper precursor VA ratios. For

that reason, despite LIG optimization showing better electrical and electrochemical properties for more than one laser scan, the number of scans was not studied on these samples. SEM images allowed to affirm that nanoparticles were successfully embedded on LIG fibers and EDS results confirmed that their elemental composition was based on copper. XRD technique was used to assess the nanoparticles' crystallographic structure and measurements confirmed the presence of Cu(0), through the identification of three strong diffraction peaks that corresponded to different crystal planes of metallic copper. XPS measurements also confirmed the existence of additional +1 and +2 copper oxidation states in a CuNPs-LIG sample. Electrical characterization was carried-out and, although the overall sheet resistance values were higher than those measured for the LIG samples, the laser parameters P4S4 and P6S7 stand out within the other combinations due to their improved electrical properties. Sensors fabricated with the P6S7 parameters led to solution leakages, when performing CV technique, so the P4S4 laser operating conditions were selected to pursue the glucose sensing tests.

The electrochemical behavior of the CuNPs-LIG sensor was studied by CV and the change in copper oxidation states was observed. Regarding the glucose-sensing performance, firstly it was verified that LIG sensors produced no significant response to the glucose addition, while for CuNPs-LIG sensors a much higher current response was registered in the presence of glucose. Moreover, by a simple chronoamperometric test, it was concluded that the 1 μL mm^{-2} of copper precursor VA ratio in the WE caused the highest current response to the same amount of glucose. The sensor was tested in both single and continuous modalities. Different applied potentials were tested on amperometric measurements and the 0.4 V was defined as the most suitable for detecting highest current responses in lower glucose concentrations. Two methods, based on distinct glucose addition protocols, were applied to effect the sensor calibration. The sensor exhibited a sensitivity of 267 mAμM^{-1}cm^{-2}, with a linear range between 20 μM and 1.79 mM, a limit of detection of 11 μM, excellent reproducibility, and good selectivity towards common sweat interferents.

Finally, a prototype of a wearable and non-invasive glucose sensor was shown, which included a two-electrode system for the sweat generation via iontophoresis, made of LIG, and the proposed CuNPs-LIG sensor for the glucose detection. This pattern was first engraved in a paper substrate and consequently transferred to a polyurethane tape, with adhesive and flexible properties.

This thesis stands as a solid foundation and starting point for the development of a sensor applicable for sensing glucose in human sweat. However, additional tests and optimizations must be performed on the sensor to refine the presented glucose sensor before including it in glucose monitoring system in sweat. To achieve this goal, a list of points that must be taken into consideration when planning the future work is presented:

- Copper precursor optimization - Although a study of this kind was carried out during this work, there is still the need for a more detailed copper sulfate optimization

by testing the sensor current response with smaller variations of the drop-casted precursor concentration. Moreover, sensors fabricated with other copper precursors could be tested.

- Control of copper precursor deposition - By controlling the ambient conditions of the precursor drying environment, such as temperature and humidity, greater sensor uniformity and a diminished variability in the current response will be ensured.
- Copper precursor excess removal - Cleaning processes with deionized water and other cleaning solutions could be studied to remove any residual copper precursor that was not converted into CuNPs with the laser scan.
- Sensor Miniaturization - This would lead to an improvement in the sensor electrochemical response, by diminishing the effect of ohmic drop as demonstrated in Section 5.1.4.1, paired with a decrease in sensor production costs. Furthermore, the sensor size reduction will favor its application in glucose detection context based on sweat, since it will require the collection of lower sweat volumes.
- Since the selectivity tests were performed with only common interferents present in sweat samples, validation tests with real human sweat must be performed to assure the sensor viability in integrating a continuous system for glucose monitoring. All sensing protocols established for this thesis must be repeated with physiological samples.

Moreover, as future perspectives, follows some aspects that must be taken into consideration when projecting this sensor to the point of being included in a real-world context of glucose sensing in sweat:

- Sensor Optimization in Polyurethane tape - All tests and calibration curves would ave to be repeated for the sensor in this new substrate to assure that LIG and CuNPs nanostructures do not lose their functional properties and ability to oxidize glucose while the transfer process. This optimization will combine additional tests with increased repetitions and will use sweat as the target matrix, to settle this detection mechanism as a stable and reliable method for glucose sensing.
- Sweat Stimulation Optimization - The amount of generated sweat will be controlled through the manipulation of several factors such as the geometry of the iontophoresis electrodes, the sweat-inducing agent concentration, and the applied potential. An assessment of the need for the implementation of microfluidic elements such as channels and wells for the sweat collection will be required.
- Adaption for real-time glucose measurement - A flexible wireless circuit board will be projected and programmed to perform sequential operations of potential application between the iontophoretic electrodes for sweat generation and amperometric

measurement of the current response, allowing for an effective glucose monitoring system. Since the nonenzymatic sensing principle of glucose depends on an alkaline medium for glucose oxidation, the inclusion of a NaOH solution in this device will be studied.

As a general note to the presented work, it can be said that the simultaneously synthesis of CuNPs and LIG provides is a simple and rapid fabrication method, suitable to be scaled-up. These findings have great potential and application value for the depelopment of flexible electronics in an economical and sustainable way. Ultimately, by pointing out the potential of this new approach to synthesize LIG and CuNPs on paper for the nonenzymatic detection of glucose, this work brings up new possibilities for the biosensing field in future medicine.

Bibliography

[1] J. Heikenfeld et al. "Wearable sensors: Modalities, challenges, and prospects". In: *Lab on a Chip* 18.2 (2018), pp. 217–248. ISSN: 14730189. DOI: 10.1039/c7lc00914c.

[2] World Health Organization. *Diabetes*. URL: https://www.who.int/health-topics/diabetes#tab=tab_1 (visited on 02/08/2021).

[3] B. Salim. *Diabetes mellitus and its treatment | International Journal of Diabetes and Metabolism. 2005; 13 (3): 111-134 | IMEMR*. URL: https://pesquisa.bvsalud.org/portal/resource/pt/emr-171007?lang=en (visited on 08/13/2021).

[4] E. W. Nery et al. "Electrochemical glucose sensing: Is there still room for improvement?" In: *Analytical Chemistry* 88.23 (2016), pp. 11271–11282. ISSN: 15206882. DOI: 10.1021/acs.analchem.6b03151.

[5] Grand View Research. *Glucose Biosensor Market Size Share, 2022 | Industry Growth Report*. URL: https://www.millioninsights.com/industry-reports/glucose-biosensor-market (visited on 02/08/2021).

[6] H. C. Wang and A. R. Lee. "Recent developments in blood glucose sensors". In: *Journal of Food and Drug Analysis* 23.2 (2015), pp. 191–200. ISSN: 10219498. DOI: 10.1016/j.jfda.2014.12.001.

[7] S. M. Khan, J. M. Nassar, and M. M. Hussain. "Paper as a Substrate and an Active Material in Paper Electronics". In: *ACS Applied Electronic Materials* 3.1 (2021), pp. 30–52. ISSN: 26376113. DOI: 10.1021/acsaelm.0c00484.

[8] N. Kurra and G. U. Kulkarni. "Pencil-on-paper: Electronic devices". In: *Lab on a Chip* 13.15 (2013), pp. 2866–2873. ISSN: 14730189. DOI: 10.1039/c3lc50406a.

[9] S. A. and N. M. "A review of types 1 and 2 diabetes mellitus and their treatment with insulin". In: *American Journal of Therapeutics* 13.4 (2006), pp. 349–361. ISSN: 1075-2765.

[10] Z. Chen et al. "A low-cost paper glucose sensor with molecularly imprinted polyaniline electrode". In: *Sensors (Switzerland)* 20.4 (2020), pp. 1–11. ISSN: 14248220. DOI: 10.3390/s20041098.

[11] P. Saeedi et al. "Global and regional diabetes prevalence estimates for 2019 and projections for 2030 and 2045: Results from the International Diabetes Federation Diabetes Atlas, 9th edition". In: *Diabetes Research and Clinical Practice* 157 (2019), p. 107843. ISSN: 18728227. DOI: 10.1016/j.diabres.2019.107843.

[12] International Diabetes Federation. *Worldwide toll of diabetes*. URL: https://www.diabetesatlas.org/en/sections/worldwide-toll-of-diabetes.html (visited on 10/31/2021).

[13] Mayo Clinic. *Hypoglycemia - Symptoms and causes - Mayo Clinic*. URL: https://www.mayoclinic.org/diseases-conditions/hypoglycemia/symptoms-causes/syc-20373685 (visited on 02/08/2021).

[14] American Diabetes Association. *Hypoglycemia (Low Blood Glucose) | ADA*. URL: https://www.diabetes.org/healthy-living/medication-treatments/blood-glucose-testing-and-control/hypoglycemia (visited on 08/17/2021).

[15] Mayo Clinic. *Hyperglycemia in diabetes - Symptoms and causes - Mayo Clinic*. URL: https://www.mayoclinic.org/diseases-conditions/hyperglycemia/symptoms-causes/syc-20373631 (visited on 02/08/2021).

[16] A. Haleem et al. "Biosensors applications in medical field: A brief review". In: *Sensors International* 2.May (2021), p. 100100. ISSN: 26663511. DOI: 10.1016/j.sintl.2021.100100.

[17] B. Van Dorst et al. "Recent advances in recognition elements of food and environmental biosensors: A review". In: *Biosensors and Bioelectronics* 26.4 (2010), pp. 1178–1194. ISSN: 09565663. DOI: 10.1016/j.bios.2010.07.033.

[18] T. V. Duncan. "Applications of nanotechnology in food packaging and food safety: Barrier materials, antimicrobials and sensors". In: *Journal of Colloid and Interface Science* 363.1 (2011), pp. 1–24. ISSN: 00219797. DOI: 10.1016/j.jcis.2011.07.017.

[19] E. d. S. Gil and G. R. de Melo. "Electrochemical biosensors in pharmaceutical analysis". In: *Brazilian Journal of Pharmaceutical Sciences* 46.3 (2010), pp. 375–391. ISSN: 21759790. DOI: 10.1590/S1984-82502010000300002.

[20] Sullivan and Frost. *Emerging Trends and Applications of Biosensors*. 2018. URL: https://aabme.asme.org/posts/emerging-trends-and-applications-of-biosensors (visited on 08/04/2021).

[21] A. Kawamura and T. Miyata. "Biosensors". In: *Biomaterials Nanoarchitectonics* (2016), pp. 157–176. DOI: 10.1016/B978-0-323-37127-8.00010-8.

[22] Ganesh. *Biosensors Market Size, Global Trends, Demands and Industry Analysis 2021 to 2027 – The Manomet Current*. URL: https://manometcurrent.com/biosensors-market-size-global-trends-demands-and-industry-analysis-2021-to-2027/ (visited on 10/31/2021).

[23] N. Bhalla et al. "Introduction to biosensors". In: *Essays in Biochemistry* 60.1 (June 2016). Ed. by P. Estrela, pp. 1–8. ISSN: 0071-1365. DOI: 10.1042/EBC20150001.

[24] C. Karunakaran, K. Bhargava, and R. Benjamin. *Biosensors and Bioelectronics*. Elsevier, 2015. ISBN: 9780128031001. DOI: 10.1016/C2014-0-03790-2.

[25] Y. Yang and W. Gao. "Wearable and flexible electronics for continuous molecular monitoring". In: *Chemical Society Reviews* 48.6 (2019), pp. 1465–1491. ISSN: 0306-0012. DOI: 10.1039/C7CS00730B.

[26] S. Roy et al. "Modernization of biosensing strategies for the development of lab-on-chip integrated systems". In: *Bioelectrochemical Interface Engineering* (2019), pp. 325–342. DOI: 10.1002/9781119611103.ch17.

[27] H. Teymourian, A. Barfidokht, and J. Wang. "Electrochemical glucose sensors in diabetes management: An updated review (2010-2020)". In: *Chemical Society Reviews* 49.21 (2020), pp. 7671–7709. ISSN: 14604744. DOI: 10.1039/d0cs00304b.

[28] P. Zuman. *Electrochemical Reactions and Mechanisms in Organic Chemistry*. Vol. 73. 3. Elsevier, Dec. 2000, pp. 367–368. ISBN: 9780444720078. DOI: 10.1016/B978-0-444-72007-8.X5000-9.

[29] J. A. Rogers et al. "Optical Generation and Characterization of Acoustic Waves in Thin Films: Fundamentals and Applications". In: *Annual Review of Materials Science* 30.1 (Aug. 2000), pp. 117–157. ISSN: 0084-6600. DOI: 10.1146/annurev.matsci.30.1.117.

[30] K. Honeychurch. "Printed thick-film biosensors". In: *Printed Films*. Elsevier, 2012, pp. 366–409. DOI: 10.1533/9780857096210.2.366.

[31] A. C. Marques et al. *Non-enzymatic lab-on-paper devices for biosensing applications*. 1st ed. Vol. 89. Elsevier B.V., 2020, pp. 189–237. DOI: 10.1016/bs.coac.2020.05.001.

[32] N. Shah, M. B. Arain, and M. Soylak. "Historical background: milestones in the field of development of analytical instrumentation". In: *New Generation Green Solvents for Separation and Preconcentration of Organic and Inorganic Species* (Jan. 2020), pp. 45–73. DOI: 10.1016/B978-0-12-818569-8.00002-4.

[33] D. Harvey. *Analytical Chemistry 2.1*. 2016, p. 729.

[34] G. A. Mabbott. "An introduction to cyclic voltammetry". In: *Journal of Chemical Education* 60.9 (1983), pp. 697–702. ISSN: 00219584. DOI: 10.1021/ed060p697.

[35] P. T. Kissinger and W. R. Heineman. "Cyclic voltammetry". In: *Journal of Chemical Education* 60.9 (1983), pp. 702–706. ISSN: 00219584. DOI: 10.1021/ed060p702.

[36] N. Elgrishi et al. "A Practical Beginner's Guide to Cyclic Voltammetry". In: *Journal of Chemical Education* 95.2 (2018), pp. 197–206. ISSN: 19381328. DOI: 10.1021/acs.jchemed.7b00361.

[37] A. Prabhakaran and P. Nayak. "Surface Engineering of Laser-Scribed Graphene Sensor Enables Non-Enzymatic Glucose Detection in Human Body Fluids". In: *ACS Applied Nano Materials* 3.1 (2020), pp. 391–398. ISSN: 25740970. DOI: 10.1021/acsanm.9b02025.

[38] T. Pinheiro et al. "Laser-Induced Graphene on Paper toward Efficient Fabrication of Flexible , Planar Electrodes for Electrochemical Sensing". In: 2101502 (2021), pp. 1–12. DOI: 10.1002/admi.202101502.

[39] I. Lavagnini, R. Antiochia, and F. Magno. "An extended method for the practical evaluation of the standard rate constant from cyclic voltammetric data". In: *Electroanalysis* 16.6 (2004), pp. 505–506. ISSN: 10400397. DOI: 10.1002/elan.200302851.

[40] PalmSens. *Ohmic drop - PalmSens*. URL: www.palmsens.com/knowledgebase-topic/ohmic-drop/ (visited on 01/06/2022).

[41] M. Autolab. "Application Area : Fundamental Ohmic Drop Part 1 – Basic Principles". In: (), pp. 2–4.

[42] T. A. Saleh. "Nanomaterials: Classification, properties, and environmental toxicities". In: *Environmental Technology and Innovation* 20 (2020), p. 101067. ISSN: 23521864. DOI: 10.1016/j.eti.2020.101067.

[43] D. Tonelli, E. Scavetta, and I. Gualandi. "Electrochemical deposition of nanomaterials for electrochemical sensing". In: *Sensors (Switzerland)* 19.5 (2019). ISSN: 14248220. DOI: 10.3390/s19051186.

[44] X. Zhang, Q. Guo, and D. Cui. "Recent advances in nanotechnology applied to biosensors". In: *Sensors* 9.2 (2009), pp. 1033–1053. ISSN: 14248220. DOI: 10.3390/s90201033.

[45] K. Rajavel et al. "Recent Progress on the Synthesis and Applications of Carbon Based Nanostructures". In: *Recent Patents on Nanotechnology* 6.2 (2012), pp. 99–104. ISSN: 18722105. DOI: 10.2174/187221012800270199.

[46] Y. Zhai, Z. Zhu, and S. Dong. "ChemInform Abstract: Carbon-Based Nanostructures for Advanced Catalysis". In: *ChemInform* 46.44 (2015), no–no. DOI: 10.1002/chin.201544277.

[47] T. H. E. Royal, S. Academy, and O. F. Sciences. "compiled by the Class for Physics of the Royal Swedish Academy of Sciences Graphene". In: *The Royal Swedish Academy of Sciences* 50005.October (2010), pp. 0–10. ISSN: 1476-4687. arXiv: 1011.4680.

[48] The University of Manchester. *Emerging Trends and Applications of Biosensors*. URL: https://aabme.asme.org/posts/emerging-trends-and-applications-of-biosensors (visited on 11/02/2021).

[49] X. J. Lee et al. "Review on graphene and its derivatives: Synthesis methods and potential industrial implementation". In: *Journal of the Taiwan Institute of Chemical Engineers* 98.xxxx (2019), pp. 163–180. ISSN: 18761070. DOI: 10.1016/j.jtice.2018.10.028.

[50] S. Chaitoglou, E. Bertran, and J. L. Andujar. "Growth Study and Characterization of Single-Layer Graphene Structures Deposited on Copper Substrate by Chemical Vapour Deposition". In: *Graphene Materials - Structure, Properties and Modifications* November (2017). DOI: 10.5772/67439.

[51] N. Kumar et al. "Top-down synthesis of graphene: A comprehensive review". In: *FlatChem* 27.February (2021), p. 100224. ISSN: 24522627. DOI: 10.1016/j.flatc.2021.100224.

[52] P. He et al. "Screen-Printing of a Highly Conductive Graphene Ink for Flexible Printed Electronics". In: *ACS Applied Materials and Interfaces* 11.35 (2019), pp. 32225–32234. ISSN: 19448252. DOI: 10.1021/acsami.9b04589.

[53] E. B. Secor et al. "Inkjet printing of high conductivity, flexible graphene patterns". In: *Journal of Physical Chemistry Letters* 4.8 (2013), pp. 1347–1351. ISSN: 19487185. DOI: 10.1021/jz400644c.

[54] R. Ye, D. K. James, and J. M. Tour. "Laser-Induced Graphene: From Discovery to Translation". In: *Advanced Materials* 31.1 (2019), pp. 1–15. ISSN: 15214095. DOI: 10.1002/adma.201803621.

[55] A. Kaidarova et al. "Wearable multifunctional printed graphene sensors". In: *npj Flexible Electronics* 3.1 (2019), pp. 1–10. ISSN: 23974621. DOI: 10.1038/s41528-019-0061-5.

[56] M. G. Stanford et al. "Laser-Induced Graphene for Flexible and Embeddable Gas Sensors". In: *ACS Nano* 13.3 (2019), pp. 3474–3482. ISSN: 1936086X. DOI: 10.1021/acsnano.8b09622.

[57] Y. Zhu et al. "Highly sensitive and skin-like pressure sensor based on asymmetric double-layered structures of reduced graphite oxide". In: *Sensors and Actuators, B: Chemical* 255 (2018), pp. 1262–1267. ISSN: 09254005. DOI: 10.1016/j.snb.2017.08.116.

[58] H. Yoon et al. "A chemically modified laser-induced porous graphene based flexible and ultrasensitive electrochemical biosensor for sweat glucose detection". In: *Sensors and Actuators, B: Chemical* 311 (2020), p. 127866. ISSN: 09254005. DOI: 10.1016/j.snb.2020.127866.

[59] Y. Zhang et al. "A flexible non-enzymatic glucose sensor based on copper nanoparticles anchored on laser-induced graphene". In: *Carbon* 156 (2020), pp. 506–513. ISSN: 00086223. DOI: 10.1016/j.carbon.2019.10.006.

[60] A. Selimis, V. Mironov, and M. Farsari. "Direct laser writing: Principles and materials for scaffold 3D printing". In: *Microelectronic Engineering* 132.October (2015), pp. 83–89. ISSN: 01679317. DOI: 10.1016/j.mee.2014.10.001.

[61] J. Lin et al. "Laser-induced porous graphene films from commercial polymers". In: *Nature Communications* 5 (2014), pp. 1–8. ISSN: 20411723. DOI: 10.1038/ncomms6714.

[62] Y. Chyan et al. "Laser-Induced Graphene by Multiple Lasing: Toward Electronics on Cloth, Paper, and Food". In: *ACS Nano* 12.3 (2018), pp. 2176–2183. ISSN: 1936086X. DOI: 10.1021/acsnano.7b08539.

[63] B. Zhu et al. "Disposable and portable gold nanoparticles modified - laser-scribed graphene sensing strips for electrochemical, non-enzymatic detection of glucose". In: 378 (2021). ISSN: 00134686. DOI: 10.1016/j.electacta.2021.138132.

[64] E. Aparicio-Martínez et al. "Flexible electrochemical sensor based on laser scribed Graphene/Ag nanoparticles for non-enzymatic hydrogen peroxide detection". In: *Sensors and Actuators, B: Chemical* 301.September (2019), p. 127101. ISSN: 09254005. DOI: 10.1016/j.snb.2019.127101.

[65] H. L. Zhang et al. "An amperometric hydrogen peroxide biosensor based on immobilization of horseradish peroxidase on an electrode modified with magnetic dextran microspheres". In: *Analytical and Bioanalytical Chemistry* 390.3 (2008), pp. 971–977. ISSN: 16182642. DOI: 10.1007/s00216-007-1748-3.

[66] Y. Zhu et al. "A non-enzymatic amperometric glucose sensor based on the use of graphene frameworks-promoted ultrafine platinum nanoparticles". In: *Microchimica Acta* 186.8 (2019). ISSN: 14365073. DOI: 10.1007/s00604-019-3653-9.

[67] Y. Liu et al. "Nonenzymatic glucose sensor based on renewable electrospun Ni nanoparticle-loaded carbon nanofiber paste electrode". In: *Biosensors and Bioelectronics* 24.11 (2009), pp. 3329–3334. ISSN: 09565663. DOI: 10.1016/j.bios.2009.04.032.

[68] M. M. Jolaei et al. "Usage of alkaline glucose for Synthesis Copper Nano particle on Polyester Fabric". In: *Ciência e Natura* 37 (2015), p. 63. ISSN: 0100-8307. DOI: 10.5902/2179460x20831.

[69] G. A. Naikoo et al. "Fourth-generation glucose sensors composed of copper nanostructures for diabetes management: A critical review". In: *Bioengineering and Translational Medicine* 7.1 (2022), pp. 1–17. ISSN: 23806761. DOI: 10.1002/btm2.10248.

[70] V. B. Juska and G. Juska. "Copper-nanostructure-modified laser-scribed electrodes based on graphitic carbon for electrochemical detection of dopamine and glucose". In: *Journal of Chemical Technology and Biotechnology* 96.4 (2021), pp. 1086–1095. ISSN: 10974660. DOI: 10.1002/jctb.6620.

[71] W. Zheng et al. "CuII-Mediated Ultra-efficient Electrooxidation of Glucose". In: *ChemElectroChem* 4.11 (2017), pp. 2788–2792. ISSN: 21960216. DOI: 10.1002/celc.201700712.

[72] Y. Xu et al. "Lab-on-paper micro- and nano-analytical devices: Fabrication, modification, detection and emerging applications". In: *Microchimica Acta* 183.5 (2016), pp. 1521–1542. ISSN: 14365073. DOI: 10.1007/s00604-016-1841-4.

[73] H. Su et al. "Waste to wealth: A sustainable and flexible supercapacitor based on office waste paper electrodes". In: *Journal of Electroanalytical Chemistry* 786 (2017), pp. 28–34. ISSN: 15726657. DOI: 10.1016/j.jelechem.2017.01.002.

[74] A. Gumrah Dumanli. "Nanocellulose and its Composites for Biomedical Applications". In: *Current Medicinal Chemistry* 24.5 (2016), pp. 512–528. ISSN: 09298673. DOI: 10.2174/0929867323666161014124008.

[75] A. K. Yetisen, M. S. Akram, and C. R. Lowe. "Paper-based microfluidic point-of-care diagnostic devices". In: *Lab on a Chip* 13.12 (2013), pp. 2210–2251. ISSN: 14730189. DOI: 10.1039/c3lc50169h.

[76] J. H. Lee, ed. *Paper-Based Medical Diagnostic Devices*. Vol. 10. Bioanalysis. Singapore: Springer Singapore, 2021, pp. 7–40. ISBN: 978-981-15-8722-1. DOI: 10.1007/978-981-15-8723-8.

[77] M. Bariya, H. Y. Y. Nyein, and A. Javey. "Wearable sweat sensors". In: *Nature Electronics* 1.3 (2018), pp. 160–171. ISSN: 25201131. DOI: 10.1038/s41928-018-0043-y.

[78] H. Lee et al. "Enzyme-Based Glucose Sensor: From Invasive to Wearable Device". In: *Advanced Healthcare Materials* 7.8 (2018), pp. 1–14. ISSN: 21922659. DOI: 10.1002/adhm.201701150.

[79] C. Y. Cui and D. Schlessinger. "Eccrine sweat gland development and sweat secretion". In: *Experimental Dermatology* 24.9 (2015), pp. 644–650. ISSN: 16000625. DOI: 10.1111/exd.12773.

[80] S. Emaminejad et al. "Autonomous sweat extraction and analysis applied to cystic fibrosis and glucose monitoring using a fully integrated wearable platform". In: *Proceedings of the National Academy of Sciences of the United States of America* 114.18 (2017), pp. 4625–4630. ISSN: 10916490. DOI: 10.1073/pnas.1701740114.

[81] J. N. Hussain, N. Mantri, and M. M. Cohen. "Working up a good sweat - The challenges of standardising sweat collection for metabolomics analysis". In: *Clinical Biochemist Reviews* 38.1 (2017), pp. 13–34. ISSN: 18380212.

[82] E. V. Karpova, E. E. Karyakina, and A. A. Karyakin. "Wearable non-invasive monitors of diabetes and hypoxia through continuous analysis of sweat". In: *Talanta* 215.February (2020), p. 120922. ISSN: 00399140. DOI: 10.1016/j.talanta.2020.120922.

[83] L. B. Baker. "Physiology of sweat gland function: The roles of sweating and sweat composition in human health". In: *Temperature* 6.3 (2019), pp. 211–259. ISSN: 23328959. DOI: 10.1080/23328940.2019.1632145.

[84] J. Heikenfeld. "Bioanalytical devices: Technological leap for sweat sensing". In: *Nature* 529.7587 (2016), pp. 475–476. ISSN: 14764687. DOI: 10.1038/529475a.

[85] R. Granstein and T. Luger. *Neuroimmunology of the Skin*. 2009. ISBN: 9783540359869. DOI: 10.1007/978-3-540-35989-0.

[86] W. Gao et al. "Fully integrated wearable sensor arrays for multiplexed in situ perspiration analysis". In: *Nature* 529.7587 (2016), pp. 509–514. ISSN: 14764687. DOI: 10.1038/nature16521.

[87] D. R. Whiting et al. "IDF Diabetes Atlas: Global estimates of the prevalence of diabetes for 2011 and 2030". In: *Diabetes Research and Clinical Practice* 94.3 (2011), pp. 311–321. ISSN: 01688227. DOI: 10.1016/j.diabres.2011.10.029.

[88] H. Kudo et al. "A flexible and wearable glucose sensor based on functional polymers with Soft-MEMS techniques". In: *Biosensors and Bioelectronics* 22.4 SPEC. ISS. (2006), pp. 558–562. ISSN: 09565663. DOI: 10.1016/j.bios.2006.05.006.

[89] J. Kim et al. "Wearable smart sensor systems integrated on soft contact lenses for wireless ocular diagnostics". In: *Nature Communications* 8 (2017). ISSN: 20411723. DOI: 10.1038/ncomms14997.

[90] J. Chen et al. "Electrocatalytic oxidation of glucose on bronze for monitoring of saliva glucose using a smart toothbrush". In: *Sensors and Actuators, B: Chemical* 285.December 2018 (2019), pp. 56–61. ISSN: 09254005. DOI: 10.1016/j.snb.2019.01.017.

[91] T. Arakawa et al. "Mouthguard biosensor with telemetry system for monitoring of saliva glucose: A novel cavitas sensor". In: *Biosensors and Bioelectronics* 84 (2016), pp. 106–111. ISSN: 18734235. DOI: 10.1016/j.bios.2015.12.014.

[92] J. Kim et al. "Simultaneous Monitoring of Sweat and Interstitial Fluid Using a Single Wearable Biosensor Platform". In: *Advanced Science* 5.10 (2018). ISSN: 21983844. DOI: 10.1002/advs.201800880.

[93] F. Schedin et al. "Detection of individual gas molecules adsorbed on graphene". In: *Nature Materials* 6.9 (2007), pp. 652–655. ISSN: 14761122. DOI: 10.1038/nmat1967.

[94] C. Shan et al. "Direct electrochemistry of glucose oxidase and biosensing for glucose based on graphene". In: *Analytical Chemistry* 81.6 (2009), pp. 2378–2382. ISSN: 00032700. DOI: 10.1021/ac802193c.

[95] L. C. Clark and C. Lyons. "ELECTRODE SYSTEMS FOR CONTINUOUS MONITORING IN CARDIOVASCULAR SURGERY". In: *Annals of the New York Academy of Sciences* 102.1 (Dec. 2006), pp. 29–45. ISSN: 00778923. DOI: 10.1111/j.1749-6632.1962.tb13623.x.

[96] D. W. Hwang et al. "Recent advances in electrochemical non-enzymatic glucose sensors – A review". In: *Analytica Chimica Acta* 1033 (2018), pp. 1–34. ISSN: 18734324. DOI: 10.1016/j.aca.2018.05.051.

[97] S. Ferri, K. Kojima, and K. Sode. "Review of glucose oxidases and glucose dehydrogenases: A bird's eye view of glucose sensing enzymes". In: *Journal of Diabetes Science and Technology* 5.5 (2011), pp. 1068–1076. ISSN: 19322968. DOI: 10.1177/193229681100500507.

[98] X. Zhu et al. "Nonenzymatic wearable sensor for electrochemical analysis of perspiration glucose". In: *ACS Sensors* 3.6 (2018), pp. 1135–1141. ISSN: 23793694. DOI: 10.1021/acssensors.8b00168.

[99] L. T. Hoa, K. G. Sun, and S. H. Hur. "Highly sensitive non-enzymatic glucose sensor based on Pt nanoparticle decorated graphene oxide hydrogel". In: *Sensors and Actuators, B: Chemical* 210 (Apr. 2015), pp. 618–623. ISSN: 09254005. DOI: 10.1016/j.snb.2015.01.020.

[100] J. Luo et al. "A novel non-enzymatic glucose sensor based on Cu nanoparticle modified graphene sheets electrode". In: *Analytica Chimica Acta* 709 (2012), pp. 47–53. ISSN: 00032670. DOI: 10.1016/j.aca.2011.10.025.

[101] H. Wei and E. Wang. "Nanomaterials with enzyme-like characteristics (nanozymes): Next-generation artificial enzymes". In: *Chemical Society Reviews* 42.14 (2013), pp. 6060–6093. ISSN: 14604744. DOI: 10.1039/c3cs35486e.

[102] Q. Zhang et al. "Self-Assembly of Graphene-Encapsulated Cu Composites for Nonenzymatic Glucose Sensing". In: *ACS Omega* 3.3 (2018), pp. 3420–3428. ISSN: 24701343. DOI: 10.1021/acsomega.7b01197.

[103] J. Zhao et al. "A non-enzymatic glucose sensor based on the composite of cubic Cu nanoparticles and arc-synthesized multi-walled carbon nanotubes". In: *Biosensors and Bioelectronics* 47 (2013), pp. 86–91. ISSN: 09565663. DOI: 10.1016/j.bios.2013.02.032.

[104] D. Jiang et al. "Enhanced non-enzymatic glucose sensing based on copper nanoparticles decorated nitrogen-doped graphene". In: *Biosensors and Bioelectronics* 54 (2014), pp. 273–278. ISSN: 18734235. DOI: 10.1016/j.bios.2013.11.005.

[105] J. Luo et al. "A novel non-enzymatic glucose sensor based on Cu nanoparticle modified graphene sheets electrode". In: *Analytica Chimica Acta* 709 (2012), pp. 47–53. ISSN: 00032670. DOI: 10.1016/j.aca.2011.10.025.

[106] F. Tehrani, L. Reiner, and B. Bavarian. "Rapid prototyping of a high sensitivity graphene based glucose sensor strip". In: *PLoS ONE* 10.12 (2015), pp. 1–11. ISSN: 19326203. DOI: 10.1371/journal.pone.0145036.

[107] F. Tehrani and B. Bavarian. "Facile and scalable disposable sensor based on laser engraved graphene for electrochemical detection of glucose". In: *Scientific Reports* 6.January (2016), pp. 1–10. ISSN: 20452322. DOI: 10.1038/srep27975.

[108] S. Wang et al. "Facile fabrication of biosensors based on Cu nanoparticles modified as-grown CVD graphene for non-enzymatic glucose sensing". In: *Journal of Electroanalytical Chemistry* 853.July (2019), p. 113527. ISSN: 15726657. DOI: 10.1016/j.jelechem.2019.113527.

[109] V. B. Juska, A. Walcarius, and M. E. Pemble. "Cu Nanodendrite Foams on Integrated Band Array Electrodes for the Nonenzymatic Detection of Glucose". In: *ACS Applied Nano Materials* 2.9 (2019), pp. 5878–5889. ISSN: 25740970. DOI: 10.1021/acsanm.9b01325.

[110] B. Wang et al. "Flexible paper sensor fabricated via in situ growth of Cu nanoflower on RGO sheets towards amperometrically non-enzymatic detection of glucose". In: *Sensors and Actuators, B: Chemical* 238 (2017), pp. 802–808. ISSN: 09254005. DOI: 10.1016/j.snb.2016.07.137.

[111] R. Xu et al. "Effective design of MnO2 nanoparticles embedded in laser-induced graphene as shape-controllable electrodes for flexible planar microsupercapacitors". In: 571 (2022), p. 151385. ISSN: 01694332. DOI: 10.1016/j.apsusc.2021.151385.

[112] J. Zhao et al. "Boosting the performance of flexible in-plane micro-supercapacitors by engineering MoS2 nanoparticles embedded in laser-induced graphene". In: *Journal of Alloys and Compounds* 887 (2021), p. 161514. ISSN: 09258388. DOI: 10.1016/j.jallcom.2021.161514.

[113] J. Zhao et al. "Co3O4 nanoparticles embedded in laser-induced graphene for a flexible and highly sensitive enzyme-free glucose biosensor". In: *Sensors and Actuators B: Chemical* 347.June (2021), p. 130653. ISSN: 09254005. DOI: 10.1016/j.snb.2021.130653.

[114] Z. You et al. "Laser-induced noble metal nanoparticle-graphene composites enabled flexible biosensor for pathogen detection". In: *Biosensors and Bioelectronics* 150.October (2020), p. 111896. ISSN: 18734235. DOI: 10.1016/j.bios.2019.111896.

[115] P. Peng et al. "One-step selective laser patterning of copper/graphene flexible electrodes". In: *Nanotechnology* 30.18 (2019). ISSN: 13616528. DOI: 10.1088/1361-6528/aafe4c.

[116] J. Liao, W. Guo, and P. Peng. "Direct laser writing of copper-graphene composites for flexible electronics". In: *Optics and Lasers in Engineering* 142 (July 2021). ISSN: 01438166. DOI: 10.1016/j.optlaseng.2021.106605.

[117] D. Xu et al. "One-step fabrication of a laser-induced forward transfer graphene/Cu:XO nanocomposite-based electrocatalyst to promote hydrogen evolution reaction". In: *Journal of Materials Chemistry A* 9.30 (Aug. 2021), pp. 16470–16478. ISSN: 20507496. DOI: 10.1039/d1ta01267c.

[118] D. Thirumalai et al. "In situsynthesis of copper-ruthenium bimetallic nanoparticles on laser-induced graphene as a peroxidase mimic". In: *Chemical Communications* 57.15 (Feb. 2021), pp. 1947–1950. ISSN: 1364548X. DOI: 10.1039/d0cc07518c.

[119] H. Liu et al. "Laser-oxidized Fe3O4 nanoparticles anchored on 3D macroporous graphene flexible electrodes for ultrahigh-energy in-plane hybrid micro supercapacitors". In: *Nano Energy* 77.February (2020), p. 105058. ISSN: 22112855. DOI: 10.1016/j.nanoen.2020.105058.

[120] Y. Chyan et al. "Graphene Art". In: *ACS Applied Nano Materials* 2.5 (2019), pp. 3007–3011. ISSN: 25740970. DOI: 10.1021/acsanm.9b00391.

[121] S. Lee and S. Jeon. "Laser-Induced Graphitization of Cellulose Nanofiber Substrates under Ambient Conditions". In: *ACS Sustainable Chemistry and Engineering* 7.2 (2019), pp. 2270–2275. ISSN: 21680485. DOI: 10.1021/acssuschemeng.8b04955.

[122] Y. Yao et al. "One-step process for direct laser writing carbonization of NH4H2PO4 treated cellulose paper and its use for facile fabrication of multifunctional force sensors with corrugated structures". In: *Cellulose* 26.12 (2019), pp. 7423–7435. ISSN: 1572882X. DOI: 10.1007/s10570-019-02617-4.

[123] B. Kulyk et al. "Laser-Induced Graphene from Paper for Mechanical Sensing". In: *ACS Applied Materials and Interfaces* 13.8 (2021), pp. 10210–10221. ISSN: 19448252. DOI: 10.1021/acsami.0c20270.

[124] A. D. M. Samouco. "Laser induced electrodes towards low cost flexible electronics and its applications in a UV sensor". In: (2017).

[125] E. Nagle. *Scanning electron microscopy*. 2019.

[126] P. J. Larkin. "IR and Raman Spectra–Structure Correlations". In: *Infrared and Raman Spectroscopy*. Elsevier, 2018, pp. 85–134. DOI: 10.1016/B978-0-12-804162-8.00006-9.

[127] Horiba. *What is Raman Spectroscopy? - HORIBA*. URL: https://www.horiba.com/fra/raman-imaging-and-spectroscopy/ (visited on 02/13/2022).

[128] T. Pinheiro. "Multiplex, Enzyme-free, Colorimetric Paper-based Device for the Measurement of Glucose, Uric Acid and Cholesterol". In: (2018), pp. 1–121.

[129] H. Park et al. "Electronic Functionality Encoded Laser-Induced Graphene for Paper Electronics". In: 3.7 (2020), pp. 6899–6904. ISSN: 25740970. DOI: 10.1021/acsanm.0c01255.

[130] S. Kumail Abbas and M. Sabieh Anwar. "Electrochemical Impedance Spectroscopy (EIS) Gamry Interface 1010E Potentiostat/Galvanostat/ZRA". In: ().

[131] H. Zhou et al. "Copper nanoparticles modified nitrogen doped reduced graphene oxide 3-D superstructure for simultaneous determination of dihydroxybenzene isomers". In: *Sensors and Actuators, B: Chemical* 249 (2017), pp. 405–413. ISSN: 09254005. DOI: 10.1016/j.snb.2017.04.132.

[132] C. M. Whelan et al. "Cu adsorption on carboxylic acid-terminated self-assembled monolayers: A high-resolution X-ray photoelectron spectroscopy study". In: *Thin Solid Films* 464-465 (2004), pp. 388–392. ISSN: 00406090. DOI: 10.1016/j.tsf.2004.06.041.

[133] Martin Köhne. *Can graphene compete with copper in electrical conductivity? | Bosch Global*. URL: https://www.bosch.com/stories/can-graphene-compete-with-copper-in-electrical-conductivity/ (visited on 01/12/2022).

[134] J. H. Li et al. "Preparation and performance of electrochemical glucose sensors based on copper nanoparticles loaded on flexible graphite sheet". In: *Xinxing Tan Cailiao/New Carbon Materials* 35.4 (2020), pp. 410–419. ISSN: 10078827. DOI: 10.1016/S1872-5805(20)60498-X.

[135] M. M. Alam and M. M. Howlader. "Nonenzymatic electrochemical sensors via Cu native oxides (CuNOx) for sweat glucose monitoring". In: *Sensing and Bio-Sensing Research* 34.April (2021), p. 100453. ISSN: 22141804. DOI: 10.1016/j.sbsr.2021.100453.

[136] Q. Gong et al. "Enhanced non-enzymatic glucose sensing of Cu–BTC-derived porous copper@carbon agglomerate". In: *Journal of Materials Science* 53.10 (May 2018), pp. 7305–7315. ISSN: 0022-2461. DOI: 10.1007/s10853-018-2078-x.

[137] M. Basina. *All About Diabetic Test Strips: Use, Accuracy, Cost*. URL: https://www.healthline.com/diabetesmine/glucose-test-strips-diabetes-uses-accuracy-costs (visited on 02/25/2022).

I

Sheet resistance measurements

Table I.1: Sheet resistance values obtained for LIG produced at different heights.

Height	z = -0.1”		z = -0.05”		z = 0”		z = +0.05”	
Parameters	Sheet Resistance	Standard Deviation	Sheet Resistance	Standard Deviation	Sheet Resistance	Standard Deviation	Sheet Resistance	Standard Deviation
P1S1	-	-	-	-	35766	5254	2515	768
P2S2	-	-	477	97.8	-	-	-	-
P3S3	121.6	37.3	425	65.3	-	-	-	-
P3S4	-	-	489.8	110	-	-	2044	263
P3S5	-	-	-	-	-	-	7894	5555
P4S3	23.4	1.6	-	-	-	-	-	-
P4S4	58	6.8	248	31.2	-	-	-	-
P4S5	159.3	31.9	419.5	16.3	-	-	-	-
P4S6	-	-	488	255.9	-	-	4742	1636
P4S7	-	-	411	42.6	-	-	2761	939
P4S8	-	-	-	-	-	-	1486	257
P5S4	23	0.8	-	-	-	-	-	-
P5S5	33.8	1.7	-	-	-	-	-	-
P5S6	52	4.2	611,25	303	-	-	-	-
P5S7	58.6	2.6	918	82.7	-	-	-	-
P5S8	92	4.5	535.5	119.1	-	-	-	-
P6S6	21.9	2.3	-	-	-	-	-	-
P6S7	27.6	0.8	-	-	-	-	-	-
P6S8	31.8	1.6	806.8	328.1	-	-	-	-
P7S8	21.9	2.5	-	-	-	-	-	-